High order material point method

July, 2016

R.P.W.M. Tielen

Technische Universiteit Delft

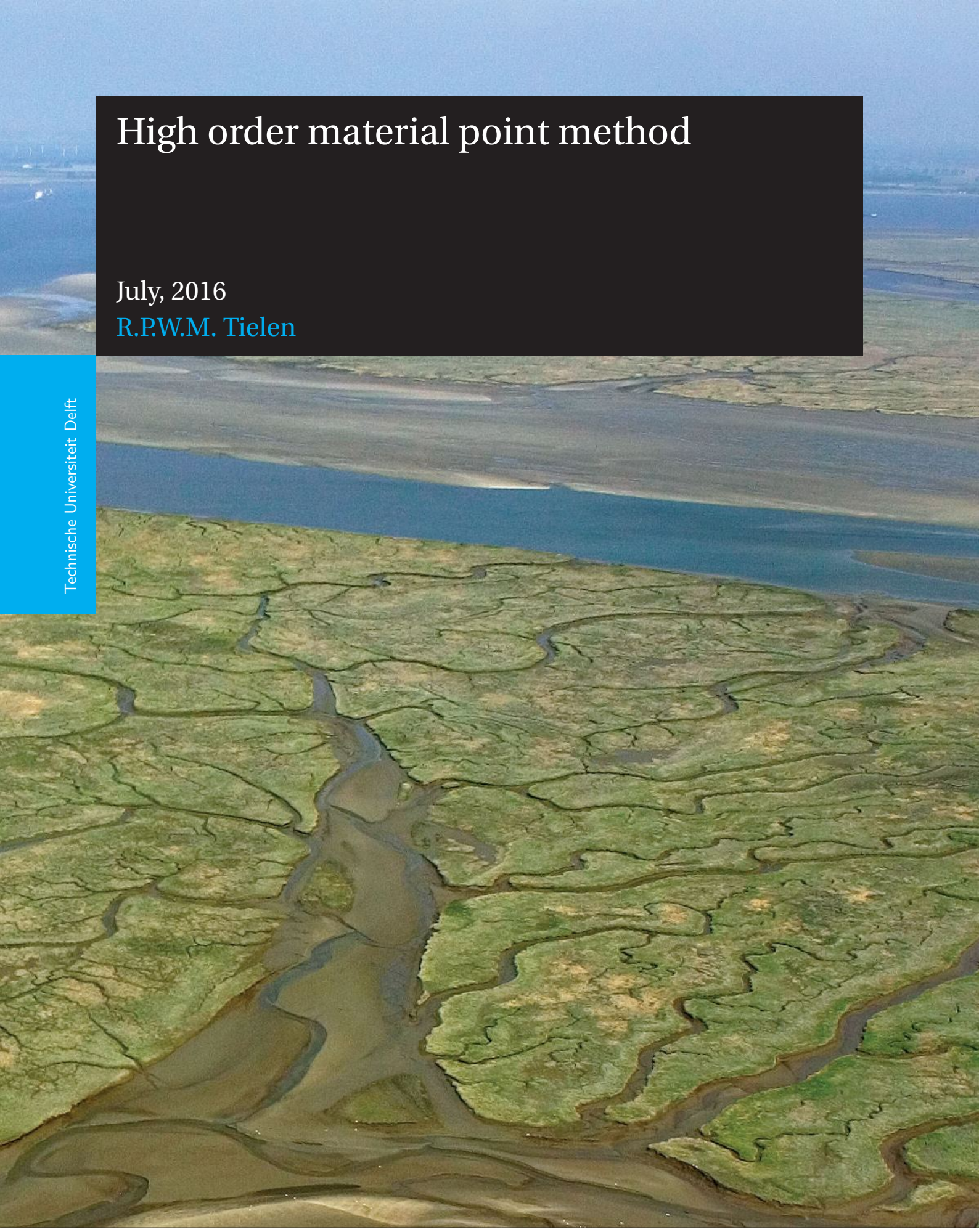

TU Delft Delft University of Technology

Deltares Enabling Delta Life

Challenge the future

HIGH ORDER MATERIAL POINT METHOD

JUNE 29, 2016

by

R.P.W.M. Tielen

in partial fulfillment of the requirements for the degree of

Master of Science
in Applied Mathematics

at the Delft University of Technology
to be defended publicly on Wednesday July 6, 2016 at 3:30 PM.

Project duration:	October 1, 2015 – July 6, 2016	
Supervisors:	Ir. E.D. Wobbes	TU Delft
	Dr.rer.nat. M. Möller	TU Delft
	Dr.-Ing. L.I. Beuth	Deltares

TU Delft Delft University of Technology

Deltares Enabling Delta Life

ABSTRACT

The material point method (MPM) is a meshfree mixed Lagrangian-Eulerian method which utilizes moving Lagrangian material points that store physical properties of a deforming continuum and a fixed Eulerian finite element mesh to solve the equations of motion for individual time steps. MPM proved to be successful in simulating mechanical problems which involve large deformations of history-dependent materials.

The solution on the background grid is found in MPM by a variational formulation. The integrals resulting from this formulation are numerically approximated by using the material points as integration points. However, the quality of this numerical quadrature rule decreases when the material points become unevenly distributed inside the mesh.

It is common practice in MPM to adopt piecewise linear basis functions for approximating the solution of the variational form. A problem arises from the discontinuity of the gradients of these basis functions at element boundaries leading to unphysical oscillations of computed stresses when material points cross element boundaries. Such grid crossing errors significantly affect the quality of the numerical solution and may lead to a lack of spatial convergence.

As a remedy to these problems, a version of the MPM making use of quadratic B-spline basis functions is presented. The C^0-continuity of their gradients eliminates grid crossing errors. Hence, a more accurate reproduction of physical quantities such as stresses and velocity is obtained. Using spline interpolation allows to more accurately approximate integrals, which enables the use of a coarser mesh. This in turn results in lower computational effort. To improve spatial convergence, the use of a consistent mass matrix instead of a lumped one commonly used with the MPM is suggested to project velocities from material points to the grid more accurately. Explicitly solving the linear system is avoided by using Richardson iteration. Improvements in terms of higher accuracy and rate of convergence are demonstrated for 1D benchmarks involving small and large deformations. In particular a vibrating bar and a column subjected to loading are considered.

This master project has been carried out in the period from October 2015 until July 2016 with support and in collaboration with Deltares, a Dutch research and consulting company that is developing MPM software to simulate geotechnical problems.

PREFACE

This thesis describes the results obtained during my master project, that I carried out in the period from October 2015 to July 2016 at the Numerical Analysis group of Professor Kees Vuik. I would like to thank him for giving me the opportunity to graduate at his chair and for introducing me to his colleague Matthias Möller who was just preparing a new master project on MPM at that time. This coincidence has led to a pleasant collaboration.

This master project is carried out together with Deltares. I would like to thank my colleagues of the unit GEO at Deltares, in particular Vahid Galavi and Miriam Mieremet for the great time during my internship. I enjoyed the lunch breaks, pub quizzes and other activities.

I want to express my gratitude to Matthias Möller and Lars Beuth for supervising me during this master project. Their ideas and feedback helped me to improve my knowledge and led to the numerical methods and results presented in this thesis. I would like to thank my daily supervisor Lisa Wobbes for her valuable feedback and giving me the opportunity to find my own path during this project.

Finally, I am very grateful to my parents, family and friends, for their continuous support during my entire study and helping me to keep things in perspective.

June 29, 2016
Roel Tielen

Contents

1

INTRODUCTION

In solid mechanics, problems are encountered which involve history-dependent material behaviour, large deformations and complex soil-structure interaction. The numerical simulation of these problems is challenging.

The numerical methods used in continuum mechanics make use of two classical descriptions of motion: the Lagrangian and Eulerian description [1]. In Eulerian methods such as Finite Differences Methods (FDM), the computational mesh is fixed and the continuum moves with respect to the grid. Although large deformation problems can be handled with these methods, the Eulerian formulation contains a nonlinear convective term, which makes it hard to deal with history-dependent materials [2]. Eulerian methods are generally used in fluid dynamics.

In Lagrangian methods such as the Updated Lagrange Finite Element Method (ULFEM) the mesh follows the material over time, making it easy to follow material free surface or multiple materials [3]. Furthermore, the consideration of history-dependent materials is easier in a Lagrangian frame. However, when large deformations are considered the mesh might get distorted.

The material point method (MPM) tries to combine the advantages of Lagrangian and Eulerian mehods. It proved to be successful in simulating problems which involve large deformations and history-dependent materials.

MPM uses a fixed background mesh and a set of material points moving through the mesh to model the deforming material. In every time step, the equations of motion are solved numerically on the background mesh to update particle position and properties. The solution is approximated by a linear combination of basis functions. Integrals are approximated using material points as integration points.

In general, linear Lagrangian basis functions are used to approximate the solution equations of motion which has disadvantages. The discontinuity of the gradients of the basis functions may lead to a so-called grid crossing error when particles move through the domain, as will be explained in more detail in Chapter 3. Physical quantities such as stresses are not accurately reproduced. Using the material points as integration points leads to a quadrature error, especially when material points become arbitrarily distributed. Variants of the MPM exist that mitigate these problems. For example, a low-order MPM in which the problems of grid crossing and numerical integration are reduced is presented in [4]. At this moment, Deltares uses this version of the MPM which has been validated with numerous benchmarks.

The use of higher-order basis functions whose gradients are continuous over element boundaries is expected to reduce these numerical problems too, and hence, to lead to a more accurate MPM solution. The use of an alternative numerical quadrature rule is expected to reduce the quadrature error observed within the MPM. Besides a reduction of the numerical problems, a decrease of the computational costs might be achieved with a high-order MPM, when the same accuracy can be achieved as with linear basis functions while using a coarser mesh and/or less material points.

At Deltares, among other geotechnical problems, underwater slope failures are investigated with the MPM. Since such analyses for realistic problem sizes involve more than a million degrees of freedom, long computing times are expected. A reduction of the computational costs is therefore relevant to perform these simulations in reasonable time.

The aim of this master project is to develop a material point method that makes use of higher-order B-spline basis functions and an alternative numerical quadrature rule. As a starting point, the numerical difficulties are examined when using linear and quadratic Lagrange basis functions in a 1D MPM. In a next step, a 1D MPM which makes use of quadratic B-spline basis functions is described. Results of benchmarks are presented. Finally, the numerical quadrature rule used in MPM is adapted for this B-spline approach and results of benchmarks are shown.

DEVELOPMENT OF MPM

The material point method is described as a *mesh-based particle method* since it uses a background mesh and a set of material points moving through this mesh [4].

One of the earliest mesh-based particle methods is the particle-in-cell (PIC) method developed at Los Alamos National Laboratory by F. H. Harlow for fluid dynamics analyses [5]. In this method, material points only carry information on mass and position of the continuum not on velocities or stresses. Dissipation of energy is characteristic for this method [6]. A next step was the introduction of the fluid-implicit particle method (FLIP) by Brackbill and Ruppel [6] in 1986. In this method, not only mass and position but also other properties such as momentum and energy are assigned to each particle. It has been shown in [7] that this method conserves kinetic energy if a consistent mass matrix is used.

In 1993, the FLIP method was extended by Sulsky et al. for problems in solid mechanics that involve history-dependent contitutive models [8]. This new method was called the material point method (MPM) by Sulsky and Schreyer [9]. Within MPM, a material is represented by a set of particles where each particle represents a subvolume of the material. Since these material points store physical properties such as stresses and strains, problems involving history-dependent material behaviour can easier be simulated. Over the years, the material point method has been used in the simulation of a variety of problems in different fields. For example, it has been used to simulate multiphase flows [10] and the deformation of membranes containing soil [11]. Furthermore, the material point method has been used for snow simulations [12] and to model sea ice dynamics [13].

THESIS OUTLINE

In Chapter 2 a short overview of continuum mechanics theory as relevant for this thesis is provided. Furthermore, the chapter contains derivation of the weak formulation of the governing equations. Chapter 3 starts with the space discretization of the weak form as used with the MPM and describes every step of the material point method in detail. Benchmarks considered in this thesis are presented in Chapter 4, involving small and large deformations. Specifically, a vibrating bar and the deformation of a linear-elastic column subjected to loading are considered. The use of Lagrange basis functions is examined in Chapter 5. In particular, linear and quadratic basis functions are considered. In Chapter 6 a 1D MPM is described which makes use of quadratic B-spline basis functions and results are compared for the provided benchmarks. An alternative quadrature rule is introduced in Chapter 7 to decrease the quadrature error observed within MPM. The approach is applied to the benchmarks from Chapter 4 for the benchmarks. In Chapter 8 conclusions are drawn and recommendations are made for future work regarding a high-order MPM.

Throughout this thesis, three versions of the MPM are distinguished. **Linear Lagrange MPM** refers to the classical or original MPM making use of linear Lagrange nodal basis functions as presented in [3]. In case quadratic B-spline basis functions are adopted, this version of MPM is referred to as **B-spline MPM**. The version of MPM which uses quadratic B-spline basis functions for spatial discretization and an alternative quadrature rule is called **Spline based MPM**.

Throughout this thesis, vectors are denoted by boldface lower-case letters. Boldface capital letters refer to matrices and scalars are denoted by an italic letter.

2

MATHEMATICAL MODEL

In this chapter a short overview of continuum mechanics theory is provided as required in this thesis. For a detailed treatment, the reader is referred to [14]. The chapter starts with the description of the Eulerian and Lagrangian frame of reference used to describe the motion of a continuum. After that, a number of definitions and the governing equations are introduced. Then, a description is given of the constitutive relation between stresses and strains for isotropic, homogeneous and linear-elastic material which is considered in this thesis. The chapter ends with the derivation of the weak formulation of the equation of conservation of momentum.

2.1. LAGRANGIAN VS. EULERIAN

Different frames of reference can be adopted to observe motion of a continuum. In the Eulerian frame of reference, a control volume is considered with a fixed position in time. Material is able to move in and out of the control volume. Conservation equations for mass and momentum in describe the inflow and outflow of both mass and momentum into and out of the control volume which must be equal to the change of mass and momentum inside the control volume.

In the Lagrangian frame of reference, a control volume is followed as it moves with time. The control volume always contains the same set of material and can deform in time. Conservation equations for mass and momentum are derived by using the fact that both mass and momentum of this control volume remain constant.

The two frames of reference are illustrated in Figure 2.1. Note that in the Eulerian frame of reference, material can move in and out of the control volume. Therefore the 'walls' of the control volume are permeable. In a Lagrangian frame of reference, this is not the case. If the control volumes are assumed to be infinitely small, this leads to conservation equations in differential form. In this thesis the Lagrangian frame of reference is considered.

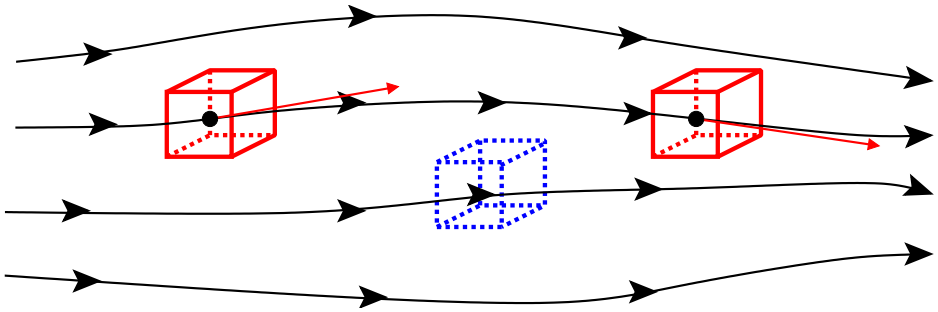

Figure 2.1: The Lagrangian (red) and Eulerian (blue) approach illustrated. Retrieved from [15].

2.2. MOTION AND KINEMATICS

Consider the deformation of a continuum with initial domain Ω_0 at time $t = 0$ s. The configuration Ω_t represents the state of the continuum after deformation at time t and will be referred to as the current configuration. The movement of a material point at initial position $\mathbf{X} \in \Omega_0$ to the position $\mathbf{x} \in \Omega_t$ can be written as:

$$\mathbf{x} = \mathbf{x}(\mathbf{X}, t).$$

Figure 2.2 illustrates the initial and deformed configuration of a continuum for the 2D case. The function $\mathbf{x}(\mathbf{X}, t)$ has a unique inverse denoted by $\mathbf{X}(\mathbf{x}, t)$ which gives the initial position of a point situated at position $\mathbf{x}$ at time t. The displacement $\mathbf{u}(\mathbf{X}, t)$ at time t of a point intially located at position $\mathbf{X}$ is then defined by:

$$\mathbf{u}(\mathbf{X}, t) = \mathbf{x}(\mathbf{X}, t) - \mathbf{X}(\mathbf{x}, t).$$

Velocities and accelerations can be obtained from displacements by taking the total derivative with respect to t:

$$\begin{aligned} \mathbf{v}(\mathbf{X}, t) &= \frac{\mathrm{d}\mathbf{u}}{\mathrm{d}t}(\mathbf{X}, t), \\ \mathbf{a}(\mathbf{X}, t) &= \frac{\mathrm{d}\mathbf{v}}{\mathrm{d}t}(\mathbf{X}, t), \end{aligned}$$

where the material derivative, or total derivative, $\frac{d}{dt}$ is defined as

$$\frac{\mathrm{d}}{\mathrm{d}t} = \frac{\partial}{\partial t} + \mathbf{v} \cdot \nabla. \tag{2.1}$$

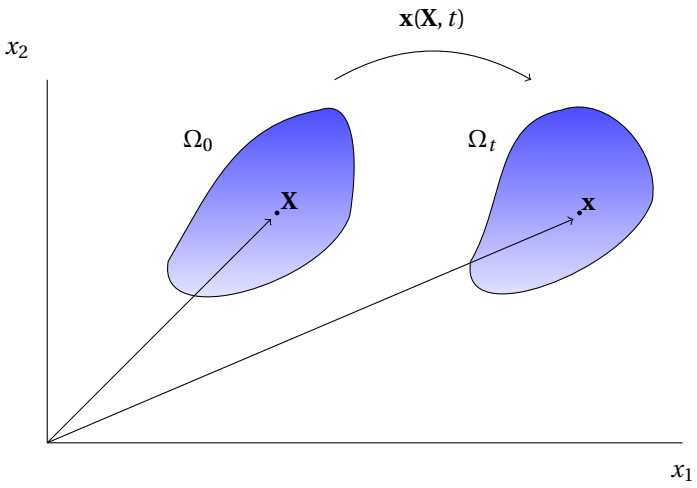

Figure 2.2: Initial and deformed configurations of a continuum.

The strain tensor $\boldsymbol{\epsilon}$ in incremental form is defined in the following way:

$$\frac{\partial \boldsymbol{\epsilon}_{(i,j)}}{\partial t} = \frac{1}{2}\left(\frac{\partial \mathbf{v}_i}{\partial \mathbf{x}_j} + \frac{\partial \mathbf{v}_j}{\partial \mathbf{x}_i}\right), \tag{2.2}$$

where $i, j \in \{1, 2, 3\}$. It defines strain increments with respect to the undeformed state and is applicable in case of small deformations. For large deformations other incremental strain measures exist [14], one of which will be introduced later in Chapter 4.

2.3. GOVERNING EQUATIONS

In this section the conservation equations are presented in differential form. The conservation of mass is given by

$$\frac{\mathrm{d}\rho}{\mathrm{d}t} + \rho\nabla\cdot\mathbf{v} = 0,$$

where $\rho = \rho(\mathbf{x}, t)$ denotes the density and $\mathbf{v} = \mathbf{v}(\mathbf{x}, t)$ the velocity. The equation of conservation of linear momentum is given by [14]

$$\rho\frac{\mathrm{d}\mathbf{v}}{\mathrm{d}t} = \nabla\cdot\boldsymbol{\sigma} + \rho\mathbf{g}.$$

where $\boldsymbol{\sigma}$ denotes the stress tensor and $\mathbf{g}$ the gravitational force. The stress tensor $\boldsymbol{\sigma}$ is assumed here as symmetric. It takes the following form in 3D:

$$\boldsymbol{\sigma} = \begin{bmatrix} \sigma_{(1,1)} & \sigma_{(1,2)} & \sigma_{(1,3)} \\ \sigma_{(2,1)} & \sigma_{(2,2)} & \sigma_{(2,3)} \\ \sigma_{(3,1)} & \sigma_{(3,2)} & \sigma_{(3,3)} \end{bmatrix}.$$

The nine components of the stress tensor define the stresses acting on a single point completely. Figure 2.3 denotes the different components of the stress tensor.

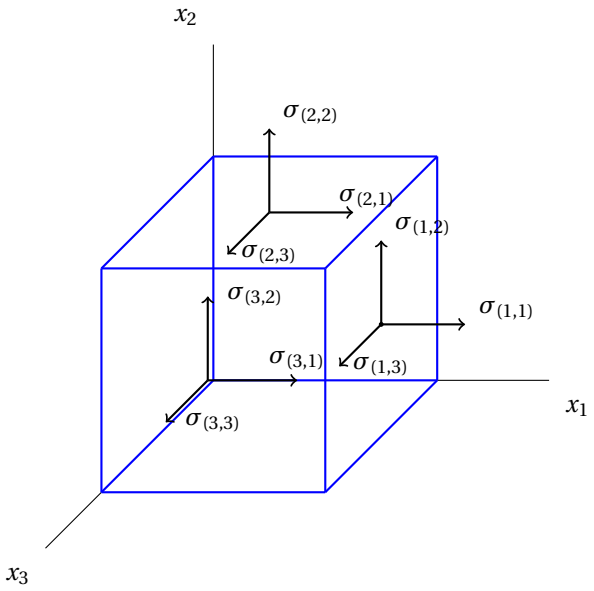

Figure 2.3: Components of the stress tensor.

Since the Lagrangian frame of reference is considered in this thesis, the material derivative reduces to the partial derivative [1]

$$\frac{\mathrm{d}}{\mathrm{d}t} = \frac{\partial}{\partial t}$$

and the conservation equation of mass and linear momentum become respectively:

$$\frac{\partial\rho}{\partial t} + \rho\nabla\cdot\mathbf{v} = 0, \tag{2.3}$$

$$\rho\frac{\partial\mathbf{v}}{\partial t} = \nabla\cdot\boldsymbol{\sigma} + \rho\mathbf{g}. \tag{2.4}$$

2.4. CONSTITUTIVE RELATION

Besides the kinematic relation between $\mathbf{v}$ and $\boldsymbol{\epsilon}$ shown in Equation (2.2), a constitutive relation is needed to relate the stress tensor to the strain tensor. A constitutive relation in incremental form can be written, using Einstein notation, as:

$$\frac{\partial \boldsymbol{\sigma}_{(i,j)}}{\partial t} = D_{(i,j,k,l)} \frac{\partial \boldsymbol{\epsilon}_{(k,l)}}{\partial t}. \tag{2.5}$$

In this thesis, only isotropic linear-elastic material is considered. This implies a linear reversible relationship between stress and strain and material properties that are independent of direction.

For this type of materials, Hooke's law applies:

$$D_{(i,j,k,l)} = \left(K - \frac{2}{3}G\right)\delta_{ij}\delta_{kl} + G\left(\delta_{ik}\delta_{jl} + \delta_{il}\delta_{jk}\right).$$

Here, δ_{ij} denotes the Kronecker delta, K and G denote, respectively, the bulk modulus and shear modulus which are defined as

$$K = \frac{E}{3(1-2\nu)} \quad \text{and} \quad G = \frac{E}{2(1+\nu)},$$

where ν denotes the Poisson ratio and E is the Young's modulus. In this thesis, ν is chosen equal to 0 as only 1D problems are considered. E is varied, depending on the considered benchmark problem.

2.5. BOUNDARY AND INITIAL CONDITIONS

Given the appropriate number of boundary and initial conditions, Equation (2.4) and (2.5) are uniquely solvable. Since Equation (2.4) contains the first-order time derivative of $\mathbf{v}$ and Equation (2.5) the first order time derivative of $\boldsymbol{\sigma}$, initial conditions are needed for displacement, velocity and stress:

$$\begin{aligned} u_i(\mathbf{x},0) &= \tilde{u}_i^0(\mathbf{x}) \\ v_i(\mathbf{x},0) &= \tilde{v}_i^0(\mathbf{x}) \\ \sigma_{(i,j)}(\mathbf{x},0) &= \tilde{\sigma}_{(i,j)}^0(\mathbf{x}) \end{aligned}$$

Equations (2.4) and (2.5) contain only first order space derivatives and, therefore, only one boundary condition is needed for each unknown at the boundary. Two types of boundary conditions are distinguished: displacement (or Dirichlet) and traction (or Neumann) boundary conditions.

It is assumed that at each unknown of the boundary only one of the boundary conditions is applied in each direction, but not both of them.

On $\partial\Omega_u$ the displacement of the continuum is prescribed:

$$u_i(\mathbf{x},t) = \tilde{u}_i(t),$$

while on $\partial\Omega_\tau$ traction is prescribed:

$$\sigma_{(i,j)}(\mathbf{x},t)\, n_j = \tau_i(t).$$

Here, n_j denotes the unit vector normal to the boundary $\partial\Omega$ pointing outward.

2.6. WEAK FORMULATION OF MOMENTUM EQUATION

To solve the conservation of linear momentum, given by Equation (2.4), its the weak formulation is derived. Equation (2.4) is multiplied with a test function $\mathbf{w}$ from a test space $\mathcal{W}$ and integrated over the current configuration Ω_t. The test space $\mathcal{W}$ consists of functions which are sufficiently smooth and zero on the part of the boundary where essential boundary conditions are presented.

$$\int_{\Omega_t} w_i \rho a_i \, \mathrm{d}\Omega = \int_{\Omega_t} w_i \frac{\partial \sigma_{(i,j)}}{\partial x_j} \, \mathrm{d}\Omega + \int_{\Omega_t} w_i \rho g_i \, \mathrm{d}\Omega.$$

The next step is to apply integration by parts and Gauss' theorem:

$$\begin{aligned} \int_{\Omega_t} w_i \frac{\partial \sigma_{(i,j)}}{\partial x_j} \mathrm{d}\Omega &= \int_{\Omega_t} \frac{\partial}{\partial x_j}(w_i \sigma_{(i,j)}) \, \mathrm{d}\Omega - \int_{\Omega_t} \frac{\partial w_i}{\partial x_j} \sigma_{(i,j)} \, \mathrm{d}\Omega \\ &= \int_{\partial\Omega_t} w_i n_j \sigma_{(i,j)} \, \mathrm{d}\Gamma - \int_{\Omega_t} \frac{\partial w_i}{\partial x_j} \sigma_{(i,j)} \, \mathrm{d}\Omega \end{aligned}$$

Hence, we obtain the following equation:

$$\int_{\Omega_t} w_i \rho a_i \, \mathrm{d}\Omega = \int_{\partial\Omega_t} w_i n_j \sigma_{(i,j)} \, \mathrm{d}\Gamma - \int_{\Omega_t} \frac{\partial w_i}{\partial x_j} \sigma_{(i,j)} \, \mathrm{d}\Omega + \int_{\Omega_t} w_i \rho g_i \, \mathrm{d}\Omega.$$

which has to hold for all test functions $\mathbf{w}$ from a test space $\mathcal{W}$. Hence the weak formulation becomes:

Find $\mathbf{a} \in \mathcal{V}$ at each time t such that

$$\int_{\Omega_t} w_i \rho a_i \, \mathrm{d}\Omega = \int_{\partial\Omega_t} w_i n_j \sigma_{(i,j)} \, \mathrm{d}\Gamma - \int_{\Omega_t} \frac{\partial w_i}{\partial x_j} \sigma_{(i,j)} \, \mathrm{d}\Omega + \int_{\Omega_t} w_i \rho g_i \, \mathrm{d}\Omega. \tag{2.6}$$

for all $\mathbf{w} \in \mathcal{W}$.

The space $\mathcal{V}$ is called the trial space and consists of functions which are sufficiently smooth and respect the essential boundary conditions.

2.7. ONE-DIMENSIONAL PROBLEM

When problems in 1D are considered as in this thesis, Equation (2.4) reduces to

$$\rho \frac{\partial v}{\partial t} = \frac{\partial \sigma}{\partial x} + \rho, \tag{2.7}$$

and Equation (2.6) reduces to

$$\int_{\Omega_t} \rho w a \, \mathrm{d}\Omega = w(x)\sigma(x,t)\Big|_0^L - \int_{\Omega_t} \frac{\partial w}{\partial x} \sigma \, \mathrm{d}\Omega + \int_{\Omega_t} \rho w g \, \mathrm{d}\Omega. \tag{2.8}$$

3

MATERIAL POINT METHOD

This chapter introduces the material point method as a numerical method to solve problems involving large deformations. Firstly, a brief overview of the MPM is provided. In the following section, the space discretization is described in detail after which each step within the MPM is discussed. Finally, the numerical problems encountered with the classical MPM are reported.

Since the focus of this thesis is the material point method in 1D, the space discretization and MPM solution are only discussed in 1D. Note that the presented space discretization applies to all MPM variants presented in this thesis.

3.1. FUNCTIONING OF MPM

The material point method is used to numerically solve the partial differential equation that describes deformation processes of continuum bodies. A continuum is represented as a set of material points which store all physical properties of the material such as mass, velocity and stresses.

The solution of the partial differential equation is obtained at the material points. The material points move through the mesh over time, representing the deforming body. In this thesis, also the name *particles* is used to refer to material points.

On the background grid, the equation of conservation of momentum is solved in the same way as with the finite element method (FEM). First, the weak form of the conservation of linear momentum is derived by multiplication with a test function and integration over the domain. The solution of this weak form is then approximated by a linear combination of basis functions, where each basis function is associated with a degree of freedom.

Every time step of the material point method consistist of three steps. At the beginning of a time step, information at the material points is projected onto the background grid. Projection is done by using the material points as integration points to approximate the integrals appearing from the weak formulation.

On the background grid, the equations of motion are solved in an updated Lagrangian frame [3]. Therefore, the nonlinear convective term associated with an Eulerian formulation does not appear. The nodes of the background grid are assumed to move according to a velocity field defined by the velocities at the degrees of freedom. Material points move through the mesh based on the velocity at the particle position.

Once all of the properties of the material points are updated, the grid is redefined while the material points are held fixed. By defining the grid equal to the its initial configuration convection is modeled [3]. Figure 3.1 illustrates a single time step of the material point method.

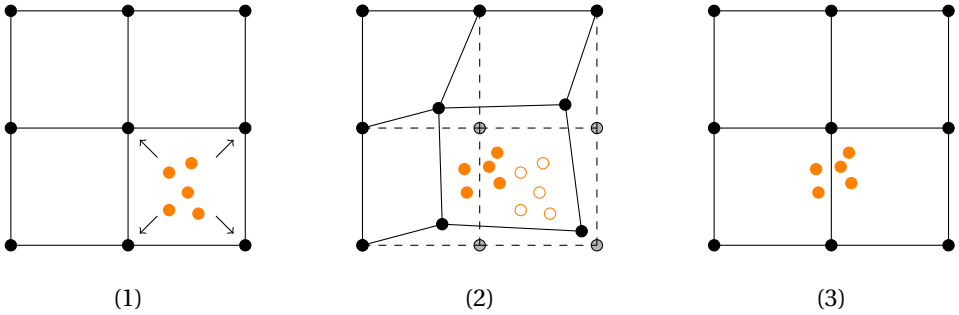

Figure 3.1: The basic concept of the material point method. (1): Project information on background grid. (2): Solve equation of motion on background grid (3): Update particle properties.

If the function value of the basis function is nonzero at a particle position, the degree of freedom associated with this basis function is called *active*. After each time step, the set of active degrees of freedom can change since the material points move through the mesh over time.

3.2. SPACE DISCRETIZATION

Within every time step, Equation (2.8)

$$\int_\Omega \rho w a \, \mathrm{d}\Omega \quad = \quad w(x)\sigma(x,t)\Big|_0^L - \int_\Omega \frac{\partial w}{\partial x}\sigma \, \mathrm{d}\Omega + \int_\Omega \rho w g \, \mathrm{d}\Omega$$

is solved on the background grid. Since the space discretization is identical for all time steps, the time index t is dropped in all equations of this section. Both acceleration a and test function w as well as velocities and displacements, are approximated by a linear combination of basis functions ϕ_j and (discrete) coefficients:

$$a(x) \approx a_h(x) = \sum_{j=1}^{n} \phi_j(x) a_j,$$

$$w(x) \approx w_h(x) = \sum_{i=1}^{n} \phi_i(x) w_i.$$

Since the representation of w_h in terms of the basis functions ϕ_i and coefficients w_i is unique, it suffices to test equation (2.8) only for the basis functions ϕ_i that span the test space $\mathcal{W}$. Hence, the weak formulation becomes:

Find a_h such that

$$\int_\Omega \phi_i \rho a_h \mathrm{d}x = \phi_i(x)\sigma(x,t)\Big|_0^L - \int_\Omega \frac{\partial \phi_i}{\partial x}\sigma \mathrm{d}x + \int_\Omega \phi_i \rho g \mathrm{d}x \tag{3.1}$$

for all $\phi_i \in \mathcal{W}$.

Equation (3.1) can be rewritten by using the definition of a_h and noting that $\frac{\partial \phi_i}{\partial x}$ represents $\nabla \phi_i$:

$$\int_\Omega \phi_i \rho \left(\sum_{j=1}^{n} \phi_j a_j \right) \mathrm{d}x = \phi_i(x)\sigma(x,t)\Big|_0^L - \int_\Omega \nabla\phi_i \sigma \mathrm{d}x + \int_\Omega \phi_i \rho g \mathrm{d}x.$$

After interchanging summation and integration and observing that the coefficients a_j do not depend on x we obtain:

$$\sum_{j=1}^{n}\left(\int_\Omega \phi_i \rho \phi_j \mathrm{d}x\right) a_j = \phi_i(x)\sigma(x,t)\Big|_0^L - \int_\Omega \nabla\phi_i \sigma \mathrm{d}x + \int_\Omega \phi_i \rho g \mathrm{d}x.$$

Since this equality has to hold for all test functions ϕ_i, we obtain:

$$\mathbf{Ma} \quad = \quad \mathbf{F}^{\text{trac}} - \mathbf{F}^{\text{int}} + \mathbf{F}^{\text{grav}}. \tag{3.2}$$

The mass matrix $\mathbf{M}$ and vectors $\mathbf{F}^{\text{trac}}$ containing traction forces, $\mathbf{F}^{\text{int}}$ internal forces and $\mathbf{F}^{\text{grav}}$ gravitational forces are, respectively, defined by

$$\begin{aligned}
\mathbf{M}_{(i,j)} &= \int_\Omega \phi_i \rho \phi_j \mathrm{d}x, \\
\mathbf{F}^{\text{trac}}_{(i)} &= \phi_i(x)\sigma(x,t)\Big|_0^L, \\
\mathbf{F}^{\text{int}}_{(i)} &= \int_\Omega \nabla\phi_i \sigma \mathrm{d}x, \\
\mathbf{F}^{\text{grav}}_{(i)} &= \int_\Omega \phi_i \rho g \mathrm{d}x.
\end{aligned}$$

In MPM, the material points are used as integration points. The weight ω_p of each integration point equals the volume of the particle:

$$\omega_p = V_p.$$

This leads to the following quadrature rule:

$$\int_\Omega f(x)\mathrm{d}x \approx \sum_{p=1}^{n_p} V_p f(x_p).$$

By application of this quadrature rule, the mass matrix and force vectors are approximated in the following way:

$$\begin{aligned}
\mathbf{M}_{(i,j)} &\approx \sum_{p=1}^{n_p} V_p \phi_i(x_p)\rho_p\phi_j(x_p) = \sum_{p=1}^{n_p} m_p \phi_i(x_p)\phi_j(x_p), \\
\mathbf{F}^{\text{grav}} &\approx \sum_{p=1}^{n_p} V_p \phi_i(x_p)\rho_p g \qquad\quad = \sum_{p=1}^{n_p} m_p \phi_i(x_p) g, \\
\mathbf{F}^{\text{int}} &\approx \sum_{p=1}^{n_p} V_p \nabla\phi_i(x_p)\sigma_p,
\end{aligned}$$

where ρ_p, m_p and x_p denote respectively the density, mass and the position of the particle.

3.3. MPM SOLUTION

Define a set of n_p particles representing a $1D$ continuum body in its initial configuration Ω_0. Each particle is assigned an initial position x_p^0, velocity v_p^0, mass m_p^0, volume V_p^0, density ρ_p^0 and stress σ_p^0, with $p \in \{1,2,\dots,n_p\}$.

A grid is defined consisting of n nodes. The domain Ω of the grid is chosen such that $\Omega_t \subset \Omega$ for all t. In this thesis, particles are intially equally distributed and the initial volume of the particles is given by

$$V_p^0 = \frac{L}{n_p},$$

where L denotes the intial length of the continuum. Figure 3.2 shows a discretized domain $\Omega \subset \mathbb{R}$ in which material points are defined equally distributed to represent the initial configuration Ω_0.

Figure 3.2: Discretized domain $\Omega \in \mathbb{R}$ and initial configuration $\Omega_0 \in \mathbb{R}$ consisting of five degrees of freedom and equally distributed particles.

Within every time step the following computation steps are performed:

1. Assemble Equation (3.2) from particle data on the background grid.
2. Solve Equation (3.2) for acceleration $\mathbf{a}$.
3. Update particle properties based on the obtained solution.

ASSEMBLAGE OF EQUATION OF MOTION

Suppose at time t all physical information of the particles is known. To solve Equation (3.2), the particle properties are projected onto the degrees of freedom. The values at the degrees of freedom correspond to the values at the nodes when adopting Lagrangian basis functions. However, as will be shown later this does not apply in the case of B-spline MPM.

As discussed in the previous section projection of the particle properties is achieved by using the particles as integration points:

$$\begin{aligned}
\mathbf{M}_{(i,j)}^t &= \sum_{p=1}^{n_p} m_p \phi_i(x_p^t)\phi_j(x_p^t), \\
\mathbf{F}_{(i)}^{\text{grav},t} &= \sum_{p=1}^{n_p} m_p g \phi_i(x_p^t), \\
\mathbf{F}_{(i)}^{\text{trac},t} &= \sum_{p=1}^{n_p} f_p^{\text{trac},t} \phi_i(x_p^t), \\
\mathbf{F}_{(i)}^{\text{int},t} &= \sum_{p=1}^{n_p} \sigma_p^t V_p^t \nabla\phi_i(x_p^t).
\end{aligned}$$

SOLVE EQUATIONS OF MOTION

Once the mass matrix and force vectors are determined, Equation (3.2) is solved for $\mathbf{a}^t$:

$$\mathbf{a}^t = (\mathbf{M}^t)^{-1}\mathbf{F}^t,$$

where

$$\mathbf{F}^t = \mathbf{F}^{\text{trac},t} - \mathbf{F}^{\text{int},t} + \mathbf{F}^{\text{grav},t}.$$

Instead of the consistent mass matrix, a lumped mass matrix is commonly used within the MPM to reduce the computation time. More explanation about the lumping procedure can be found in Appendix A.2.

UPDATE PARTICLE PROPERTIES

With the *modified Lagrangian algorithm* proposed in [3] the velocity of the particles at the new time level is directly determined from the coefficients a_i^t:

$$v_p^{t+\Delta t} = v_p^t + \Delta t \sum_{i=1}^{n} \phi_i(x_p^t) a_i^t.$$

The velocity at the degrees of freedom is then determined by a density weighted L_2-projection of the velocity field $v(x)$, only known at the position of the particles, onto the finite element space $\mathcal{V}$ spanned by the basis functions ϕ_i. Hence, the following holds:

Find v_h such that

$$\int_{\Omega_t} \rho(x)\, v(x)^{t+\Delta t} \phi_j \mathrm{d}x = \int_{\Omega_t} \rho(x)\, v_h(x) \phi_j(x) \mathrm{d}x \tag{3.3}$$

for all $\phi_j \in \mathcal{V}$.

Using the definition of v_h, we obtain

$$\begin{aligned}
\int_{\Omega_t} \rho(x)\, v(x)^{t+\Delta t} \phi_j \mathrm{d}x &= \int_{\Omega_t} \rho(x) \left(\sum_{i=1}^{n} \phi_i(x)\, v_i^{t+\Delta t} \right) \phi_j(x) \mathrm{d}x \\
&= \sum_{i=1}^{n} \int_{\Omega_t} \rho(x) \phi_i(x)\, v_i^{t+\Delta t} \phi_j(x) \mathrm{d}x \\
&= \sum_{i=1}^{n} \int_{\Omega_t} \rho(x) \phi_i(x) \phi_j(x) \mathrm{d}x\; v_j^{t+\Delta t}
\end{aligned}$$

Since this equality has to hold for all ϕ_j, we obtain the following linear system:

$$\mathbf{P}^{t+\Delta t} = \mathbf{M}^t \mathbf{v}^{t+\Delta t}. \tag{3.4}$$

where

$$\mathbf{P}^{t+\Delta t} = \int_{\Omega_t} \rho(x)\, v(x)^{t+\Delta t} \phi_j \mathrm{d}x.$$

If a lumped mass matrix is used, $v_i^{t+\Delta t}$ can be determined in the following way:

$$v_i^{t+\Delta t} = \frac{\int_{\Omega_t} \rho(x)\, v(x)^{t+\Delta t} \phi_i(x) \mathrm{d}x}{\mathbf{M^L}^t_{(i,i)}}$$

By applying the numerical quadrature rule used in MPM, we obtain:

$$v_i^{t+\Delta t} = \frac{\sum_{p=1}^{n_p} V_p^t \rho_p^t \phi_i(x_p^t) v_p^{t+\Delta t}}{\mathbf{M^L}^t_{(i,i)}} = \frac{\sum_{p=1}^{n_p} m_p \phi_i(x_p^t) v_p^{t+\Delta t}}{\mathbf{M^L}^t_{(i,i)}}.$$

Incremental particle displacements are then computed from the velocity at the degrees of freedom to update the displacement increments of the particles:

$$\Delta u_p^{t+\Delta t} = \Delta t \sum_{i=1}^{n} \phi_i(x_p^t) v_i^{t+\Delta t}.$$

Based on Equations (2.2) and (2.5), the strain increments and stresses of the material points are computed:

$$\begin{aligned} \Delta\epsilon_p^{t+\Delta t} &= \sum_{i=1}^{n} \nabla\phi_i(x_p^t)\Delta u_i^{t+\Delta t}, \\ \sigma_p^{t+\Delta t} &= \sigma_p^t + (E-\sigma_p^t)\Delta\epsilon_p^{t+\Delta t}. \end{aligned}$$

Both particle volume and density are updated based on the strain increment:

$$\begin{aligned} V_p^{t+\Delta t} &= (1+\Delta\epsilon_p^{t+\Delta t})V_p^t, \\ \rho_p^{t+\Delta t} &= \frac{\rho_p^t}{(1+\Delta\epsilon_p^{t+\Delta t})}. \end{aligned}$$

Finally, the position of the particles is updated:

$$x_p^{t+\Delta t} = x_p^t + \Delta u_p^{t+\Delta t}.$$

In Figure 3.3 an overview of the MPM solution is presented. Application of boundary conditions is treated in the next subsection.

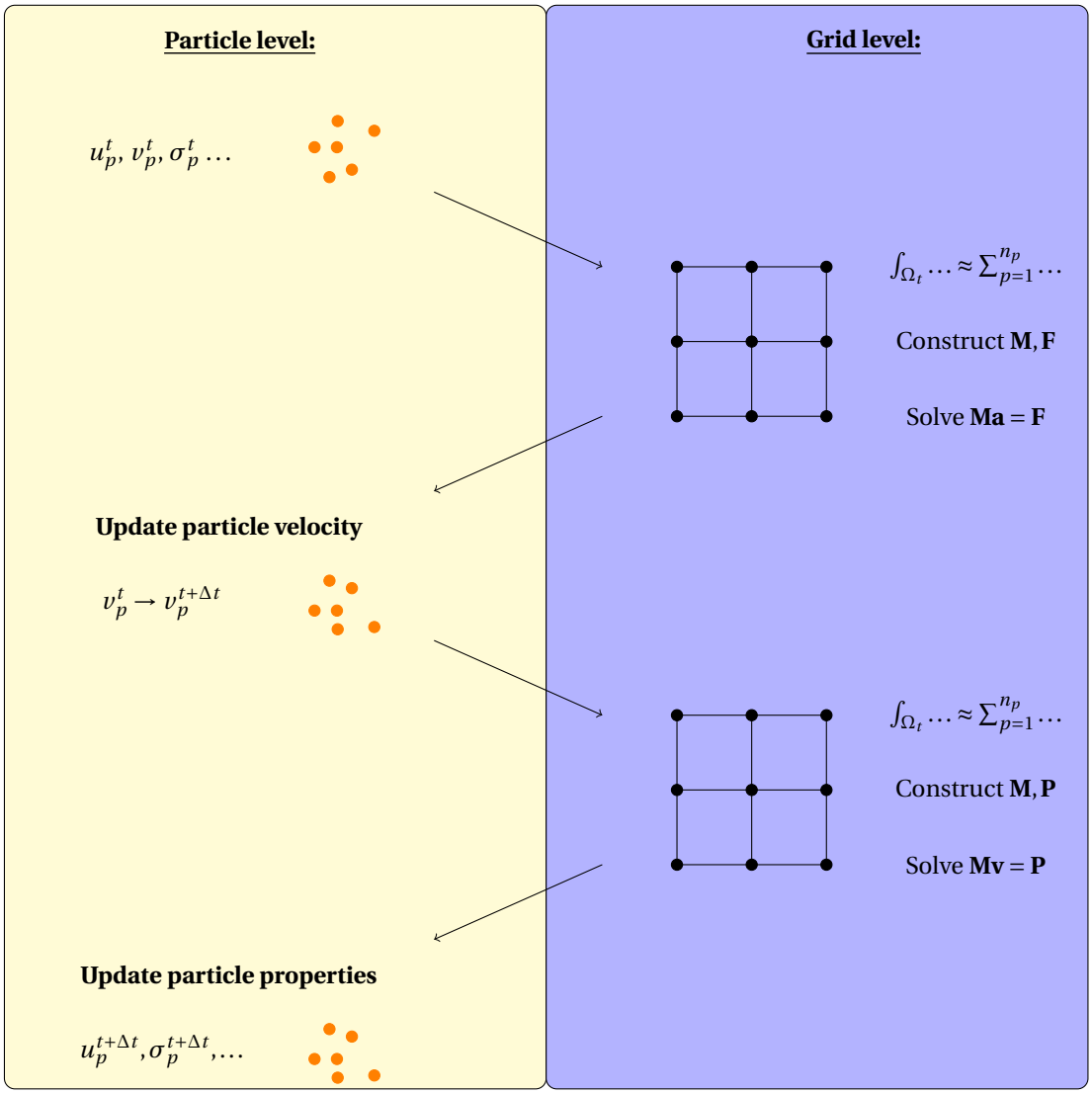

Figure 3.3: Overview of MPM calculation steps of a time step.

BOUNDARY CONDITIONS

In this thesis, both Dirichlet and Neumann boundary conditions are considered. Dirichlet boundary conditions have to be applied on the velocity field and the acceleration field obtained at the background grid. Application of a homogeneous Dirichlet boundary condition is done in the same way as with the FEM. Calculated values for acceleration and velocity at the degree of freedom corresponding to the boundary function are set to zero.

Neumann boundary conditions, or traction boundary conditions, are applied by assigning a traction force f_p^{trac} to particles that are initially located next to the boundary. Traction forces are projected onto degrees of freedom as follows:

$$\mathbf{F}_{(i)}^{\text{trac},t} = \sum_{p=1}^{n_p} f_p^{\text{trac}} \phi_i(x_p^t).$$

A disadvantage of this assignment of boundary conditions is that the traction force is smeared out over multiple degrees of freedom. In [16] and references herein, the concept of a moving mesh is introduced to reduce the smearing error associated with the projection of traction forces.

TIME INTEGRATION SCHEME

The MPM solution presented in this thesis makes use of the semi-implicit Euler-Cromer method. In the following, it is briefly reviewed.

Based on the velocity and acceleration field determined on the background grid, velocity and displacement of the particles are updated in the following way:

$$\begin{aligned} v_p^{t+\Delta t} &= v_p^t + \Delta t \sum_{i=1}^{n} \phi_i(x_p^t) a_i^t, \\ u_p^{t+\Delta t} &= u_p^t + \Delta t \sum_{i=1}^{n} \phi_i(x_p^t) v_i^{t+\Delta t}. \end{aligned}$$

The acceleration at time t is used to explicitly update the particle velocity, whereas the velocity at time $t+\Delta t$ is used to implicitly update the displacement of the particles.

The critical time step size depends on the distribution of the particles with respect to the background grid [17]. Since the particles move through the mesh over time, it is recommended to determine the critical time step size at every time level. In practice, the time step size is chosen such that the CFL (Courants, Friedrich, Lewy) condition is respected [4]:

$$\Delta t \leq \frac{h}{\sqrt{\frac{E}{\rho}}}. \tag{3.5}$$

3.4. NUMERICAL DIFFICULTIES

The use of linear basis functions within MPM has disadvantages. As stated in the introduction, the discontinuity of the basis function derivatives as well as the use of material points as integration points leads to numerical problems. In this section these problems are described in more detail.

GRID CROSSING

Within the original MPM, material points eventually cross the position where the derivative of a basis function is discontinuous. These so-called grid crossings influence the internal forces, masses and external forces calculated at the degrees of freedom. To illustrate this effect at the hand of the internal forces, recall that the internal force at degree of freedom i is calculated in the following way:

$$\mathbf{F}_{(i)}^{\text{int},t} = \sum_{p=1}^{n_p} \sigma_p^t V_p^t \nabla \phi_i(x_p^t).$$

Figure 3.4 denotes a grid consisting of three degrees of freedom, in which four particles are defined. Assume each particle has the same stress σ and volume V, both constant over time. Furthermore, assume the derivative of the basis functions to be equal to -1 or 1. The internal force at degree of freedom 2 is then given by:

$$\mathbf{F}_2^{\text{int,t}} = \sum_{p=1}^{n_p} \sigma V \nabla \phi(x_p^t) = 2\sigma V - 2\sigma V = 0.$$

Suppose one particle crosses x_2 where the derivative of the basis function associated to degree of freedom 2 is discontinuous. The internal force at degree of freedom 2 then suddenly becomes:

$$\mathbf{F}_2^{\text{int,t}} = \sum_{p=1}^{n_p} \sigma V \nabla \phi(x_p^t) = \sigma V - 3\sigma V = -2\sigma V.$$

Hence, grid crossing leads to a non-physical difference in the internal forces.

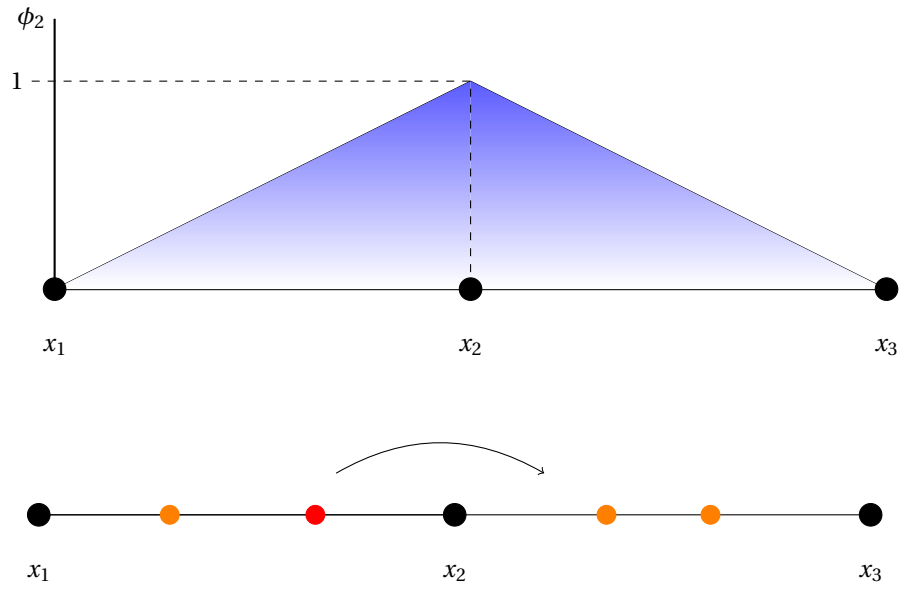

Figure 3.4: Illustration of grid crossing error.

To reduce the effect of grid crossings, Bardenhagen and Kober introduced in [18] a family of methods, named the Generalized Interpolation Material Point (GIMP) methods. The material point method can be seen as a special case of GIMP. While the effect of grid crossings was reduced, an increase of computational time was reported in [19].

In [4] and [20], stresses were determined at fixed Gauss points as the weighted average of particle stresses to reduce grid crossing errors. Other attempts to solve the problems associated with grid crossings were reported in [19], [21] and [22].

In [23] the spatial convergence of the material point method was determined when using different types of basis functions. Besides linear basis functions, both quadratic and cubic B-spline functions were used. When using linear basis functions, a lack of convergence was observed. Both quadratic and cubic B-spline functions showed spatial convergence up to a relatively high number of elements. Therefore, the use of higher-order B-spline basis functions was recommended [23].

QUADRATURE ERROR

In MPM integrals are approximated as follows:

$$\int_{\Omega_t} f(x)\mathrm{d}x \approx \sum_{p=1}^{n_p} V_p^t f(x_p^t).$$

Since material points move through the computational mesh over time, the position of the integration points changes every time step. The particle volume is used to approximate the domain over which integration is performed. This leads to a numerical integration rule of which the quality is uncertain. In general the numerical integration rule used in MPM is not exact.

The use of the particle volume as integration weight leads to a significant quadrature error when a discontinuous function is integrated. Note that within the MPM, the function $\nabla\phi_i$ is integrated to determine the internal force at the degrees of freedom. When Lagrangian linear basis functions are used, $\nabla\phi_i$ is discontinuous. It was shown in [23] that the use of quadratic and cubic B-spline functions reduces this quadrature error. However, using the particles as integration points still leads to a numerical integration rule of which the quality is uncertain.

A solution to this problem might be the use of a numerical integration rule which uses integration points and weights at locations that render accurate integration. This approach is limited however by the fact that physical properties like density and stress are only known at the particle positions. The values of these quantities at integration points have to be approximated from particle data. To do this more elaborately, function reconstruction techniques can be used. With this approach a function is reconstructed based on a finite number of known function values. To obtain an approximation of the quantity of interest at the integration point, the function can be evaluated at this position.

In [2], a weighted least squares approach was used to reconstruct, among other quantities, the density field from the known values at the particle positions. After reconstructing the density field, a one-point Gauss rule was used to approximate the integrals. In Chapter 7, (cubic) spline interpolation will be used as a function reconstruction technique to reduce the numerical quadrature error.

4

BENCHMARKS

In this chapter two 1D benchmarks are presented that will be used to investigate enhancements of the original MPM developed in the frame of this thesis. Obtained results regarding displacement, velocity and stress of particles are compared with a reference solution.

The first benchmark problem considers the longitudinal vibrations of a linear-elastic bar which is fixed at both ends. Displacement of the bar is caused by a prescribed initial velocity. An analytical solution is available for the case of small deformations. Accuracy of the different versions of the MPM is determined based on this solution.For large deformations an ULFEM solution is used as a reference, since no analytical is available.

In the second benchmark, a linear-elastic column subjected to different loading is considered. In Chapter 5, 6 and 7 self-weight is considered. The case of a load applied on top is considered in the Chapter 8. In case of small deformations an analytical solution is available, whereas an ULFEM is used as a reference when considering large deformations.

For the presented benchmarks, both small and large deformations are considered. For small deformations, the maximum strain ϵ is less than 5%. In case the maximum strain exceeds 5% the deformations are considered as large. In general, large deformations involve grid crossing, empty elements and an uneven particle distribution.

For the 1D case Equation (2.3) and (2.5) reduce to

$$\begin{aligned} \rho \frac{\partial v}{\partial t} &= \frac{\partial \sigma}{\partial x} - \rho g, \\ \frac{\partial \sigma}{\partial t} &= E \frac{\partial v}{\partial x} \end{aligned}$$

which is equivalent to the non-homogeneous wave equation [17]:

$$\rho \frac{\partial^2 u}{\partial t^2} = E \frac{\partial^2 u}{\partial x^2} + \rho g.$$

Given benchmark specific boundary and initial conditions, the analytical solution of this equation is used as a reference solution for the different MPM versions discussed in this thesis.

4.1. VIBRATING BAR WITH FIXED ENDS

The first benchmark is concerned with the longitudinal vibrations of a linear-elastic bar which is fixed at both ends. At $t = 0$ s, a prescribed velocity $v_0(x)$ is applied causing the bar to vibrate. Figure 4.1 gives a schematic overview of the vibrating bar problem. In [24] a similar benchmark problem was investigated, where the bar was fixed at only one end.

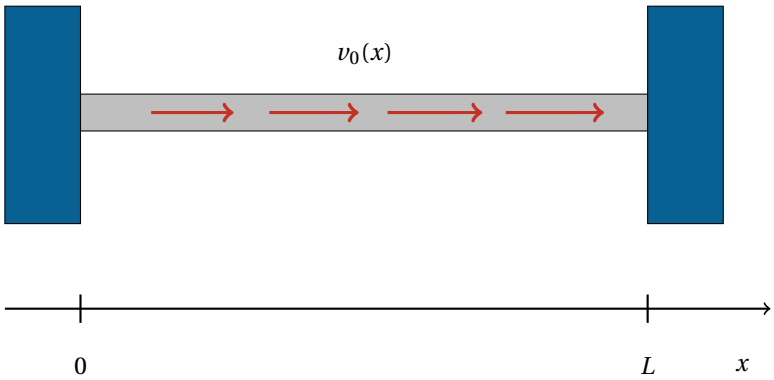

Figure 4.1: The vibrating bar problem.

The analytical solution of the vibrations of a bar with both ends fixed is based on the one-dimensional wave equation [25]

$$\frac{\partial^2 u}{\partial t^2} = \frac{E}{\rho}\frac{\partial^2 u}{\partial x^2},$$

with boundary and initial conditions

$$\begin{aligned} u(0,t) &= 0, \\ u(L,t) &= 0, \\ u(x,0) &= 0, \\ \frac{\partial u}{\partial t}(x,0) &= v_0 \sin\left(\frac{\pi x}{L}\right). \end{aligned}$$

The solution to this equation considering these conditions is

$$u(x,t) = \frac{v_0}{\omega_1}\sin(\omega_1 t)\sin\left(\frac{\pi x}{L}\right), \tag{4.1}$$

where

$$\omega_1 = \frac{\pi\sqrt{\frac{E}{\rho}}}{L}$$

and $\sqrt{\frac{E}{\rho}}$ is the bar's wave velocity. Table 4.1 provides an overview of the chosen parameters for the computation case of small deformations. Adopting these parameters leads to a maximum strain ϵ of 1%.

Quantity	Symbol	Value	Unit
Density	ρ	1	[kg/m^3]
Young's modulus	E	100	[Pa]
Poission ratio	ν	0	[−]
Length	L	25	[m]
Velocity	v_0	0.1	[m/s]

Table 4.1: Parameters used to model small deformations for the vibrating bar problem.

For the case of large deformations, the chosen parameter values are provided in Table 4.2. Adopting these parameter values leads to a maximum strain ϵ of 7%.

Quantity	Symbol	Value	Unit
Density	ρ	25	[kg/m^3]
Young's modulus	E	50	[Pa]
Poission ratio	ν	0	[−]
Length	L	1	[m]
Velocity	v_0	0.1	[m/s]

Table 4.2: Parameters used for to model large deformations for the vibrating bar problem.

4.2. COLUMN UNDER SELF-WEIGHT

The second benchmark considered in the following chapters deals with the deformation of a linear-elastic column due to self-weight. The case of a load applied on top will be considered in Chapter 8. This benchmark represents a realistic problem that is more closely related to geotechnical engineering. A Poisson ratio of 0 is considered rendering a 1D problem which (of course) does not correspond to reality. Figure 4.2 gives a schematic overview of the column.

Suddenly applying a load on the column, self-weight or traction, renders a wave front travelling through the column, which is reflected when reaching its ends. Reproducing such propagation and reflection of waves accurately is numerically challenging. Since it is found in many (dynamic) geotechnical problems, it is a valuable benchmark to consider for assessing the performance of the MPM and its developed variants.

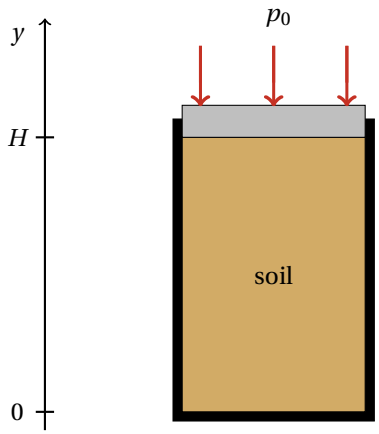

Figure 4.2: The column.

In case of small deformations, a reference solution can be derived from the wave equation[17]:

$$\frac{\partial^2 u}{\partial t^2} = \frac{E}{\rho}\frac{\partial^2 u}{\partial y^2} - g,$$

with initial and boundary conditions:

$$\begin{aligned} u(0,t) &= 0, \\ \frac{\partial u}{\partial y}(H,t) &= \frac{p_0}{E}, \\ u(y,0) &= 0, \\ \frac{\partial u}{\partial t}(y,0) &= 0. \end{aligned}$$

The solution of this partial differential equation with corresponding conditions is given by [17]:

$$u(y,t) = \frac{1}{2}\frac{\rho g y^2}{E} + \frac{(p_0 - \rho g H)y}{E} + \sum_{n=1}^{\infty} u_n \cos\left(\frac{\sqrt{\frac{E}{\rho}}(2n-1)\pi t}{2H}\right)\sin\left(\frac{(2n-1)\pi y}{2H}\right) \tag{4.2}$$

where

$$u_n = \frac{8H(2\pi p_0 n(-1)^n + 2\rho g H - \pi p_0(-1)^n)}{(4n^2-4n+1)(2n-1)\pi^3 E}.$$

When considering large deformations, an analytical solution is not available. Therefore, ULFEM results obtained with a sufficiently high number of degrees of freedom are used as a reference solution. The number of degrees of freedom is chosen such that refinement does not lead to a significant difference in the obtained solution.

The used parameters for the case of small deformations are listed in Table 4.3. When adopting these parameters, the maximum strain ϵ is equal to 0.5%.

Quantity	Symbol	Value	Unit
Density	ρ	1	[kg/m^3]
Young's modulus	E	$5 \cdot 10^4$	[Pa]
Poission ratio	ν	0	[−]
Gravitational acceleration	g	−9.81	[m/s^2]
Column height	H	25	[m]

Table 4.3: Parameters for the case of small deformations.

In case of large deformations, an overview of the parameter values is provided in Table 4.4. The use of these parameter values leads to large displacements, where the maximum strain ϵ is equal to 9%.

Quantity	Symbol	Value	Unit
Density	ρ	$1 \cdot 10^3$	[kg/m^3]
Young's modulus	E	$1 \cdot 10^5$	[Pa]
Poission ratio	ν	0	[−]
Gravitational acceleration	g	−9.81	[m/s^2]
Column height	H	1	[m]

Table 4.4: Parameters used for the case of large deformations.

4.3. NUMERICAL ACCURACY

To determine the quality of the MPM solution, obtained particle displacements are compared with the analytical solution. Errors due to space and time discretization influence the MPM solution, but in this thesis focus lies on spatial convergence. Therefore, the performed benchmark analyses the numerical solution is obtained for very small values of Δt, making the error due to time discretization negligible compared to the spatial discretization error.

The error $|u_h^t - \bar{u}^t|$ between the numerical solution u_h^t and the analytical solution $\bar{u}^t$ at time t is approximated by the Reduced Mean Square (RMS) error:

$$e^{\text{RMS}} = \sqrt{\frac{\sum_{p=1}^{n_p} [u_p^t - \bar{u}(x_p, t)]^2}{n_p}}.$$

A numerical method is said to converge in space with order n if for $\Delta t \to 0$ the reduction of Δx by a factor 2 leads to a reduction of the error $|u_p^t - \bar{u}^t|$ by a factor 2^n. For the FEM, it is known that the use of basis functions of order p leads to spatial convergence is of order $p+1$.

5

LAGRANGE MPM

Based on the general 1D description of the MPM given in Chapter 3 for arbitrary basis functions, in this chapter the MPM is discussed which makes use of Lagrange basis functions. This version of the MPM has been implemented with Matlab. Both linear and quadratic Lagrange basis functions have been considered.

The linear case corresponds to what might be described as the classical MPM and obtained results are used for comparison with the different versions of the MPM presented in the following chapters. The use of quadratic Lagrange basis functions has been investigated in [19], but problems regarding stability where reported. Results for the benchmarks described in Chapter 4 are presented.

5.1. LINEAR LAGRANGE MPM

In case of Lagrangian basis functions, the line segments $[0, L]$ of the vibrating bar and loaded column are discretized by n_e elements with equal element size $h = \frac{L}{n_e}$. For linear basis functions element e_k consists of two nodes k and $k+1$, where the position of node k is denoted by x_k. The nodes and elements are used to define the basis functions. Figure 5.1 illustrates the partition of a line segment.

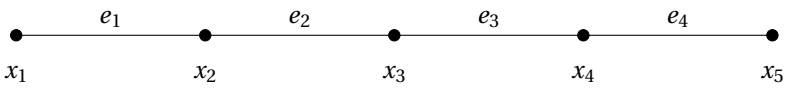

Figure 5.1: Line segment of length L consisting of 4 elements and 5 nodes.

The restriction of a basis function on a single element is called a shape function. A shape function is denoted by N_i and the gradient of a shape function by B_i. Since the elements are pairwise disjoint, the integrals in Equation (3.2) can be evaluated by integrating over the single elements. For example, an arbitrary entry (i, i) of the lumped element mass matrix is given by

$$\mathbf{M}^{\mathbf{L}}_{\mathbf{e}(i,i)} = \int_{e_k} N_i(x)\rho(x)\mathrm{d}x.$$

The lumped mass matrix $\mathbf{M}^{\mathbf{L}} \in \mathbb{R}^{n_n \times n_n}$ and force vectors $\mathbf{F}^{\text{grav}}, \mathbf{F}^{\text{trac}}$ and $\mathbf{F}^{\text{int}} \in \mathbb{R}^{n_n \times 1}$ are then assembled from element matrices and element vectors, as explained in Appendix A.1.

Each element is transformed to a reference element via the mapping

$$\mathrm{T}_{e_k} : e_{\text{ref}} \to e_k$$

defined by

$$\mathrm{T}_{e_k}(\xi) = x_k + (x_{k+1} - x_k)\xi = x_k + h\xi,$$

where $\xi \in [0,1]$. The Jacobian of this transformation is equal to h and thus non-singular for each ξ. The inverse transformation thus exists, it is given by

$$\mathrm{T}_{e_k}^{-1}(x) = \frac{x - x_k}{x_{k+1} - x_k} = \frac{x - x_k}{h}.$$

Figure 5.2 illustrates the mapping T_{e_k} from the reference element e_{ref} to element e_k.

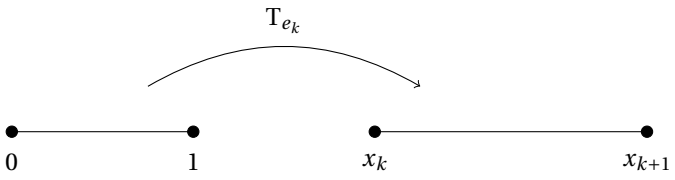

Figure 5.2: Transformation from reference element e_{ref} to element e_k.

If a particle is situated in element e_k at position $x_p \in [x_k, x_{k+1}]$ x_p is referred to as the *global position* of this particle. We define $\xi_p = \frac{x_p - x_k}{x_{k+1} - x_k}$ to be the *local position* of a particle.

Two shape functions are defined on e_{ref} such that for $i, j = 1, 2$.

$$\hat{N}_i(\xi_j) = \delta_{ij}$$

where $\xi_1 = 0$ and $\xi_2 = 1$. Since the values of the shape functions are known at the two nodes, the shape functions are uniquely determined by these nodal values. Hence, on e_{ref} the following shape functions are defined:

$$\begin{aligned} \hat{N}_1(\xi) &= \xi, \\ \hat{N}_2(\xi) &= 1 - \xi, \end{aligned}$$

where $\xi \in [0,1]$. If $x_p \in [x_k, x_{k+1}]$, the relation between the shape functions $\hat{N}_i$ and N_i is given by

$$\hat{N}_i(T_{e_k}^{-1}(x_p)) = N_i(x_p).$$

From the shape functions, a piecewise linear basis function can be constructed for each node. An example of such a basis function is shown in Figure 5.3.

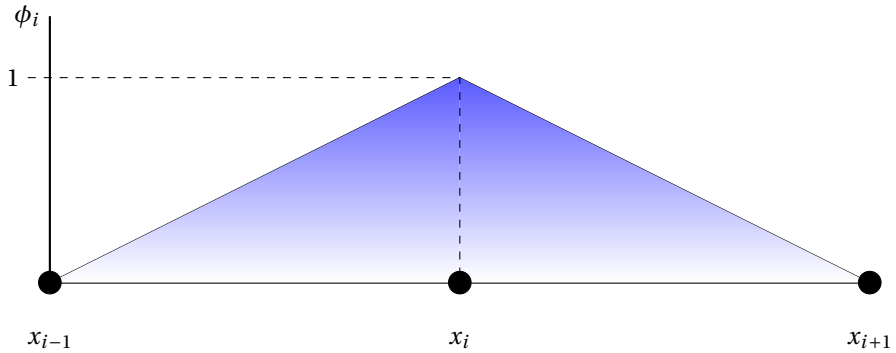

Figure 5.3: Basis function ϕ_i corresponding to node i.

Together with the description of the MPM solution in Chapter 3 this completes the formulation of the linear Lagrange MPM. The two benchmarks described in Chapter 4 have been analysed with it and results are presented in the following sections.

5.1.1. VIBRATING BAR - SMALL DEFORMATIONS

In case of small deformations, the obtained solution for position and velocity over time of a material point is investigated. Furthermore, spatial convergence is determined for the vibrating bar problem using the approach presented in Chapter 4. The used parameter values can be found in Table 4.1. A time step size of $\Delta t = 1 \cdot 10^{-5}$ s was used for all simulations.

Figure 5.4 and 5.5 illustrate respectively the position and velocity of a material point situated directly left of the middle of the vibrating bar with 4 particles per cell and 33 degrees of freedom. The use of a time step size of $\Delta t = 1 \cdot 10^{-5}$ s corresponds, according to Equation (3.5), to a Courant number of $1.28 \cdot 10^{-4}$. There is visually no difference between the MPM solution and the analytical solution. For this benchmark the classical MPM seems to give accurate results.

Figure 5.6 shows the stresses over the bar at time $t = 0.5$ s. Since stresses are updated based on the gradient of the basis functions, the use of linear basis functions leads to a piecewise constant stress field. Therefore, the obtained stress field with linear Lagrange MPM does not correspond well to the exact solution.

In Figure 5.7 the spatial convergence of the material point method that makes use of linear basis functions is shown. Different numbers of particles per cell (PPC) and a different number of degrees of freedom were used in this convergence study. The RMS error was determined at time $t = 0.02$ s. During these simulations, no grid crossings occured before $t = 0.02$ s.

As shown in Table 5.1, the RMS error decreases with increasing number of degrees of freedom as expected. When the domain is discretized by the same number of elements, increasing the number of particles slightly decreases the RMS error.

$n_{dof} - 1$	e^{RMS} 4 PPC	e^{RMS} 6 PPC	e^{RMS} 8 PPC
4	$1.4537 \cdot 10^{-4}$	$1.4363 \cdot 10^{-4}$	$1.4303 \cdot 10^{-4}$
8	$3.7630 \cdot 10^{-5}$	$3.7162 \cdot 10^{-5}$	$3.7002 \cdot 10^{-5}$
16	$9.4898 \cdot 10^{-6}$	$9.3709 \cdot 10^{-6}$	$9.3300 \cdot 10^{-6}$
32	$2.3776 \cdot 10^{-6}$	$2.3478 \cdot 10^{-6}$	$2.3375 \cdot 10^{-6}$
64	$5.9473 \cdot 10^{-7}$	$5.8725 \cdot 10^{-7}$	$5.8469 \cdot 10^{-7}$

Table 5.1: RMS errors with different numbers of degrees of freedom and particles per cell.

The rate of convergence is presented in Table 5.2 in case initially 4 PPC are defined. With linear basis functions quadratic convergence for the vibrating bar problem is obtained when material points hardly move and grid crossing does not occur. Second order convergence for linear Lagrange MPM has also been reported in [2].

$n_{dof} - 1$	$\log_2\left(\frac{e^{\text{RMS}}(h)}{e^{\text{RMS}}(h/2)}\right)$
4	
8	1.9498
16	1.9874
32	1.9969
64	1.9991

Table 5.2: Accuracy of the numerical solution at time $t = 0.02$ s with 4 particles per cell.

Based on these results it can be concluded that linear Lagrange MPM renders well for this benchmark without grid crossing and relatively small movement of the particles. In the next section, when large deformations are considered, the effect of grid crossing is examined.

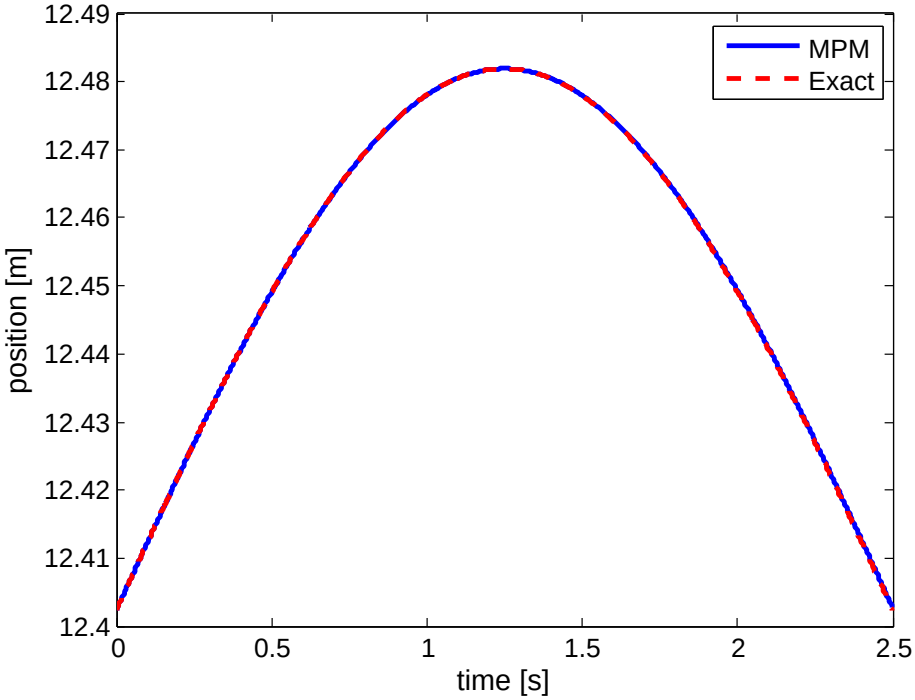

Figure 5.4: Position of the particle situated initially at $x_p = 12.4023$ m, directly left of the middle of the vibrating bar ($L = 25$ m) with 4 particles per cell and 33 degrees of freedom. Grid crossing does not occur.

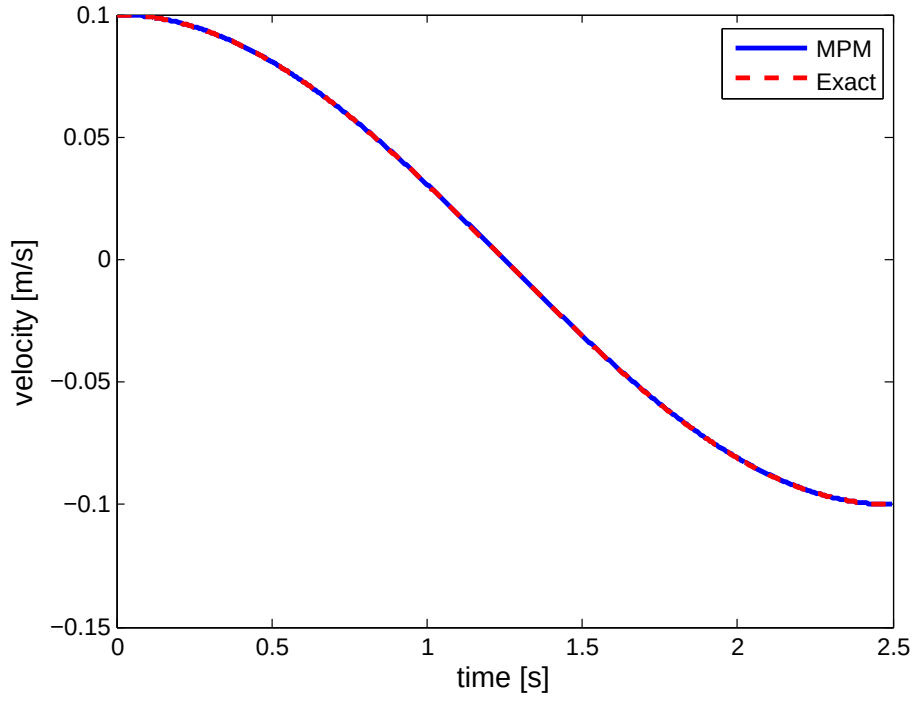

Figure 5.5: Velocity of the particle situated initially at $x_p = 12.4023$ m, directly left of the middle of the vibrating bar ($L = 25$ m) with 4 particles per cell and 33 degrees of freedom. Grid crossing does not occur.

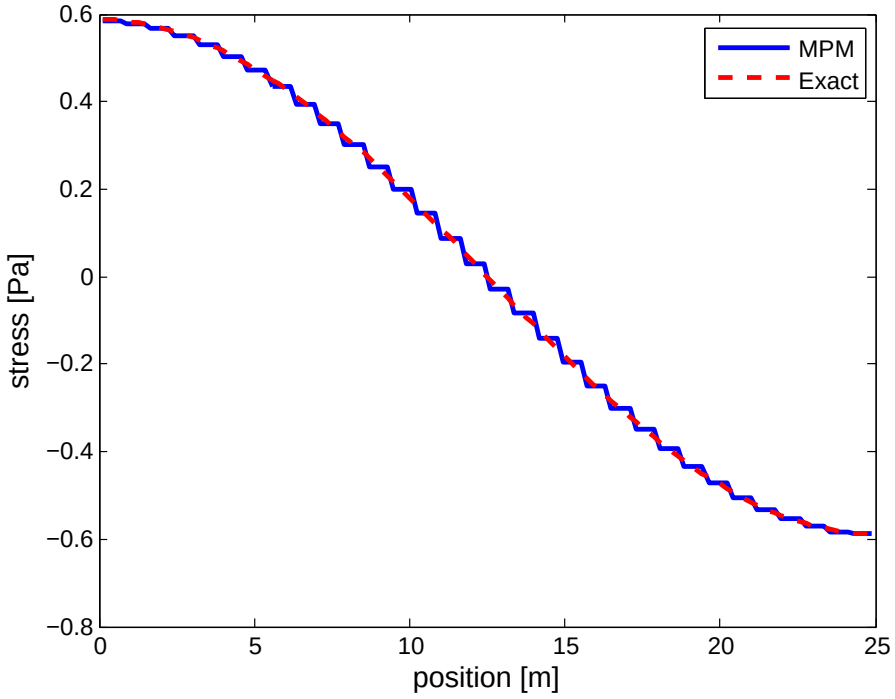

Figure 5.6: Stresses over the bar with linear Lagrange basis functions at time $t = 0.5$ s with 4 particles per cell and 34 degrees of freedom.

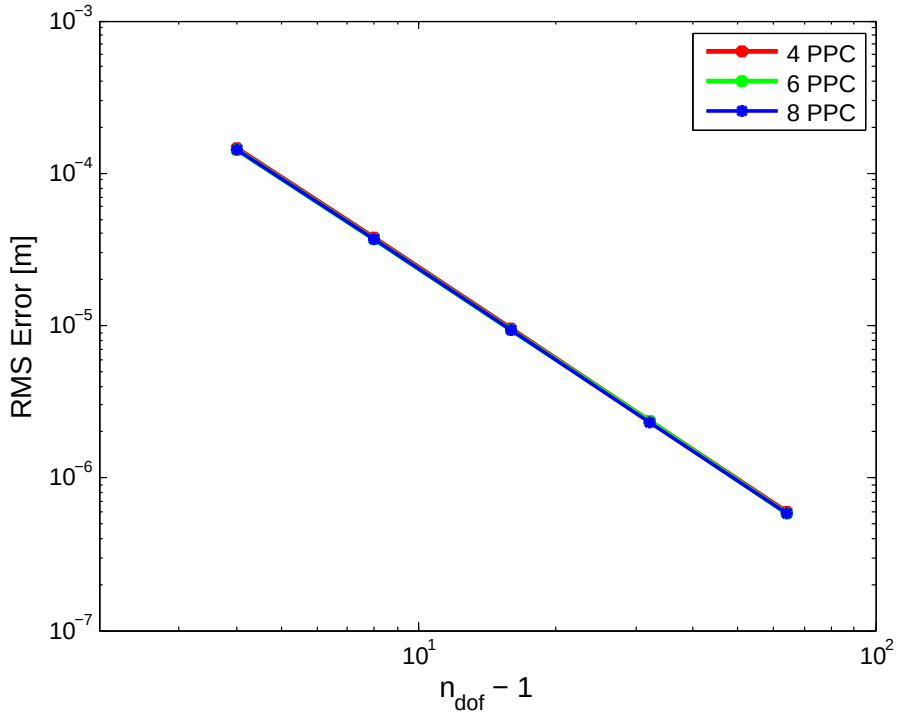

Figure 5.7: Spatial convergence with different numbers of particles per cell at time $t = 0.02$ s.

5.1.2. VIBRATING BAR - LARGE DEFORMATIONS

In case of large deformations, position and velocity of a material point over time is checked. An ULFEM solution is used as a reference solution, since no analytical solution is available. The parameter values presented in Table 4.2 are adopted. Furthermore, a time step size of $\Delta t = 1 \cdot 10^{-5}$ s was used for all simulations.

Figure 5.8 and 5.9 illustrate the position and velocity of a material point situated directly left of the middle of the vibrating bar with 4 particles per cell and 33 degrees of freedom. A time step size of $\Delta t = 1 \cdot 10^{-5}$ s is used, which corresponds to a Courant number of $3.2 \cdot 10^{-3}$.

Compared to the case of small deformations, the quality of the solution for both position and velocity drops. Initially, the MPM solution corresponds to the ULFEM solution. Later on in the simulation grid crossing affects the obtained solution, leading to oscillations in the velocity of the material point. Defining more degrees of freedom does not improve the MPM solution.

Figure 5.10 shows the stresses over the bar at time $t = 0.5$. Due to grid crossing, the stresses start to oscillate severely leading to an unrealistic stress field.

To examine the effect of grid crossing in more detail, the internal force at a single degree of freedom is investigated. Figure 5.11 shows the internal force at a single degree of freedom. Every time a material point passes the discontinuity of the basis function associated with this degree of freedom, a red pulse is shown. Grid crossing has a direct influence on the internal force and, hence, decreases the quality of the MPM solution.

At this moment, it's hard to state to what extend the numerical quadrature rule used in MPM affects the quality of the MPM solution, since both errors occur when the displacement of material points is relatively large. Therefore, grid crossing and the quadrature error occur are strongly connected.

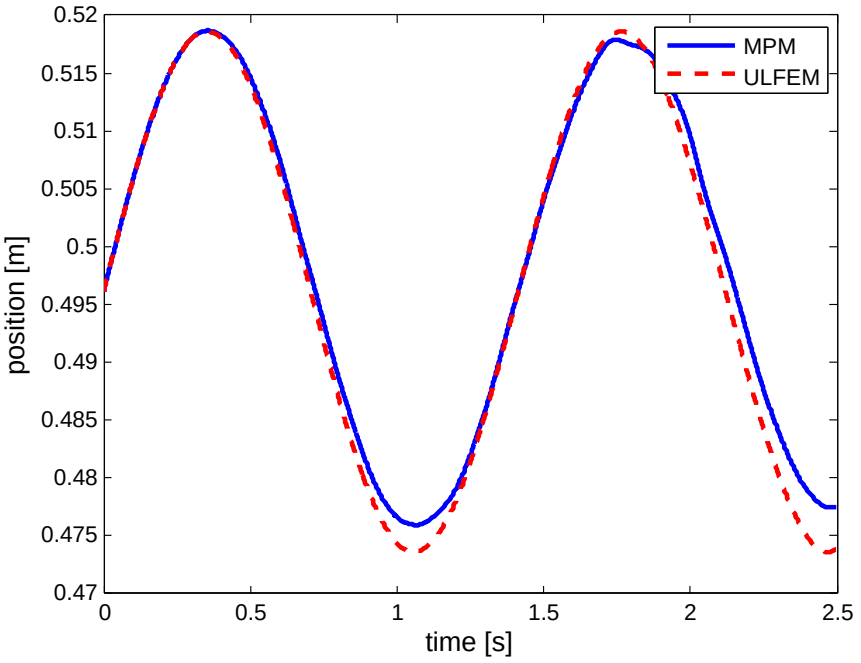

Figure 5.8: Position of the particle initially at $x_p = 0.4961$ m, directly left of the middle of the vibrating bar with 4 particles per cell and 33 degrees of freedom. Grid crossing does occur.

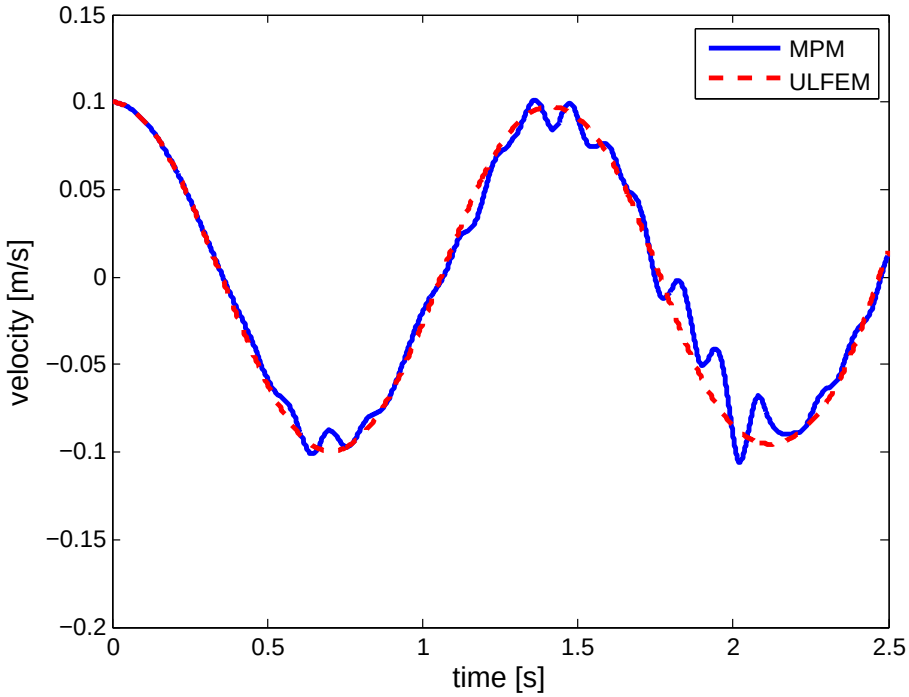

Figure 5.9: Velocity of the particle initially at $x_p = 0.4961$ m, directly left of the middle of the vibrating bar with 4 particles per cell and 33 degrees of freedom. Grid crossing does occur.

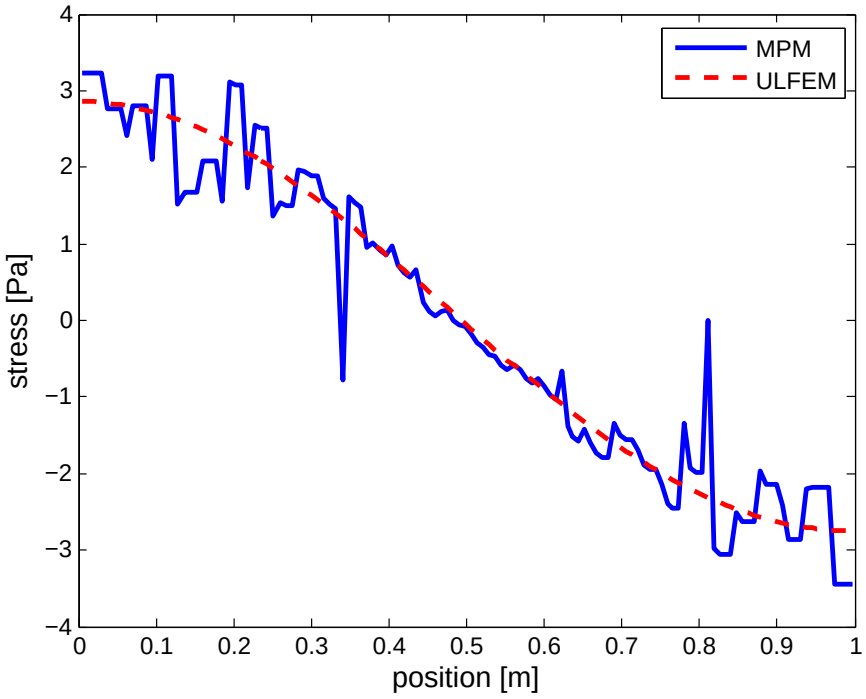

Figure 5.10: Stresses over the bar with linear Lagrange basis functions at time $t = 0.5$ s.

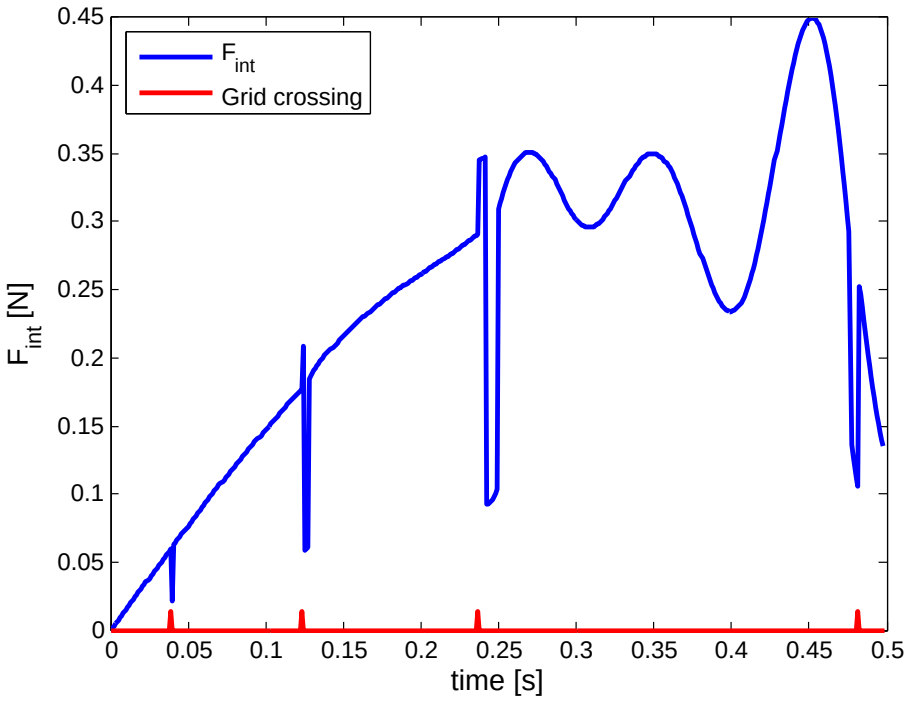

Figure 5.11: Internal force at a single degree of freedom over time. A grid crossing at the discontinuity of the basis functions associated with this degree of freedom is denoted by a red pulse.

5.1.3. COLUMN UNDER SELF WEIGHT - SMALL DEFORMATIONS

Parameter values for the second benchmark problem, a sudden application of self-weight on a column, parameter values are listed in Table 4.3. The reference solution is given by Equation (4.2). The number of degrees of freedom is varied to investigate the influence of grid crossing on the MPM solution. For all simulations a time step size of $\Delta t = 1 \cdot 10^{-4}$ s is used.

Initially, the number of degrees of freedom is set to 50 which corresponds to a Courant number of $4,38 \cdot 10^{-2}$. The number of particles per cell is 2. No grid crossings occur when adopting this number of degrees of freedom. Figure 5.12 shows the position of the material point right underneath the middle of the column. The obtained position is visually identical to the analytical solution.

The velocity of the same material point is shown in Figure 5.13. The MPM solution corresponds well to the reference solution, but at the time intervals during which the velocity at the considered point is constant, it oscillates around the reference solution. These oscillations are also present when using the FEM to obtain a numerical solution.

Figure 5.14 shows the stresses over the column at time $t = 0.5$ s. As a reference, the solution obtained with a ULFEM calculation is used obtained with a sufficiently fine mesh of 99 degrees of freedom. Due to sudden application of the self weight, a wave front travels from the bottom to the top of the column at the material's wave speed. The solution obtained with linear Lagrange MPM corresponds well to the reference solution.

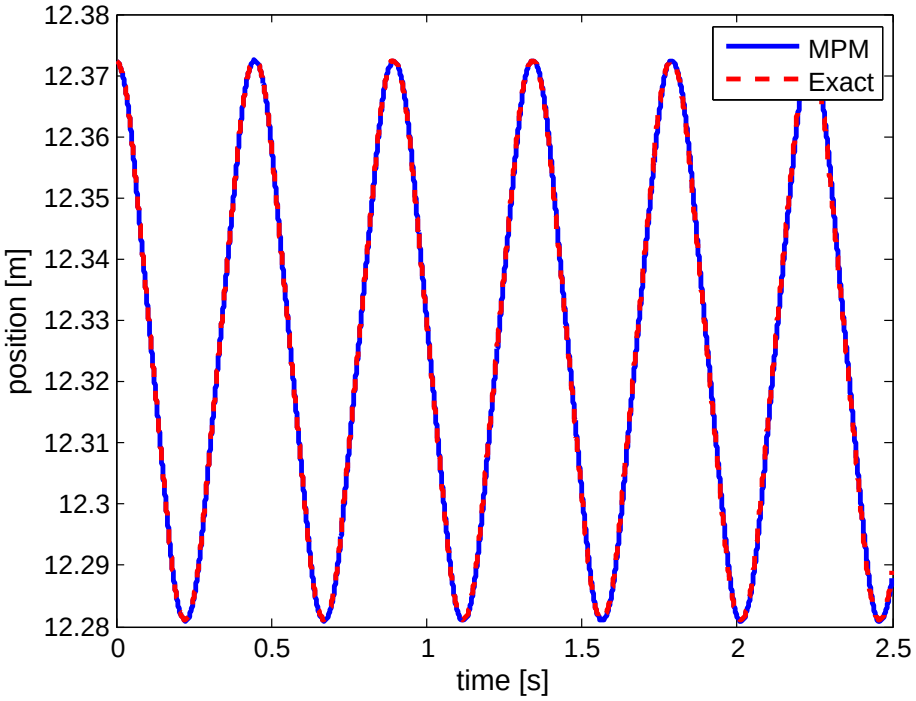

Figure 5.12: Position of the particle situated just underneath the column center with 2 particles per cell and 50 degrees of freedom.

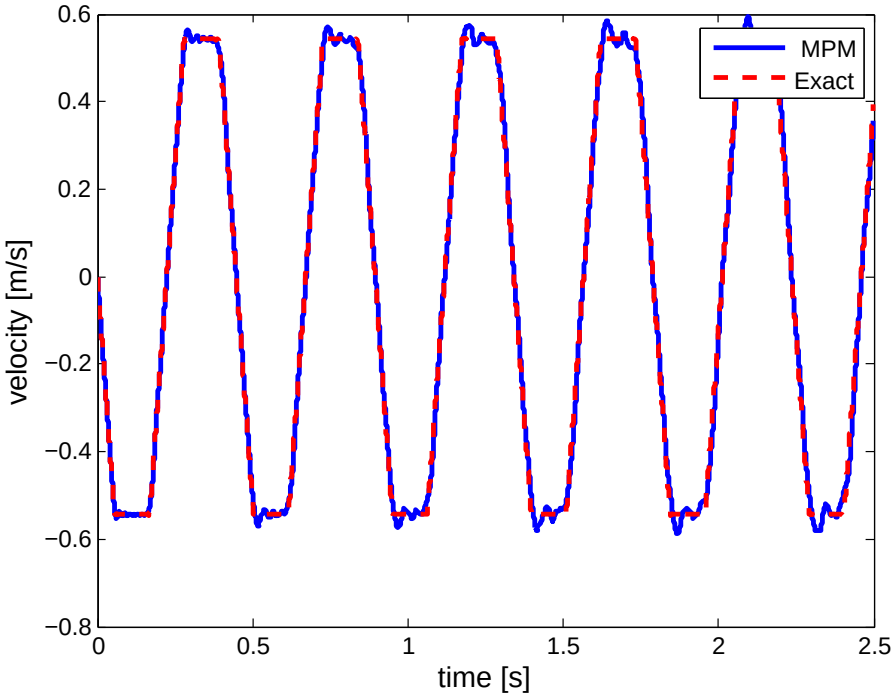

Figure 5.13: Velocity of the particle situated just underneath the column center with 2 particles per cell and 50 degrees of freedom.

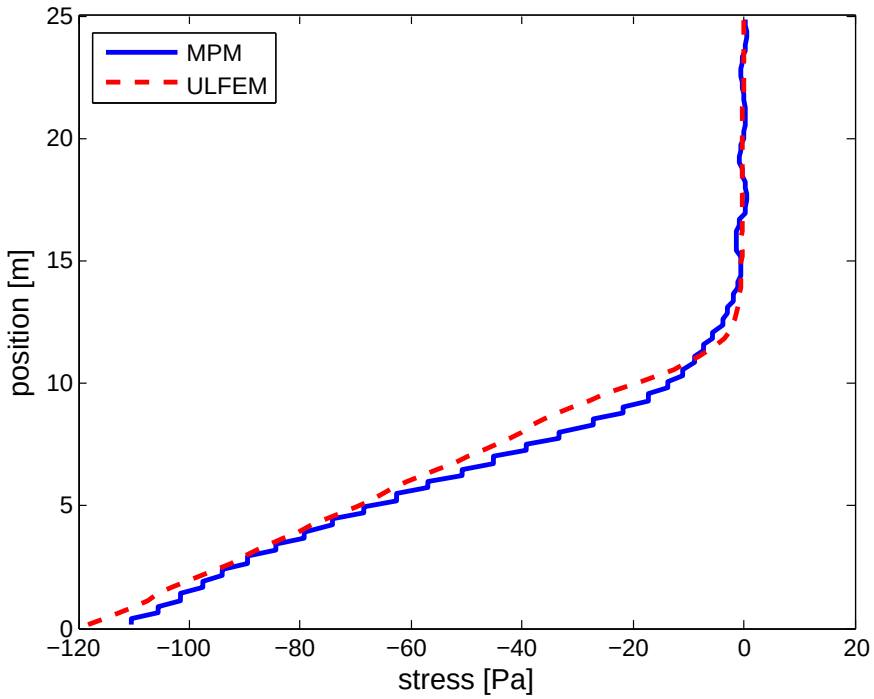

Figure 5.14: Stress over the column at time $t = 0.5$ s with 2 particles per cell and 80 degrees of freedom.

The same calculations were performed with 80 degrees of freedom and a time step size of $\Delta t = 1 \cdot 10^{-4}$ s which results in a Courant number of $7.07 \cdot 10^{-2}$. In contrast to the use of 50 degrees of freedom, grid crossing occurs during the calculations. All the other parameters are kept the same during these simulations.

Figure 5.15 shows the position of the material point right underneath the column center. As with the vibrating bar, the MPM solution now differs from the reference solution and the difference increases over time. In contrast to previous obtained results, the material point does not return to it's original position, indicating that energy is lost during the computations.

The velocity of the same material point is shown in Figure 5.16. Grid crossing leads to severe oscillations around the reference solution. These oscillations are not only present at time intervals where the velocity of the material point is constant, but almost during the entire simulation.

The stress over the column at time $t = 0.5$ s is shown in Figure 5.17. The wave travelling through the column can no longer be reproduced. In fact, the material points attain unrealistic high stresses.

The results show that grid crossing strongly affects the quality of the MPM solution. Position, velocity and stresses can no longer be accurately determined with this version of MPM.

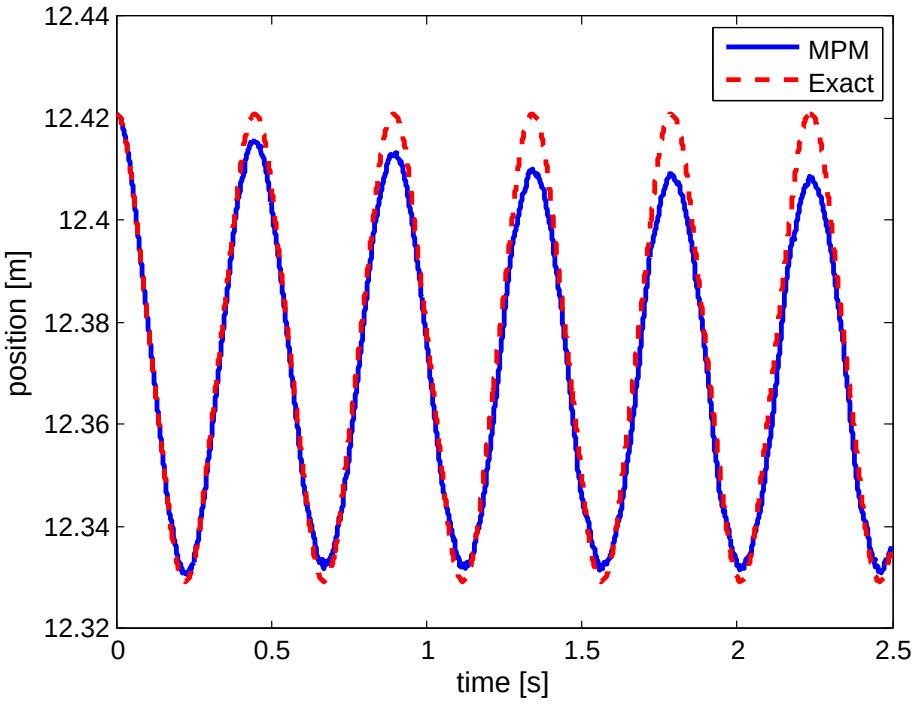

Figure 5.15: Position of the particle situated just underneath the column center with 2 particles per cell and 80 degrees of freedom.

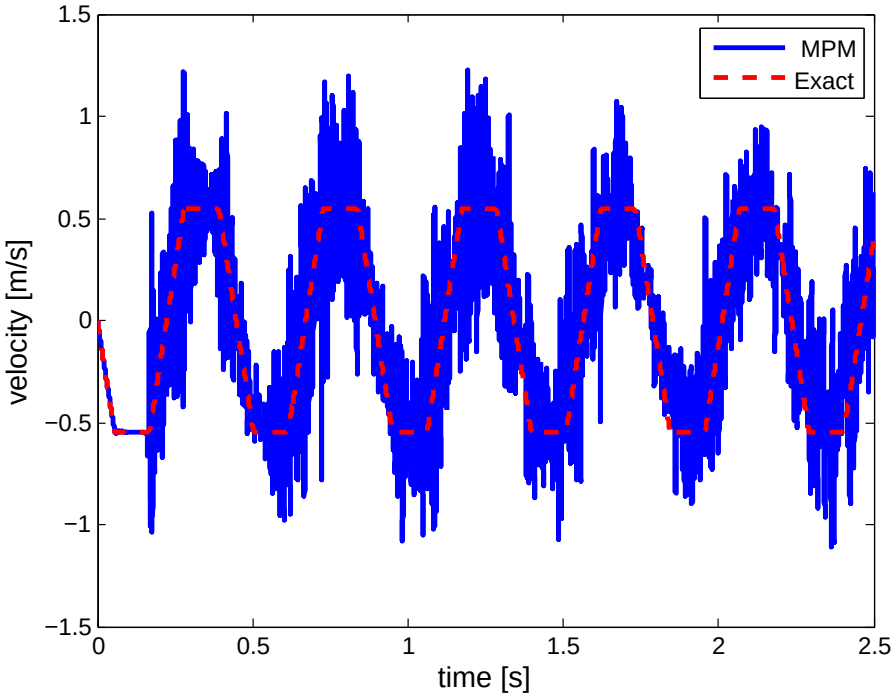

Figure 5.16: Velocity of the particle situated just underneath the column center with 2 particles per cell and 80 degrees of freedom.

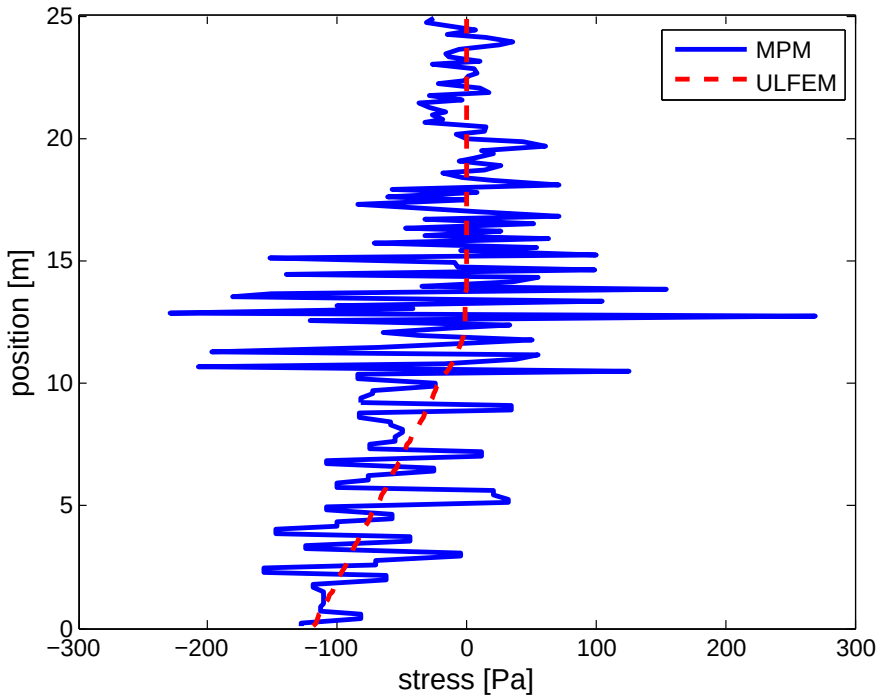

Figure 5.17: Stresses over the column at time $t = 0.5$ s with 2 particles per cell and 50 degrees of freedom.

5.1.4. COLUMN UNDER SELF WEIGHT - LARGE DEFORMATIONS

Sudden application of self-weight on a column leading is considered. The parameter values shown in Table 4.4 are used, leading to large deformations. An ULFEM calculation with 128 degrees of freedom is used as reference solution.

Figure 5.18 and 5.19 denote respectively the position and velocity of the particle situated directly below the center of the column. The number of particles per element was set equal to 4 and the number of degrees of freedom was set to 65. A time step size is used of $\Delta t = 1 \cdot 10^{-4}$ s, which corresponds to a Courant number of $6.5 \cdot 10^{-2}$.

Due to grid crossing, the quality of the MPM solution for both position and velocity drops after approximately 0.05 s. Since the particle does not move back to its initial position, it can be concluded that energy is not conserved during this simulation.

Figure 5.20 shows the stresses over the column at time $t = 0.5$ s. The results obtained with the MPM are compared with an ULFEM calculation. The wave propagating through the column can not be reproduced when using the classical Lagrange MPM. In fact, the stresses attain unrealistically high values.

These results were also confirmed by a numerical study with the Deltares MPM code (Anura 3D) without the application of measures for mitigation of grid crossing errors. As mentioned in Chapter 3, different enhanced variants of MPM exist which reduce these problems.

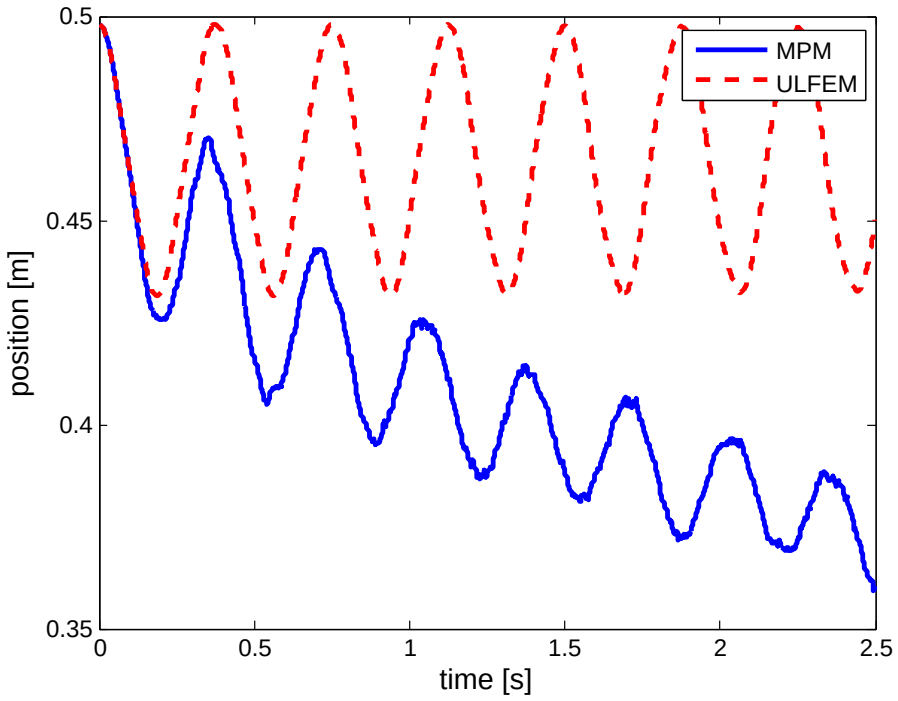

Figure 5.18: Position of the particle situated just underneath column center with 4 particles per cell and 65 degrees of freedom.

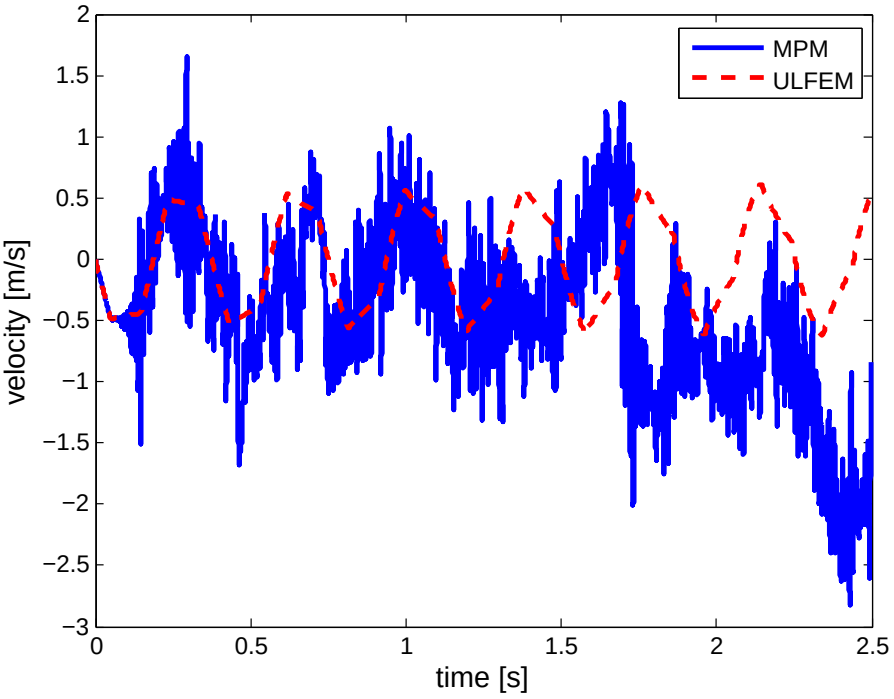

Figure 5.19: Velocity of the particle situated just underneath column center with 4 particles per cell and 65 degrees of freedom.

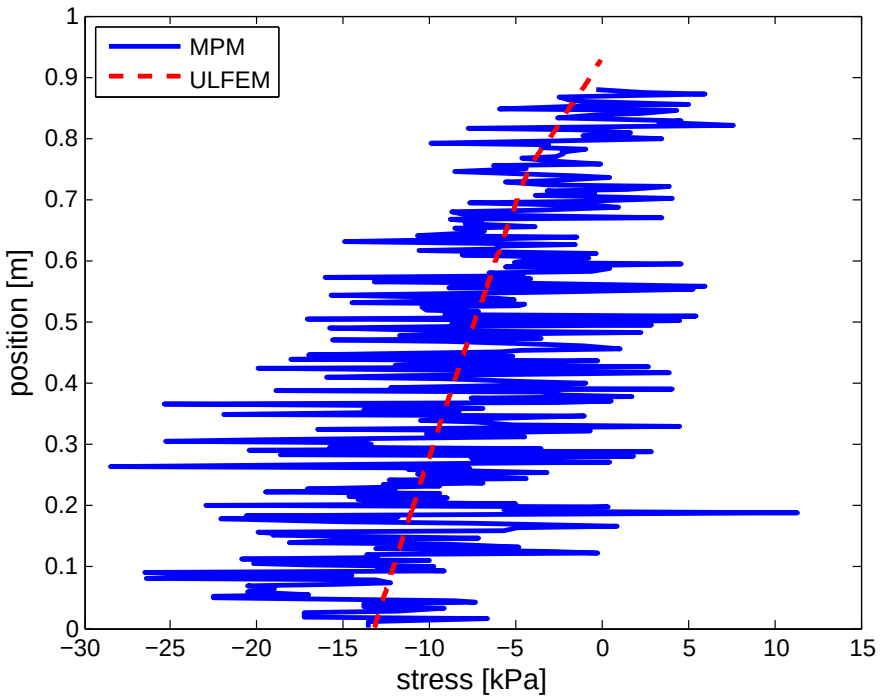

Figure 5.20: Stresses over the column at time $t = 0.5$ s with 4 particles per cell and 65 degrees of freedom.

5.2. QUADRATIC LAGRANGE MPM

In the previous section a version of the MPM was investigated which makes use of linear basis functions. The numerical problems due to the discontinuity of the basis functions were illustrated with results obtained for benchmark problems.

In this section a change of basis functions is presented which makes use of quadratic Lagrange basis functions. The section starts with the introduction of these polynomials. In [19] stability problems where reported when using these basis functions within the MPM. This chapter illustrates these problems and is therefore not meant to present an alternative for the classical MPM.

For quadratic basis functions every 1D element comprises three nodes. The additional node is situated in the middle of an element. Figure 5.21 illustrates the partition of a line segment in three elements.

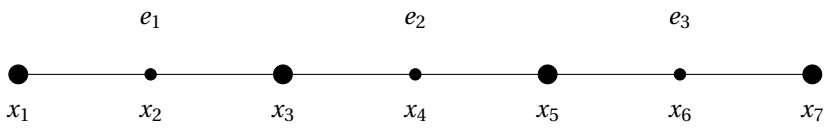

Figure 5.21: Line segment of length L consisting of 3 elements and 7 nodes.

The elements are transformed to a reference element similar to the approach presented in the previous section. The reference element e_{ref} consists of the three nodes x_1, x_2 and x_3. On e_{ref} the following shape functions are defined:

$$\begin{aligned} \hat{N}_1(\xi) &= 2\xi^2 - 3\xi + 1, \\ \hat{N}_2(\xi) &= -4\xi^2 + 4\xi, \\ \hat{N}_3(\xi) &= 2\xi^2 - \xi, \end{aligned}$$

where $\xi \in [0,1]$. The shape functions are shown in Figure 5.22.

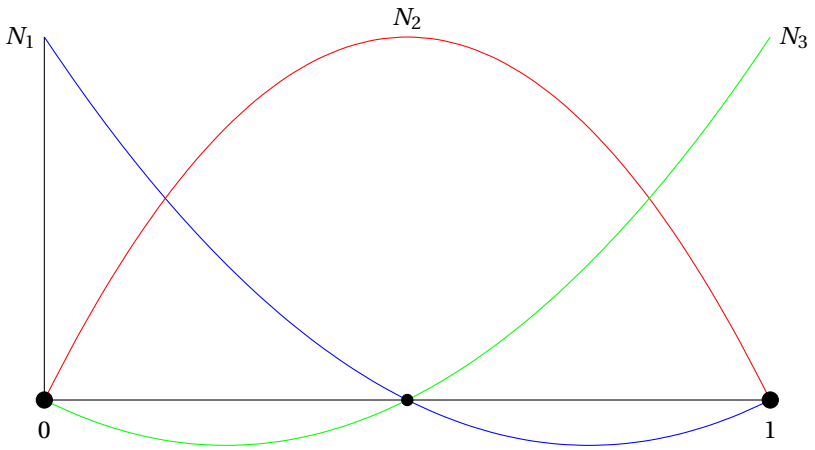

Figure 5.22: Quadratic shape functions defined on reference element e_{ref}.

The shape functions also possess the partition of unity property, implying that for all $\xi \in [0,1]$ we have

$$\sum_{i=1}^{3} \hat{N}_i(\xi) = 1.$$

From the shape functions associated with a node, a basis function can be constructed. Figure 5.23 illustrates a basis function corresponding to a node at the boundary of an element. The basis function is piecewise quadratic and has compact support on $[x_{i-2}, x_{i+2}]$.

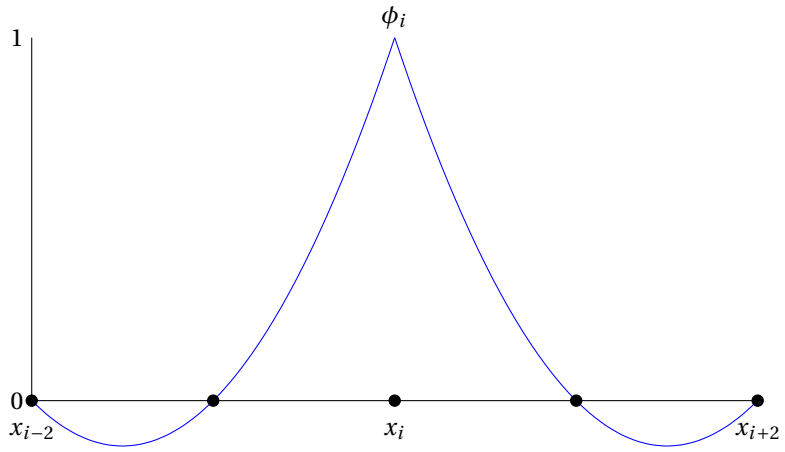

Figure 5.23: Basis function ϕ_i corresponding to node i.

Note that the basis functions corresponding to the nodes at the boundary of an element have a discontinuous gradient. Therefore, the grid crossing error is not expected to be reduced with these type of basis functions. Furthermore, as can be seen from Figure 5.22, the shape functions associated with the nodes at the boundary of an element take negative values on the interval $[0, 1]$.

Since the values of the shape functions at the particle positions are used to determine the element mass matrices, the global mass matrix might contain negative valued entries. Due to these negative values, the lumping procedure described in A.2 can not be applied and solving equation (3.2) becomes relatively expensive. The negative entries in the consistent mass matrix might cause instability of the solution scheme [26].

To illustrate the problems that occur when using Lagrange based quadratic basis functions, the first benchmark is considered. The spatial domain is discretized by 4 elements and each element consists of 100 equidistantly placed material points. Since the solution is only determined at the particle positions with MPM, a relatively high number of PPC is chosen to reconstruct the solution at a specific time. Table 4.1 provides an overview of the used parameter values.

Figure 5.24 shows the displacement of the particles at time $t = 0.5$ s as a function of x with the use of quadratic Lagrange basis functions. For comparison, the displacement obtained with linear basis functions is shown in Figure 5.25. When using linear basis functions the solution differs less from the exact solution.

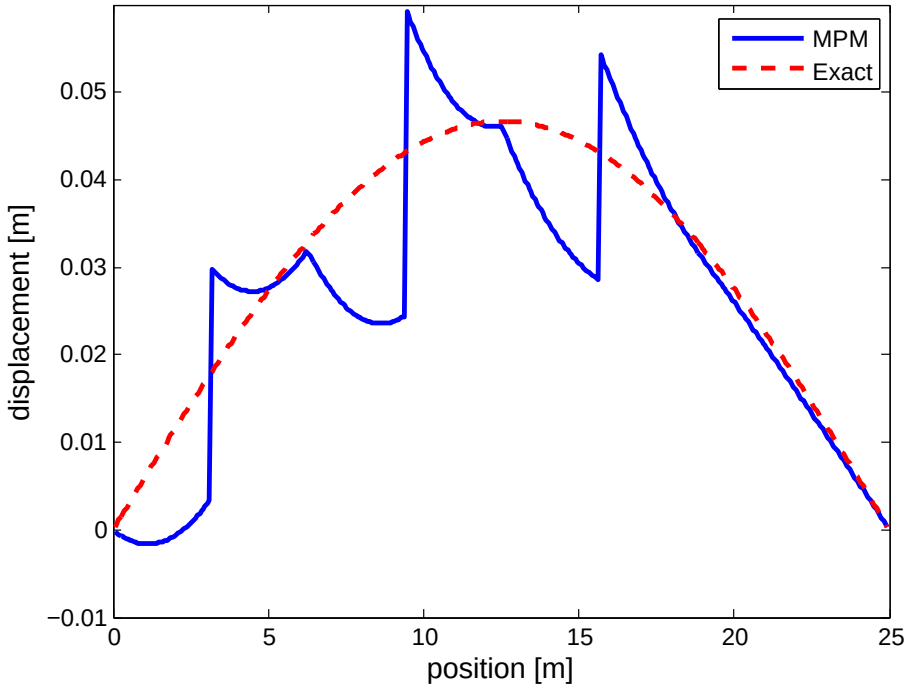

Figure 5.24: Displacement at time $t = 0.5$ s with 4 particles per cell and the use of quadratic Lagrange basis functions.

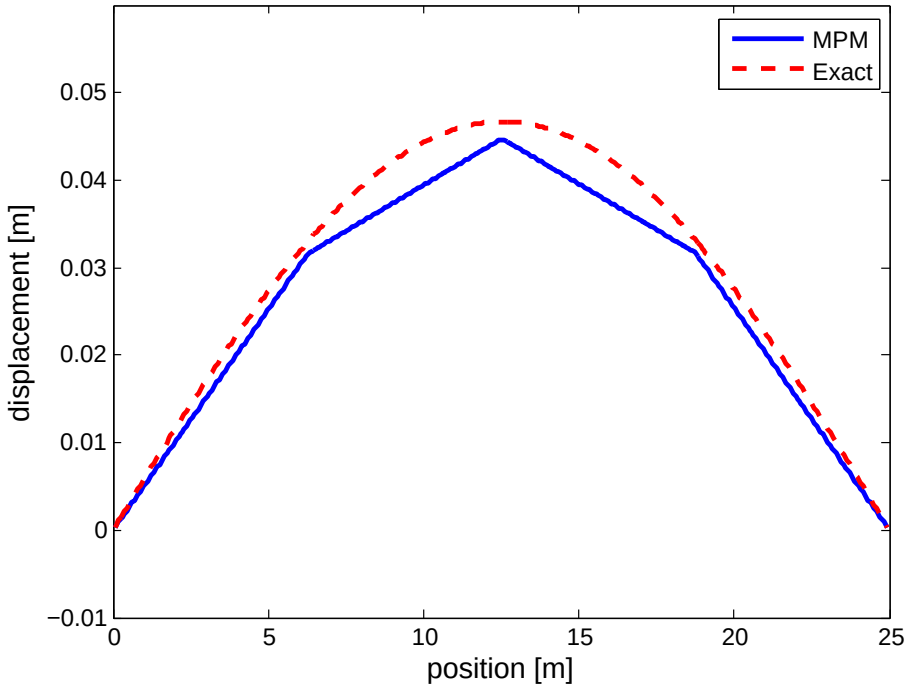

Figure 5.25: Displacement at time $t = 0.5$ s with 4 particles per cell and the use of linear Lagrange basis functions.

5.3. CONCLUSIONS

In this chapter two benchmarks were considered to test the implemented material point method, which uses Lagrange basis functions. Based on the obtained results the following conclusions can be drawn:

- The classical MPM shows second-order convergence when small deformations are considered and grid crossing does not occur. The numerical quadrature rule does not limit the spatial convergence.
- Grid crossing significantly reduces the quality of the MPM solution. The use of linear Lagrange basis functions leads to unrealistic results for the second benchmark when considering large deformations.
- It is hard to state what the influence of the numerical quadrature rule is on the MPM solution, since the quadrature error is strongly connected with grid crossing.
- Using quadratic Lagrange basis functions within the MPM leads to stability problems due to the negative values attained by these basis functions.

Hence, the use of linear or quadratic Lagrangian basis functions leads to numerical problems. Higher-order B-spline basis functions are expected to reduce these numerical problems. The use of these type of basis functions is investigated in the following chapters. The results obtained in this chapter with linear Lagrange basis functions will be used for comparison with the versions of the MPM presented in the following chapters.

6

B-SPLINE MPM

As shown in Chapter 5, the use of Lagrange basis functions within the MPM leads to numerical problems. When considering linear basis functions, grid crossings of the material points affect the accuracy of the numerical solution. Quadratic Lagrange basis functions are no solution as their negative values lead to numerical instabilities and non-physical phenomena (negative mass at degrees of freedom). Furthermore, these basis functions too are discontinuous at boundary nodes, leading to grid crossing errors.

Higher-order basis functions with continuous gradients and strictly positive function values are desirable. In this chapter the use of quadratic B-spline basis functions which fulfill these requirements is discussed. In [23] these basis functions were adopted for a 1D benchmark describing a bar with traction. Numerical experiments showed spatial convergence up to a relatively large number of degrees of freedom when adopting quadratic B-spline basis functions whereas the use of linear Lagrange basis functions lead to a lack of convergence. In this chapter, the use of quadratic B-spline basis functions within MPM is further investigated.

In a first step, a 1D code has been implemented using B-spline basis functions and has been applied to the benchmarks introduced in Chapter 4. Before presenting the developed B-spline MPM a brief introduction to B-spline functions is given. Results with B-spline MPM are presented and compared with the results obtained with the linear Lagrangian MPM and with reference solutions.

6.1. B-SPLINE FUNCTIONS

In the following, a B-spline basis function is denoted by $\phi_{i,d}$, where d denotes the polynomial order of the B-spline. To define B-spline basis functions a *knot vector* is used which consists of a set of points in $\mathbb{R}$ called *knots*. Let $\Xi = \{\xi_1, \xi_2, \ldots, \xi_{n+d+1}\}$ be a knot vector, where n denotes the number of basis functions. If the knots ξ_i are equally distributed the knot vector is said to be *uniform*. More than one knot might be positioned at the same location. These knots are referred to as *repeated* knots. A knot vector is called *open* if ξ_1 and ξ_{n+d+1} are repeated $d+1$ times.

B-spline basis functions can be defined recursively by using the Cox-de Boor recursion formula [27]. The constant basis functions ($d = 0$) are defined in the following way:

$$\phi_{i,0}(\xi) = \begin{cases} 1 & \text{if } \xi_i \leq \xi < \xi_{i+1} \\ 0 & \text{else.} \end{cases}$$

Higher-order B-spline basis functions are then defined by

$$\phi_{i,d}(\xi) = \frac{\xi - \xi_i}{\xi_{i+d} - \xi_i}\phi_{i,d-1}(\xi) + \frac{\xi_{i+d+1} - \xi}{\xi_{i+d+1} - \xi_{i+1}}\phi_{i+1,d-1}(\xi),$$

where $\xi \in [\xi_1, \xi_{n+d+1}]$.

The nonzero intervals $[\xi_i, \xi_{i+1})$ are called *knot spans*. Given an open uniform knot vector of length $n+d+1$, the number of knot spans is equal to $n-d$.

In case of an open uniform knot vector, the basis functions for $d = 1$ are the same as the piecewise linear basis functions used in Chapter 5. Figure 6.1 denotes the linear and quadratic B-spline basis functions defined by an open uniform knot vector on the interval $[0,1]$, where the number of basis functions n is equal to 6. In case of an open uniform knot vector, the basis functions are interpolary at the ends of the interval. Furthermore, all the basis functions are equal to zero at the left and right boundary except the boundary basis functions. An open uniform knot vector will be considered when adapting the MPM.

The B-spline basis function $\phi_{i,d}$ is nonzero on the interval $[\xi_i, \xi_{i+d+1}]$. Hence, the width of the interval where B-spline basis functions are nonzero depends on the order of the basis function. B-spline basis functions of order d defined by a uniform knot vector are C^{d-1}-continuous. However, if a knot is repeated k times, the basis functions become C^{d-k-1}-continuous. To illustrate this, Figure 6.2 denotes the quadratic B-spline basis functions defined by the open non-uniform knot vector $\Xi = \{0,0,0,1,2,3,4,4,5,5,5\}$. Due to the repeated knots ξ_7 and ξ_8 at $\xi = 4$, the basis functions are C^0-continuous at this location.

An important property of B-spline basis functions is the fact that for all $\xi \in [\xi_1, \xi_{n+d+1}]$ we have

$$\phi_{i,d}(\xi) \geq 0.$$

Furthermore, the basis functions possess the partition of unity property. For all $\xi \in [\xi_1, \xi_{n+d+1}]$ and d fixed we have

$$\sum_{i=1}^{n} \phi_{i,d}(\xi) = 1.$$

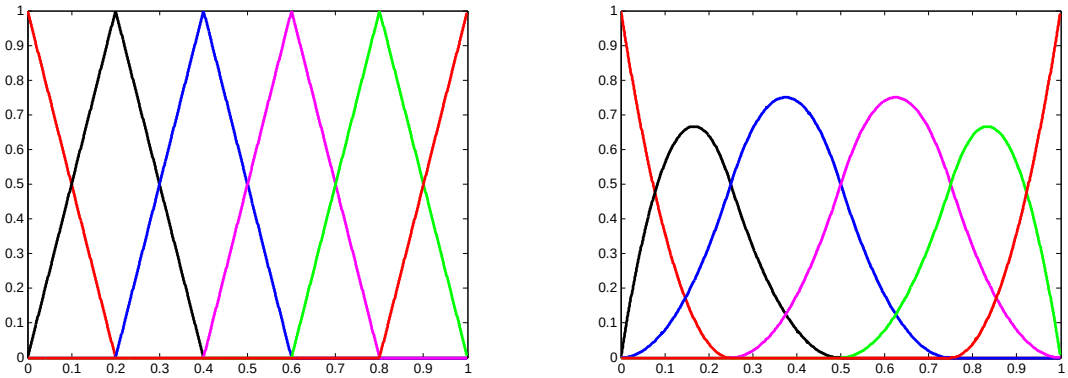

Figure 6.1: Linear and quadratic B-spline basis functions defined by an open uniform knot vector with $n = 6$.

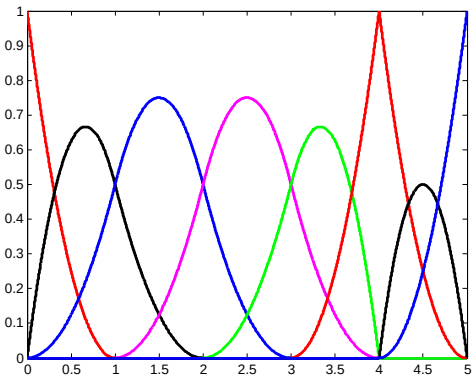

Figure 6.2: B-spline basis function $\phi_{i,2}$ based on the knot vector $\Xi = \{0,0,0,1,2,3,4,4,5,5,5\}$ with discontinuity at $\xi = 4$.

6.2. B-SPLINE MPM

Based on the initial length L of the vibrating bar and loaded column and the number of basis functions n, the knot vector can be written in the following way:

$$\Xi = \{0,0,0,\alpha,2\alpha,\ldots,(n-4)\alpha,(n-3)\alpha,L,L,L\},$$

where $\alpha = \frac{L}{(n-2)}$.

The use of B-spline basis functions renders a significant difference with regard to the space discretization commonly used with the MPM. Basis functions are completely determined by the knot vector Ξ, elements or nodes are no longer used to define the basis functions.

A discretization of the domain with elements and nodes would give some practical problems when adopting B-spline basis functions. For example, the basis functions do not respect the following property at the nodes:

$$\phi_i(x_j) = \delta_{ij},$$

except at the boundary. Therefore, the finite number of coefficients do no longer correspond to the values at the position of the node:

$$a^t(x_j) = \sum_{i=1}^{n} \phi_i(x_j) a_i^t \neq a_j^t.$$

Furthermore, the support of quadratic B-spline basis function ϕ_i is given by the interval $[\xi_i, \xi_{i+3}]$, which does not correspond in general with element boundaries.

In practice, the domain is therefore no longer discretized by elements or nodes. This has the following consequences with regard to the MPM:

- The projection of particle properties on the background grid should no longer be interpreted as a projection on nodes, but as a projection on the degrees of freedom.
- "Grid crossing" should be interpreted as the movement of a material point across the discontinuity of a basis function.
- Integrals are no longer computed separately over distinct element domains but over the entire domain by summation over all particles. Hence, the assembly procedure described in Section A.1 is no longer used.
- The analogue of mesh refinement is knot insertion [28]. With knot insertion, the number of knots is increased to define more basis functions. As a consequence, spatial convergence is determined by increasing the number of knot spans instead of the number of elements.

Since only the boundary basis functions are nonzero at the boundary, implementation of the boundary conditions does not change. To determine the Courant number, the element size can no longer be used. Instead, the lenght of the knot spans is used, which are all equal since a uniform knot vector is used. The description of the MPM solution in Chapter 3 still applies when adopting B-spline basis functions.

6.2.1. VIBRATING BAR - SMALL DEFORMATIONS

For small deformations, the obtained solution for the position and velocity of a material point is investigated. Furthermore, spatial convergence is determined using the analytical solution. The parameter values used in these simulations can be found in Table 4.1. A time step size was used of $\Delta t = 1 \cdot 10^{-5}$ s for all simulations. Quadratic B-spline basis functions are used, defined by the open uniform knot vector presented in the previous section.

Figure 6.3 and 6.4 illustrate respectively the position and velocity of the particle situated directly left of the middle of the vibrating bar with 4 particles per cell and 34 degrees of freedom. Since a time step size of $\Delta t = 1 \cdot 10^{-5}$ s is used, this corresponds to a Courant number of $1.28 \cdot 10^{-4}$. Visually, there is no difference with the results obtained in Chapter 5, see Figure 5.4 and 5.5. The B-spline MPM would seem to render for this benchmark equally well.

Figure 6.5 shows the stresses over the bar at time $t = 0.5$ s obtained with B-spline MPM. The use of quadratic basis functions leads to a piecewise linear stress field. At the boundary the stresses oscillate, leading to a less accurate representation of the stress field. Increasing the number of degrees of freedom reduces the oscillations at the boundary. These oscillations are not present when adopting linear Lagrange basis functions.

In Figure 6.6 results of a spatial convergence study at time $t = 0.02$ s are shown. The number of degrees of freedom was varied between 6 and 66. Initially 4 particles per cell were defined in each knot span. As expected, the RMS error decreases with increasing number of degrees of freedom. However, for all number of degrees of freedom considered in this study the RMS error is lower when adopting linear Lagrange basis functions. The RMS errors for 4 particles per cell are presented in Table 6.1. In contrast with linear basis functions, the B-spline MPM does not show quadratic convergence for the vibrating bar problem.

$n_{\text{dof}} - p$	$\log_2\left(\frac{e^{\text{RMS}}(h)}{e^{\text{RMS}}(h/2)}\right)$
4	
8	1.2784
16	1.5499
32	1.5910
64	1.6067

Table 6.1: Accuracy of the numerical solution at time $t = 0.02$ s with 4 particles per cell.

Table 6.2 shows the RMS error for different degrees of freedom and particles per cell. Increasing the number of particles per cell does not decrease the RMS error when the number of degrees of freedom is the same. A possible explanation for this might be the oscillations in stresses at the boundary affecting the quality of the B-spline MPM solution.

$n_{dof} - p$	e^{RMS} - 4 PPC	e^{RMS} - 6 PPC	e^{RMS} - 8 PPC
4	$1.6123 \cdot 10^{-4}$	$1.6140 \cdot 10^{-4}$	$1.6147 \cdot 10^{-4}$
8	$6.6466 \cdot 10^{-5}$	$6.6895 \cdot 10^{-5}$	$6.7050 \cdot 10^{-5}$
16	$2.2700 \cdot 10^{-5}$	$2.2899 \cdot 10^{-5}$	$2.2970 \cdot 10^{-5}$
32	$7.5351 \cdot 10^{-6}$	$7.6116 \cdot 10^{-6}$	$7.6389 \cdot 10^{-6}$
64	$2.4741 \cdot 10^{-6}$	$2.4995 \cdot 10^{-6}$	$2.5086 \cdot 10^{-6}$

Table 6.2: RMS-errors with different degrees of freedom and particles per cell.

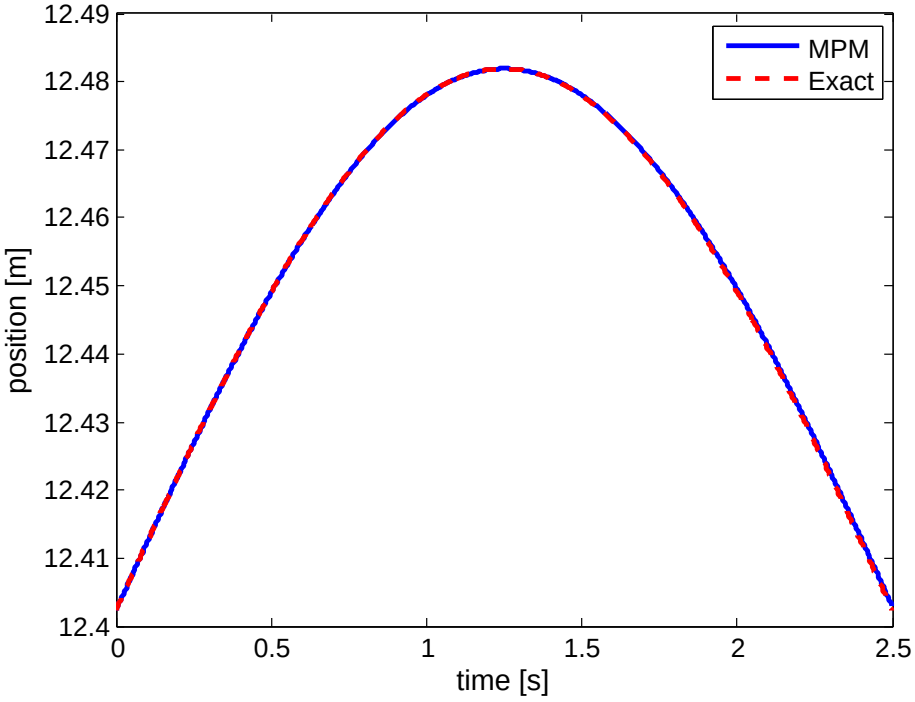

Figure 6.3: Position of the particle situated initially directly left of the middle of the vibrating bar at $x_p = 12.4023$ m with 4 particles per cell and 34 degrees of freedom. Grid crossing does not occur.

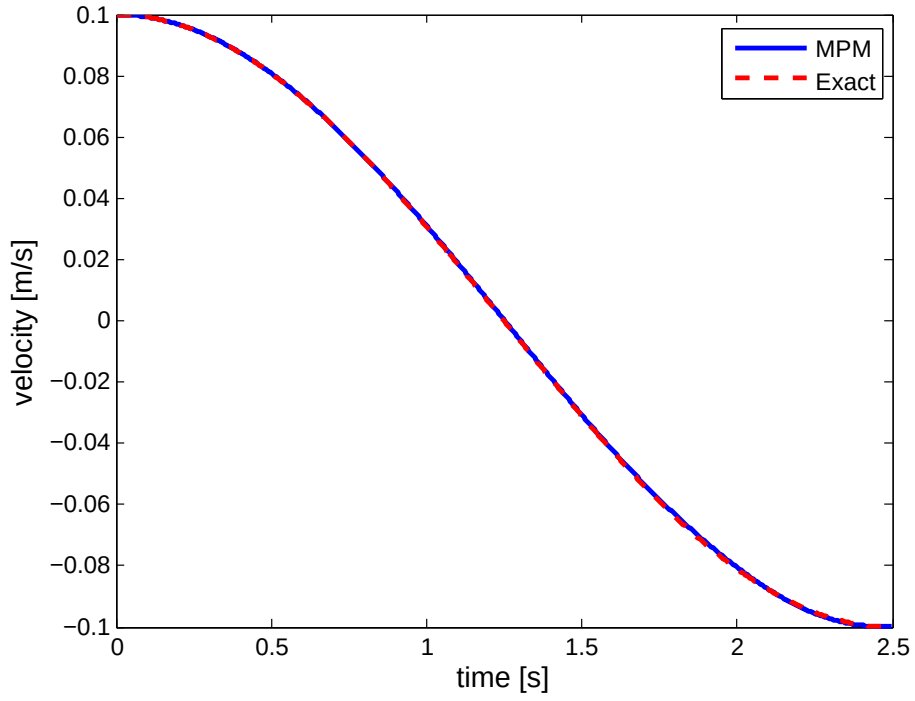

Figure 6.4: Velocity of the particle situated initially directly left of the middle of the vibrating bar at $x_p = 12.4023$ m with 4 particles per cell and 34 degrees of freedom. Grid crossing does not occur.

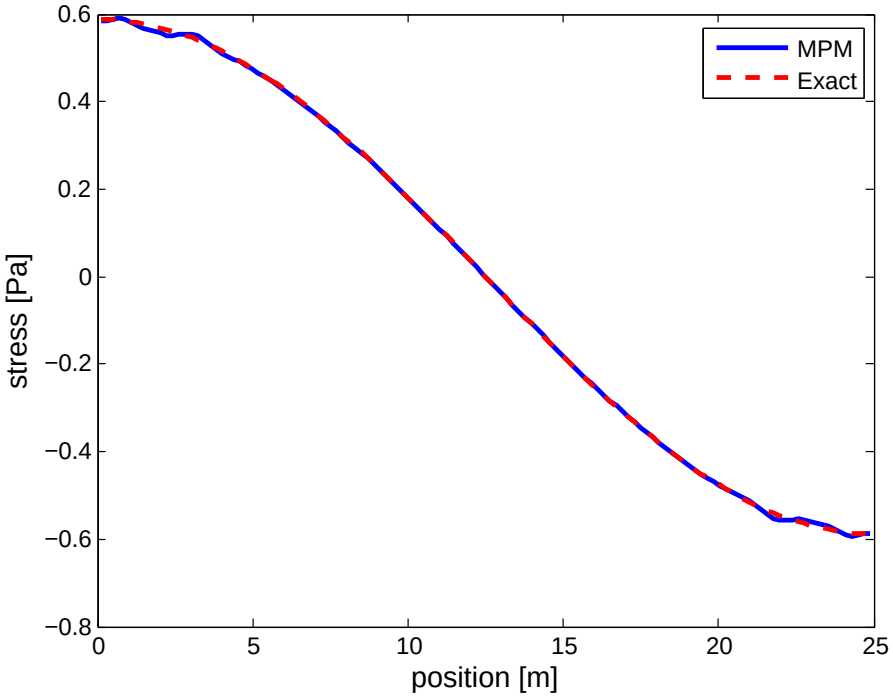

Figure 6.5: Stresses over the bar with quadratic B-spline basis functions at time $t = 0.5$ s with 4 particles per cell and 34 degrees of freedom.

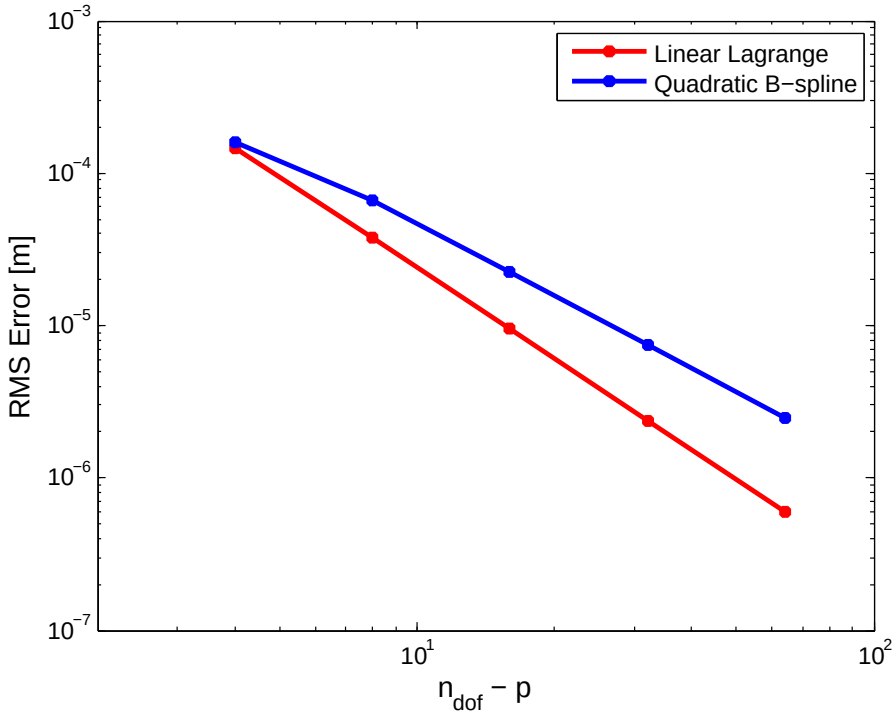

Figure 6.6: Spatial convergence with linear Lagrange and quadratic B-spline basis functions at time $t = 0.02$ s.

6.2.2. VIBRATING BAR - LARGE DEFORMATIONS

In case of large deformations, an ULFEM calculation is used as a reference solution. The obtained solution for position and velocity of a material point is investigated. The parameter values adopted are listed in Table 4.2. A time step size of $\Delta t = 1 \cdot 10^{-5}$ s was used for all simulations.

Figure 6.7 and 6.8 illustrate respectively the position and velocity of the particle situated directly left of the middle of the vibrating bar with 4 particles per cell and 34 degrees of freedom. Since a time step size of $\Delta t = 1 \cdot 10^{-5}$ s is used, this corresponds to a Courant number of $3.2 \cdot 10^{-3}$. The results can be compared when using linear Lagrange basis functions, see Figure 5.8 and 5.9.

Adopting quadratic B-spline basis functions improves the solution in terms of position and velocity. Oscillations which were present with the classical MPM are no longer visible. The solution for displacement and velocity obtained with B-spline MPM correspond well to the reference solution.

Figure 6.9 shows the stresses along the bar at time $t = 0.5$ s. Adopting quadratic basis functions leads to a piecewise linear stress field. Grid crossing does not influence the obtained solution, leading to a significant improvement compared to the use of linear Lagrange basis functions. The oscillations observed in the previous section with quadratic B-spline basis functions are better visible when considering large deformations. Furthermore, they are more spread over the length of the bar.

As in Chapter 5, the internal force at a single degree of freedom is investigated over time. Figure 6.10 shows the internal force of a single degree of freedom. Every time a material point passes the discontinuity of the basis functions associated with this degree of freedom, a red pulse is shown. In contrast when using Lagrange linear basis functions, see Figure 5.11, grid crossing has no effect on the internal force when using quadratic B-spline basis functions.

The results indicate that grid crossing is no longer a problem when adopting quadratic B-spline basis functions. This results in a more accurate reproduction of displacement, velocity and stresses at the material points. However, oscillations at the boundary influence the quality of the MPM solution.

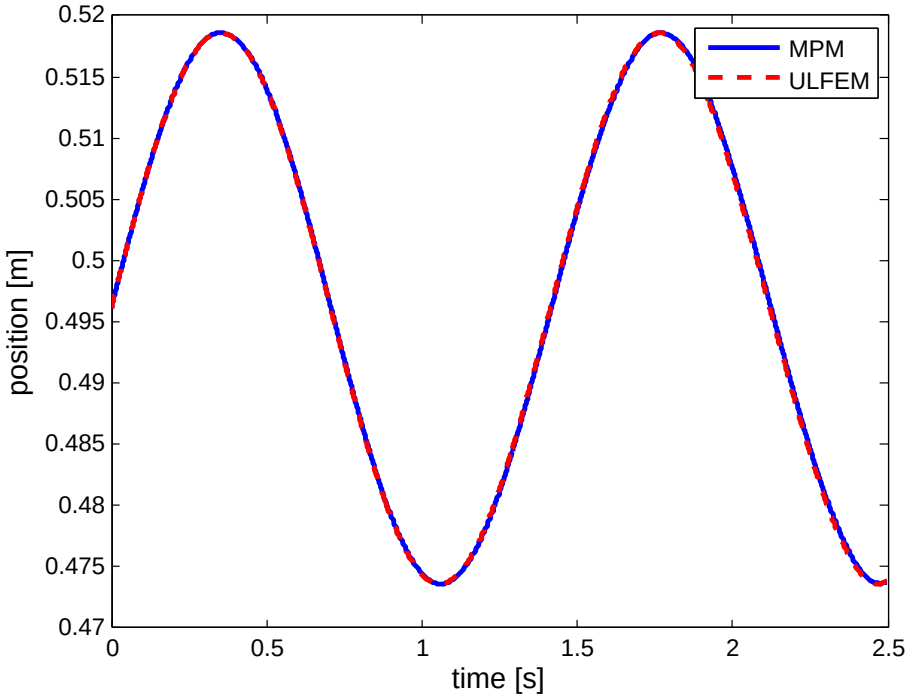

Figure 6.7: Position of the particle initially at $x_p = 0.4961$ m, directly left of the middle of the vibrating bar with 4 particles per cell and 34 degrees of freedom. Grid crossing does occur.

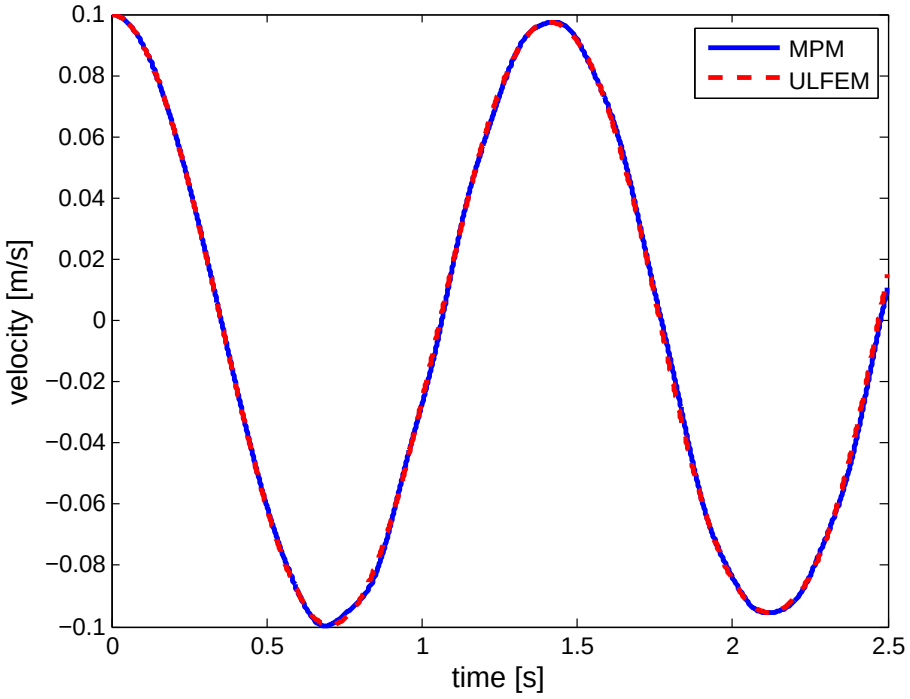

Figure 6.8: Velocity of the particle initially at $x_p = 0.4961$ m, directly left of the middle of the vibrating bar with 4 particles per cell and 34 degrees of freedom. Grid crossing does occur.

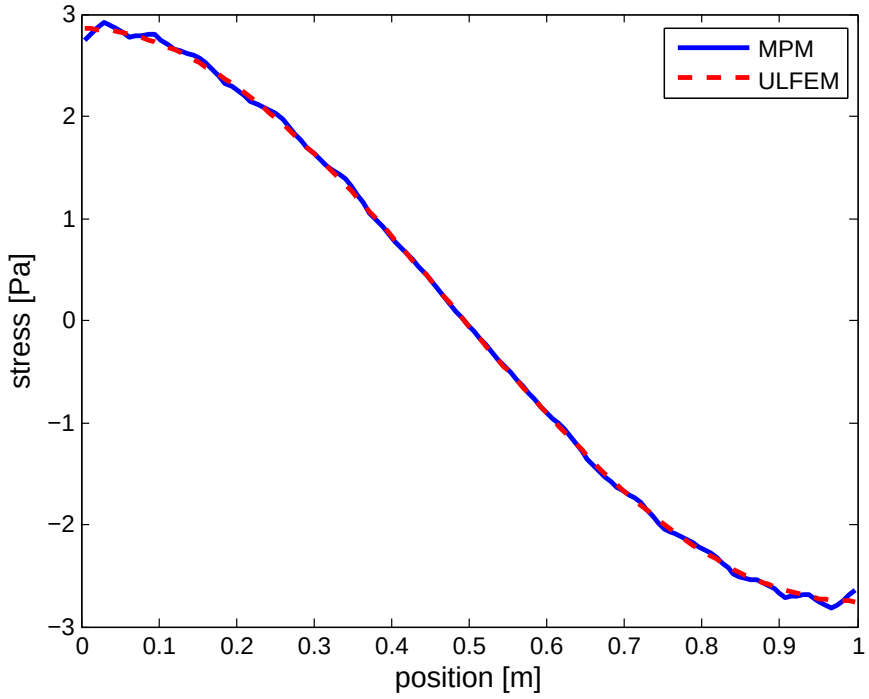

Figure 6.9: Stress over bar with quadratic B-spline basis functions at time $t = 0.5$ s.

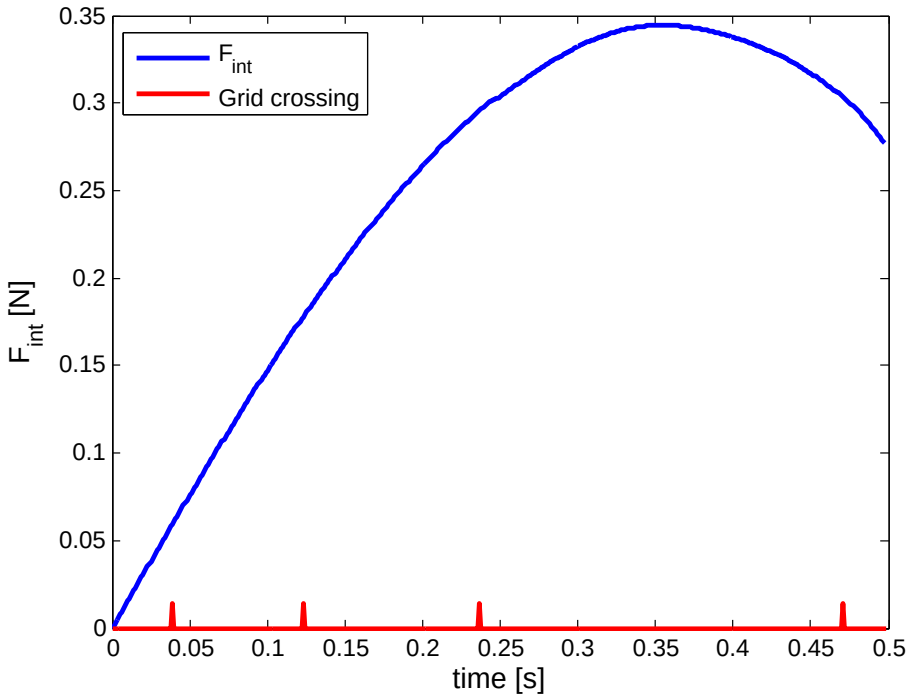

Figure 6.10: Internal force at a single degree of freedom over time. A grid crossing at the discontinuity of the basis functions associated with this degree of freedom is denoted by a red pulse.

6.2.3. COLUMN UNDER SELF-WEIGHT - SMALL DEFORMATIONS

As in Chapter 5, a column suddenly subjected to self-weight is considered. For linear Lagrangian basis functions, grid crossing affected the MPM solution for the position and velocity of a material point when using 80 degrees of freedom. The obtained results were shown in Figure 5.15 and 5.16.

A simulation was carried out with the same parameter values. A time step size was used of $\Delta t = 1 \cdot 10^{-4}$ s which corresponds to a Courant number of $7.07 \cdot 10^{-2}$. Hence, the only difference between the simulations is the type of basis functions that is used. Figure 6.11 and 6.12 denote respectively the displacement and the velocity of the particle initially situated just underneath the center of the column. The obtained position and velocity correspond well to the reference solution. Grid crossing does not effect the quality of the solution anymore. At the time intervals during which velocity at the considered point is constant, the MPM solution oscillates around the reference solution. These oscillations are also present when using the FEM to obtain a numerical solution.

Figure 6.13 shows the stresses over the column with quadratic B-spline basis functions at time $t = 0.5$ s. Results can be compared when using linear Lagrange basis functions, see Figure 5.17. Grid crossing does not affect the quality of the solution, leading to a more accurate representation of the stress field. In contrast when using linear Lagrange basis functions, B-spline MPM is able to reproduce the wave traveling from the bottom to the top of the column. The stress over the column still oscillates around the reference solution when adopting quadratic B-spline basis functions.

Results show that the use of quadratic B-spline basis functions, which are C^1-continuous, solves the numerical problems regarding grid crossing and leads to a more accurate numerical solution for displacement, velocity and stresses.

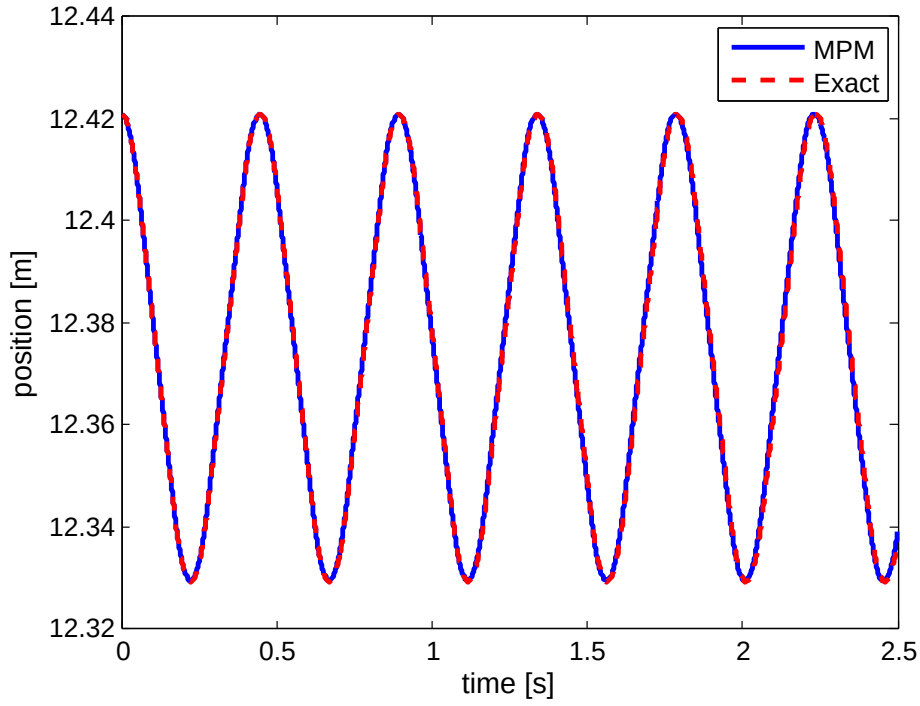

Figure 6.11: Position of the particle situated just underneath the column center with 2 particles per cell and 80 degrees of freedom. Grid crossing does occur.

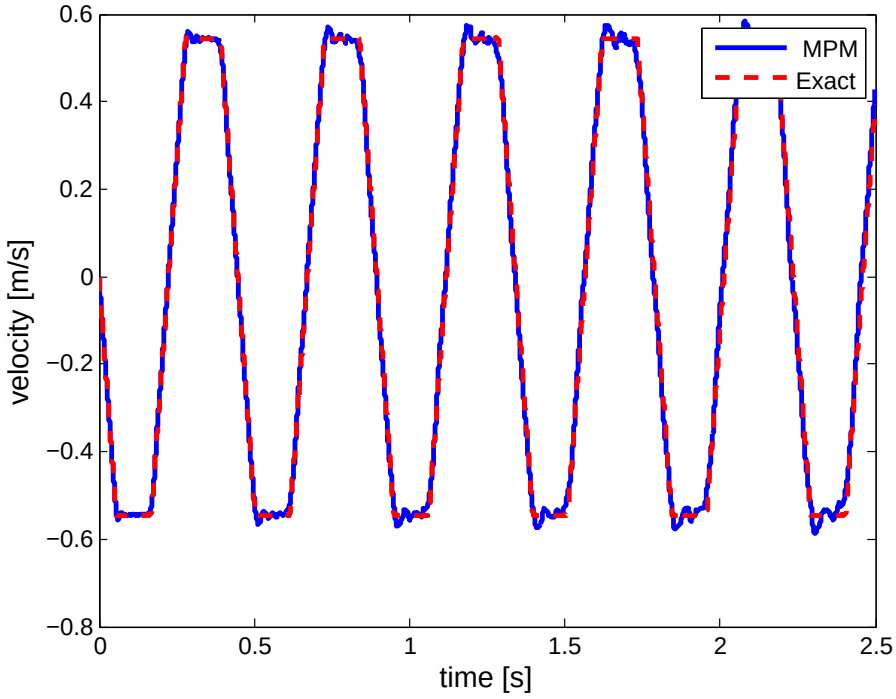

Figure 6.12: Velocity of the particle situated just underneath the column center with 2 particles per cell and 80 degrees of freedom. Grid crossing does occur.

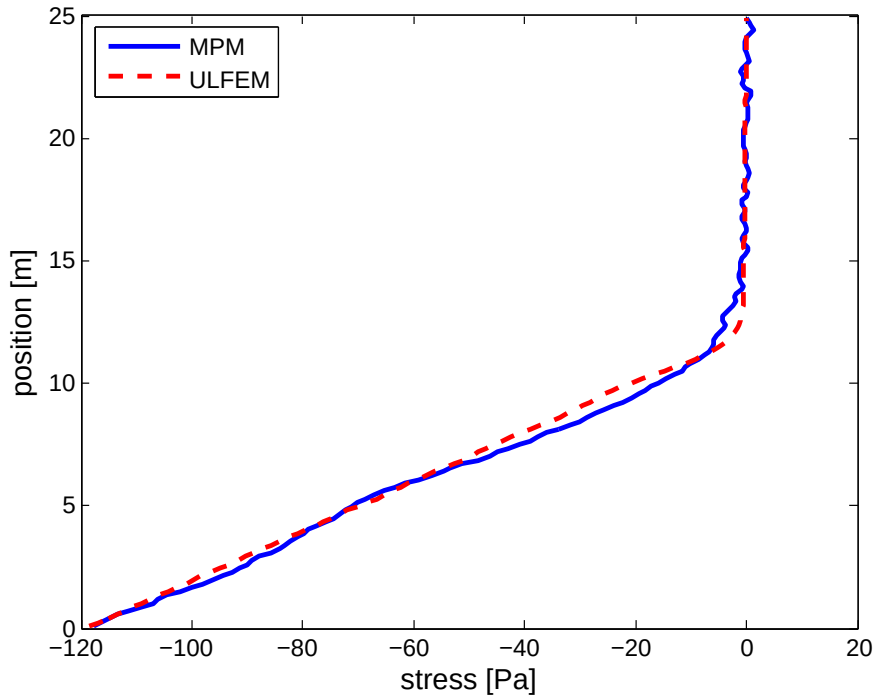

Figure 6.13: Stresses over the column with quadratic B-spline basis functions at time $t = 0.5$ s.

6.2.4. COLUMN UNDER SELF-WEIGHT - LARGE DEFORMATIONS

In case of large deformations, the MPM solution obtained in Chapter 5 for the position and velocity of a single particle were shown in Figure 5.18 and Figure 5.19 respectively. A simulation was carried out using quadratic B-spline basis functions while keeping all the parameter values the same.

The domain is discretized by 64 knot spans which corresponds to 66 degrees of freedom. A time step size is used of $\Delta t = 1 \cdot 10^{-4}$ s which results in a Courant number of $6.5 \cdot 10^{-2}$. Figure 6.14 illustrates the position of a single particle when adopting B-spline basis functions. Compared to Figure 5.18, the obtained results improve significantly. However, the material point does not return to its initial position when time increases, indicating a small dissipation of energy.

These observations can be explained by Figure 6.15 which denotes the velocity of the same particle over time. The velocity oscillates around the reference solution, where the amplitude of the oscillations increases over time leading to a less accurate solution. Compared to Figure 5.19, the obtained solution improves significantly.

Figure 6.16 shows the stresses over the column when using quadratic B-spline basis functions. Compared with the results obtained with linear Lagrange basis functions (Figure 5.20) adopting B-spline basis functions reduces the oscillations significantly, and the wave travelling up can be recognized. The obtained stresses at the material points still oscillate around the reference solution. Compared with the results obtained for small deformations, the amplitude of the oscillations increases.

Results obtained for small deformations indicate that grid crossing should not be a problem anymore when using quadratic B-spline basis functions. Apparently, there is another source of error which influences the quality of the MPM solution. One of these sources might be the quadrature rule used within MPM. Therefore, an alternative numerical integration rule will be adopted in Chapter 7.

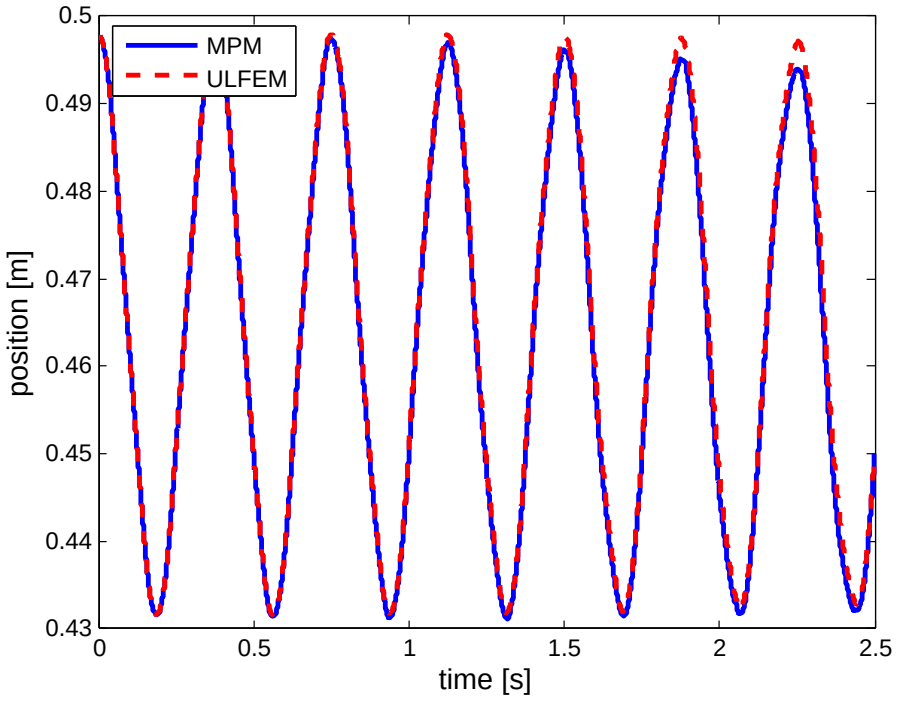

Figure 6.14: Position of the particle situated just underneath the column center with 4 particles per cell and 66 degrees of freedom. Grid crossing does occur.

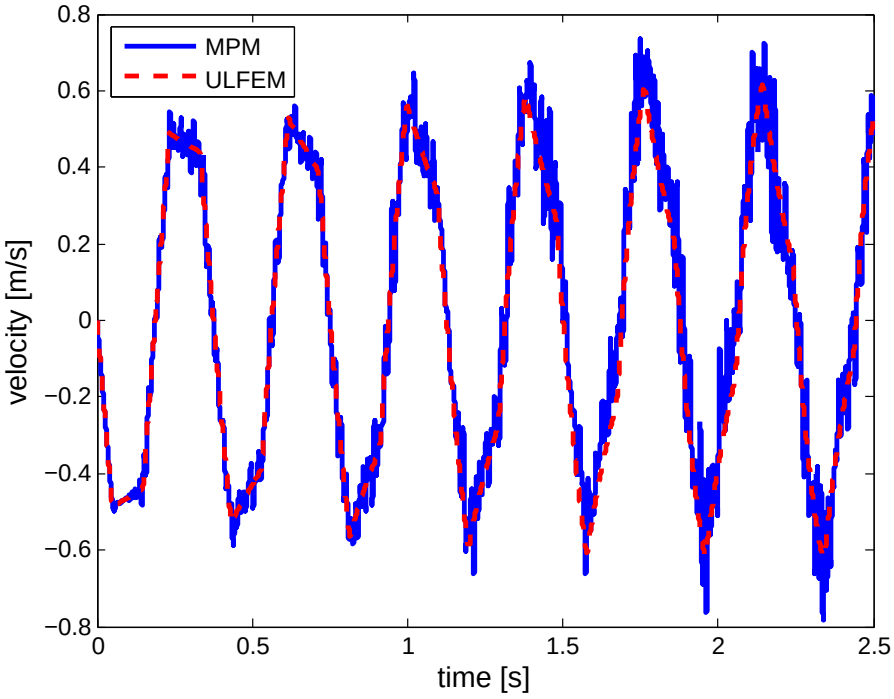

Figure 6.15: Velocity of the particle situated just underneath the column center with 4 particles per cell and 66 degrees of freedom. Grid crossing does occur.

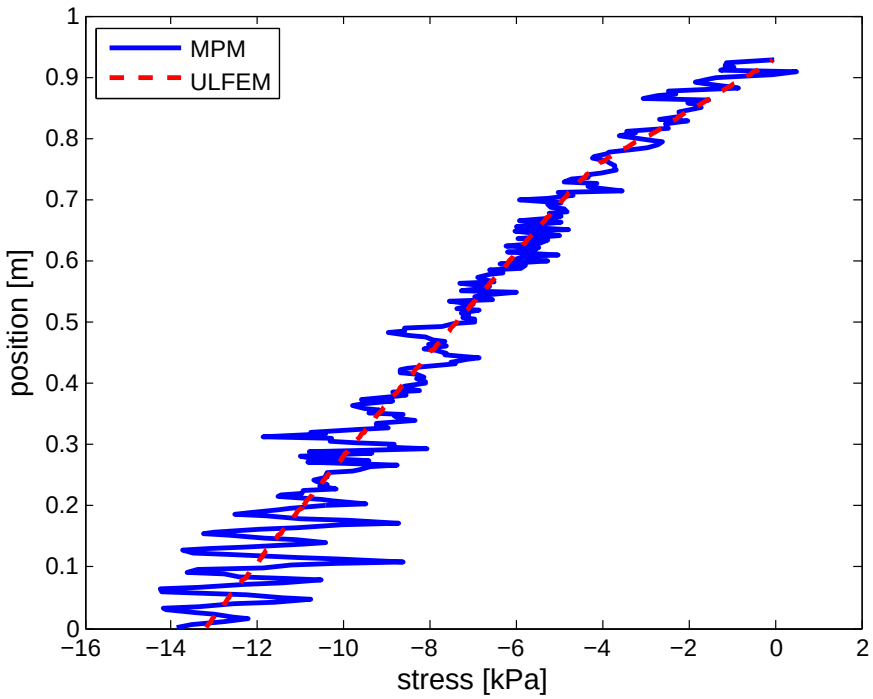

Figure 6.16: Stresses over the column with quadratic B-spline basis functions at time $t = 0.5$ s.

6.3. CONCLUSIONS

In this chapter the use of quadratic B-spline basis functions with the MPM was investigated. Based on the obtained results, the following conclusions can be drawn:

- Adopting quadratic B-spline basis functions does not improve spatial convergence when grid crossing does not occur.
- Quadratic B-spline basis functions solve the problem of grid crossing, which results in a more accurate MPM solution compared to the use of Lagrange basis functions.
- For the first benchmark, the stresses at the material points oscillate at the boundary, influencing the quality of the MPM solution.
- For the second benchmark the stresses and velocity show oscillations, especially when considering large deformations.

The oscillations observed for the different benchmarks might be caused by the numerical quadrature rule used in the MPM. The use of an alternative integration rule to the material point based integration presented in Chapter 3, e.g. Gauss quadrature, is not straightforward. Physical quantities such as stresses and density are only known at the particle positions, which do not correspond with the position of the integration points. Therefore, the value of physical quantities first have to be approximated at the integration points.

In the following chapter, a function reconstruction technique will be used to obtain the value of physical quantities at the integration points such that integrals can be computed more accurately. For linear basis functions, this approach has been used to improve the spatial convergence when particles become arbitrary distributed [2].

7

SPLINE BASED MPM

In Chapter 6, it was shown that the use of quadratic B-spline basis functions reduces the grid crossing error. However, the quality of the solution might be influenced by other sources of error, for example the numerical quadrature used in MPM. Results obtained in the previous chapter seem to indicate this. In this chapter the use of (cubic) spline interpolation within the MPM is investigated to increase the quality of the MPM solution.

The chapter starts with an introduction of (cubic) splines and the application of function reconstruction in the MPM. Results obtained for the two benchmarks of Chapter 4 are presented and compared with results of Chapter 5 and 6.

7.1. SPLINE INTERPOLATION

Consider a function $f : [a,b] \rightarrow \mathbb{R}$ for which only function values at positions $\{a = x_1, \ldots, x_m = b\}$ are known. To obtain the function value at an arbitrary point $\xi \in [a,b]$, the function f has to be reconstructed based on the known function values.

Reconstructing a function based on a set of known function values can be done by interpolating the known values or constructing a function which approximately fits the known values.

Examples of interpolation techniques are linear interpolation, hermite interpolation and spline interpolation [29]. With these approaches, f is reconstructed by interpolating the known function values. As a result the reconstruction $\hat{f}$ of the original function f is obtained such that

$$\hat{f}(x_i) = f(x_i)$$

for all $i \in \{1, \ldots, m\}$.

When constructing a function that approximately fits the known values, the function f can be reconstructed without respecting this property. An example of such a function reconstruction technique is a moving least squares (MLS) approach [30]. This approach was succesfully used in [2] to adapt the numerical integration rule used in the material point method.

Since the properties at the material points represent the MPM solution, interpolation seems the most appropriate type of function reconstruction technique. Polynomial interpolation might lead to oscillations at the boundary, also known as Runge's phenomenon [29]. Therefore, (cubic) spline interpolation is adopted in this thesis as function reconstruction technique.

With (cubic) spline interpolation the function f is approximated by a piecewise third-order polynomial s. On each interval $[x_i, x_{i+1}]$, where $i = 1, \dots m-1$, a third-order polynomial s_i is determined such that:

- $s(x_i) = f(x_i)$ for all $i \in \{1, \dots, m\}$.
- $s_i^{(k)}(x_{i+1}) = s_{i+1}^{(k)}(x_{i+1})$ for all $i \in \{1, m-2\}$ and for $k = 0, 1, 2$.
- $s_0^{(2)}(x_0) = s_{m-1}^{(2)}(x_m) = 0$,

where $s_i^{(k)}$ denotes the k^{th} derivative of the function s_i.

Since s_i is a third-order polynomial, it can be written in the following form:

$$s_i(x) = a_i(x - x_i)^3 + b_i(x - x_i)^2 + c_i(x - x_i) + d_i.$$

To determine the coefficients of s_i, the properties of s_i listed above are used. In [29] this procedure is decribed in more detail.

To illustrate cubic spline interpolation, a known function was reconstructed based on a finite number of function values. Figure 7.1 denotes the function $f(x) = \sin(x)$ and an interpolating cubic spline $s(x)$. The red dotted function values were used to determine the third-order polynomials s_i.

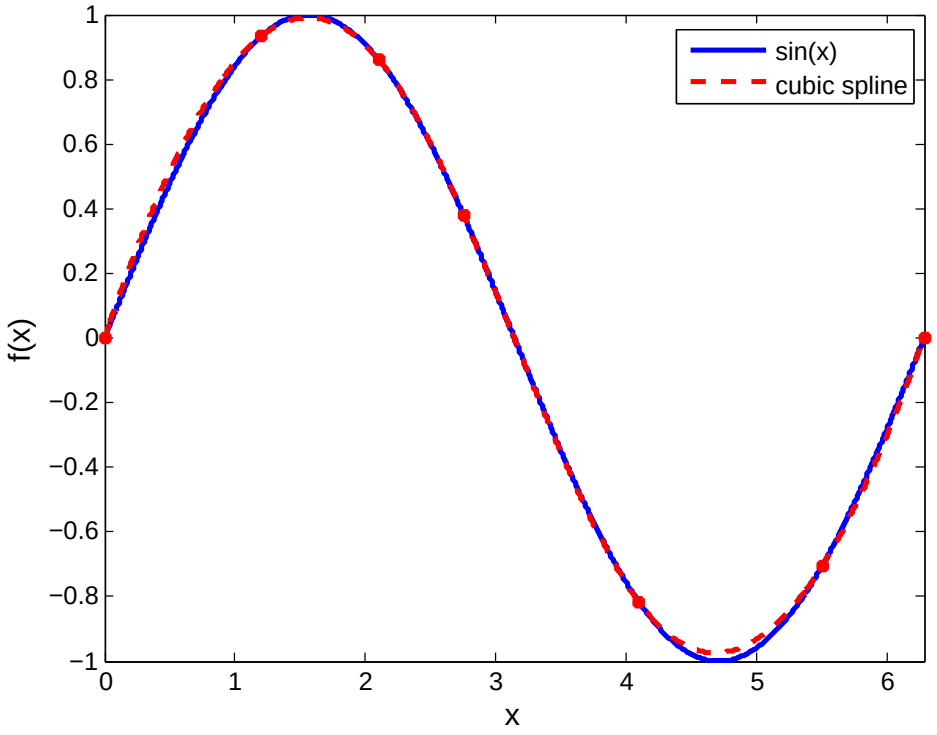

Figure 7.1: Cubic spline interpolation based on sample values of $\sin(x)$.

7.2. SPLINE BASED MPM

In the following, the alternative numerical integration rule based on a (cubic) spline function is discussed. Spline functions are constructed by using the known values of the stresses and velocities at particle positions. These spline functions are then evaluated at the position of integration points to adapt the numerical quadrature rule.

The numerical quadrature rule used in MPM implies that mass is conserved when projecting the mass from the particles to the degrees of freedom. This can be shown from the definition of the mass matrix by changing the order of summation and using the partition of unity property of the basis functions:

$$\begin{aligned}\sum_{i=1}^{n} \mathbf{M^L}_{(i,i)} &= \sum_{i=1}^{n}\sum_{p=1}^{n_p} m_p \phi_i(x_p) \\ &= \sum_{p=1}^{n_p}\sum_{i=1}^{n} m_p \phi_i(x_p) \\ &= \sum_{p=1}^{n_p} m_p.\end{aligned}$$

The use of an alternative integration rule might lead to a projection on the degrees of freedom which is not mass conserving. Therefore, the mass matrix and gravitational force vector are still determined with the quadrature rule used in MPM.

The numerical quadrature rule used in MPM also implies conservation of momentum. This can be shown in a similar way:

$$\begin{aligned}\sum_{i=1}^{n} \mathbf{M^L}_{(i,i)} v_i &= \sum_{i=1}^{n} \mathbf{M^L}_{(i,i)} \sum_{p=1}^{n_p} \frac{m_p \phi_i(x_p) v_p}{\mathbf{M^L}_{(i,i)}} \\ &= \sum_{p=1}^{n_p}\sum_{i=1}^{n} m_p \phi_i(x_p) v_p \\ &= \sum_{p=1}^{n_p} m_p v_p.\end{aligned}$$

An alternative quadrature rule might not lead to a momentum conserving mapping. Whether or not this influences the quality of the results is investigated for the benchmarks.

The (cubic) spline **stress field** $\hat{\sigma}(x)$ is determined based on the stresses at the particle positions. The internal force vector is then determined in the following way:

$$\mathbf{F}^{\text{int},t}_{(i)} = \int_{\Omega_t} \nabla\phi_i(x)\sigma(x)\mathrm{d}x \approx \sum_{c=1}^{n_c} \omega_c \nabla\phi_i(x_c)\hat{\sigma}(x_c),$$

Here ω_c and x_c denote respectively the weight and position of the integration points and n_c the number of integration points. In case the momentum conserving projection used in MPM is adapted, the **projection of the particle velocities** is performed as follows:

$$\int_{\Omega_t} \rho(x) v(x) \phi_i(x)\mathrm{d}x \approx \sum_{c=1}^{n_c} \omega_c \hat{\rho}(x_c)\hat{v}(x_c)\phi_i(x_c),$$

where $\hat{v}(x)$ and $\hat{\rho}(x)$ denote the cubic spline based on the particle velocities and densities. Note that the (cubic) splines are not integrated, but are only used to obtain (approximated) function values at the integration points.

Since the basis functions are piecewise quadratic functions, a 2-point Gauss rule is used on the half of each non-zero interval $[\xi_i, \xi_{i+1}]$ to approximate the integrals. Hence the following integration rule is applied:

$$\int_{\Omega_t} f(x)\mathrm{d}x = \sum_{j=p+1}^{n} \int_{\xi_j}^{\xi_{j+1}} f(x)\mathrm{d}x = \sum_{j=p+1}^{n} \sum_{c=1}^{4} \omega_c f(x_c),$$

where the integration weights are given by

$$\omega_c = \frac{\xi_{j+1} - \xi_j}{4}$$

for all Gauss points in the interval $[\xi_i, \xi_{i+1}]$. The position of the Gauss points are given by

$$\begin{aligned}
x_1 &= -\frac{\xi_{j+1}-\xi_j}{4}\sqrt{\frac{1}{3}} + \frac{3\xi_j + \xi_{j+1}}{4}, \\
x_2 &= \frac{\xi_{j+1}-\xi_j}{4}\sqrt{\frac{1}{3}} + \frac{3\xi_j + \xi_{j+1}}{4}, \\
x_3 &= -\frac{\xi_{j+1}-\xi_j}{4}\sqrt{\frac{1}{3}} + \frac{\xi_j + 3\xi_{j+1}}{4}, \\
x_4 &= \frac{\xi_{j+1}-\xi_j}{4}\sqrt{\frac{1}{3}} + \frac{\xi_j + 3\xi_{j+1}}{4}.
\end{aligned}$$

More information about Gaussian quadrature and in particular the two point Gauss rule can be found in Appendix A.3. Figure 7.2 denotes exemplarily the positions of Gauss points in case of a discretization featuring 5 degrees of freedom and quadratic B-spline basis functions.

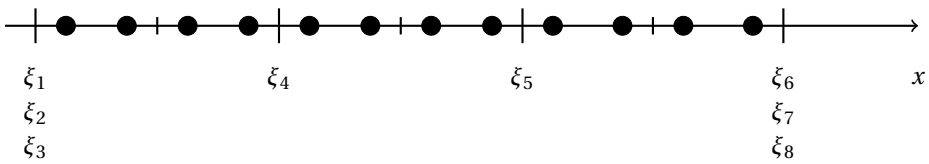

Figure 7.2: Position of the integration points in case of 5 degrees of freedom and quadratic B-spline basis functions.

The deforming continuum must be taken into account when applying a numerical quadrature rule. In the original MPM, this is done by using the particles as integration points and the volume of the particles as integration weights. Therefore, the spline is only reconstructed on the interval supported by the continuum. An approximation of this interval is given by

$$\Omega_t \approx [x_1^t - \frac{1}{2}V_1^t, x_{n_p}^t + \frac{1}{2}V_{n_p}^t],$$

where x_p^t and V_p^t denote respectively the position and volume of a particle at time t. Integration points which do not lie inside this interval, obtain the value 0 for all physical properties. These Gauss points thus do not contribute to the approximation of the integrals. This is illustrated in Figure 7.3. The Gauss points outside the support of the continuum, denoted with red, are deactivated by setting al the physical properties equal to 0.

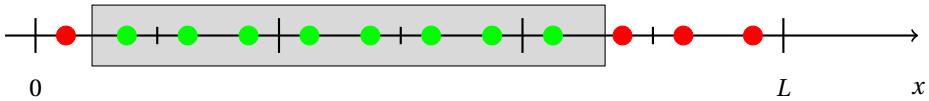

Figure 7.3: Illustration of integration domain.

This approach renders problems in case only one of the two Gauss points corresponding to an interval $[\xi_i, \xi_{i+1}]$ lies outside the interval $[x_1 - \frac{1}{2}V_1^t, x_{n_p} + \frac{1}{2}V_{n_p}^t]$. Since the value at one Gauss point is set equal to 0, the quality of the approximation drops. To solve this problem, the position of the Gauss points is redefined in case this might happen. Figure 7.4 illustrates this procedure. The red dotted Gauss point lies outside the support of the continuum whereas the corresponding Gaus point lies inside the support. The position of both integration points is redefined.

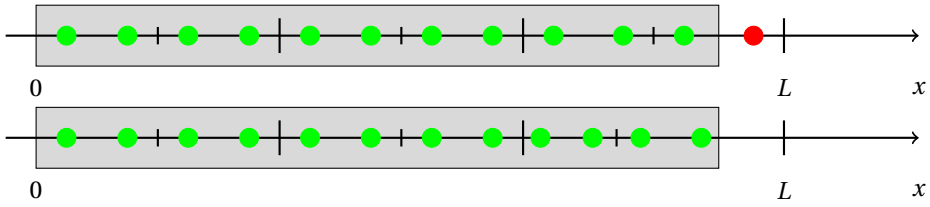

Figure 7.4: Redefining position of the Gauss points based on the position of the continuum.

The integrals are not exactly integrated due to three reasons:

- A 2-point Gauss rule is only an exact integration rule for a polynomial up to order 3, not for an arbitrary function f. For example, the function $f(x) = \rho(x)\phi_i(x)$ which is integrated to obtain the entry (i,i) of the mass matrix is not integrated in an exact way.
- The function values at integration points computed from splines are approximations of the true function values.
- The interval $[x_1 - \frac{1}{2}V_1^t, x_{n_p} + \frac{1}{2}V_{n_p}^t]$ approximates the support of the continuum.

Whether or not these errors dominate the benefit from adopting another integration rule the will be investigated with the benchmarks.

RICHARDSON ITERATION

As described in Chapter 3 the velocities at the degrees of freedom are computed by a density weighted projection. A lumped mass matrix is used resulting in

$$v_i^{t+\Delta t} = \frac{\int_{\Omega_t} \rho(x)\phi_i(x)\, v(x)^{t+\Delta t}\mathrm{d}x}{\mathbf{M^L}_{(i,i)}}.$$

The use of a lumped mass matrix leads to an error, which might influence the spatial convergence when using quadratic B-spline basis functions. Whether or not the use of a consistent mass matrix improves the results for the benchmarks is investigated in the next section.

Since the consistent mass matrix is symmetric and positive-definite, Cholesky factorization can be used to solve the linear system of equations. For large values of n this direct solver may be too expensive [31]. Therefore, the iterative Richardson method has been adopted. As described in [32], $\mathbf{v}^{(n+1)}$ is obtained from $\mathbf{v}^{(n)}$ from the following recursion formula:

$$\mathbf{M^L}\,\mathbf{v}^{(n+1)} = \mathbf{P} + \left(\mathbf{M^L} - \mathbf{M^C}\right)\mathbf{v}^{(n)},$$

where $\mathbf{v}^{(0)}$ is obtained by solving

$$\mathbf{M^L}\,\mathbf{v}^{(0)} = \mathbf{P}.$$

As a stopping criterion we use

$$\frac{||\mathbf{P} - \mathbf{M^C}\,\mathbf{v}^*||_2}{||\mathbf{P}||_2} \leq \epsilon,$$

with $\epsilon = 1 \cdot 10^{-9}$. Observations show that using this value as a stopping criterion for Richardson iteration renders the same results as the use of a direct solver. An iterative solver is faster than Cholesky factorization for large values of n, but computationally more expensive compared with the use of a lumped mass matrix.

7.2.1. VIBRATING BAR - SMALL DEFORMATIONS

In the following, the vibrating bar is considered with the parameter values listed in Table 4.1. Results obtained for both position and velocity of a material point are presented. A time step size was used of $\Delta t = 1 \cdot 10^{-5}$ s for all simulations presented in this section.

The approach presented in Chapter 6 is used, extended by the alternative numerical integration as discussed in the previous section. The alternative quadrature rule was used to obtain the internal force and velocity at the degrees of freedom. Hence, a projection is used which is not momentum conserving. A consistent mass matrix is used to project particle velocities on the degrees of freedom.

Figure 7.5 and 7.6 show respectively the change of position and velocity of the particle situated directly left of the middle of the bar with 4 particles per cell and 34 degrees of freedom. Since a time step size of $\Delta t = 1 \cdot 10^{-5}$ s is used, this corresponds to a Courant number of $1.28 \cdot 10^{-4}$. Visually, there is hardly any difference with the results obtained in Chapter 5 and 6. The spline based MPM seems to render equally good for this benchmark.

The stresses over the bar at time $t = 0.5$ s are shown in Figure 7.7. The solution obtained with spline based MPM is almost identical to the exact solution. The oscillations present at the boundary when adopting B-spline MPM are no hardly visuable.

Figure 7.8 shows the spatial convergence for the spline based MPM. The RMS error is determined at time $t = 0.02$ s and the number of degrees of freedom was varied between 6 and 66. Compared with results obtained in Chapter 5 and 6, spatial convergence significantly improved. No grid crossing occured during these simulations.

Table 7.1 shows the RMS error for different number of degrees of freedom and particles per cell. Increasing the number of degrees of freedom decreases the RMS error. For the same number of degrees of freedom, increasing the number of particles per cell decreases the RMS error.

$n_{dof} - p$	e^{RMS} - 4 PPC	e^{RMS} - 6 PPC	e^{RMS} - 8 PPC
4	$4.9665 \cdot 10^{-6}$	$4.8784 \cdot 10^{-6}$	$4.8629 \cdot 10^{-6}$
8	$5.4447 \cdot 10^{-7}$	$5.3234 \cdot 10^{-7}$	$5.3018 \cdot 10^{-7}$
16	$6.4964 \cdot 10^{-8}$	$6.3387 \cdot 10^{-8}$	$6.3106 \cdot 10^{-8}$
32	$7.9865 \cdot 10^{-9}$	$7.7862 \cdot 10^{-9}$	$7.7505 \cdot 10^{-9}$
64	$1.0137 \cdot 10^{-9}$	$9.8887 \cdot 10^{-10}$	$9.8455 \cdot 10^{-10}$

Table 7.1: RMS-errors with different degrees of freedom and particles per cell.

Table 7.2 shows the spatial convergence in case 4 particles per cell are defined initially. The spline based MPM shows third order convergence for the vibrating bar problem.

$n_{dof} - p$	$\log_2\left(\frac{e^{\text{RMS}}(h)}{e^{\text{RMS}}(h/2)}\right)$
4	
8	3.1893
16	3.0671
32	3.0240
64	2.9780

Table 7.2: Accuracy of the numerical solution at time $t = 0.02$ s with 4 particles per cell.

The results for this benchmark show the improvement when using an alternative quadrature rule within the MPM. Spatial convergence improved and stresses can be more accurately reproduced compared to the use of B-spline MPM.

Results presented in this section were obtained with the use of a consistent mass matrix and an alternative quadrature rule to project the particle velocities on the degrees of freedom. Numerical experiments show that these adaptions are both necessary conditions to obtain third order spatial convergence and a stress field without oscillations at the boundary.

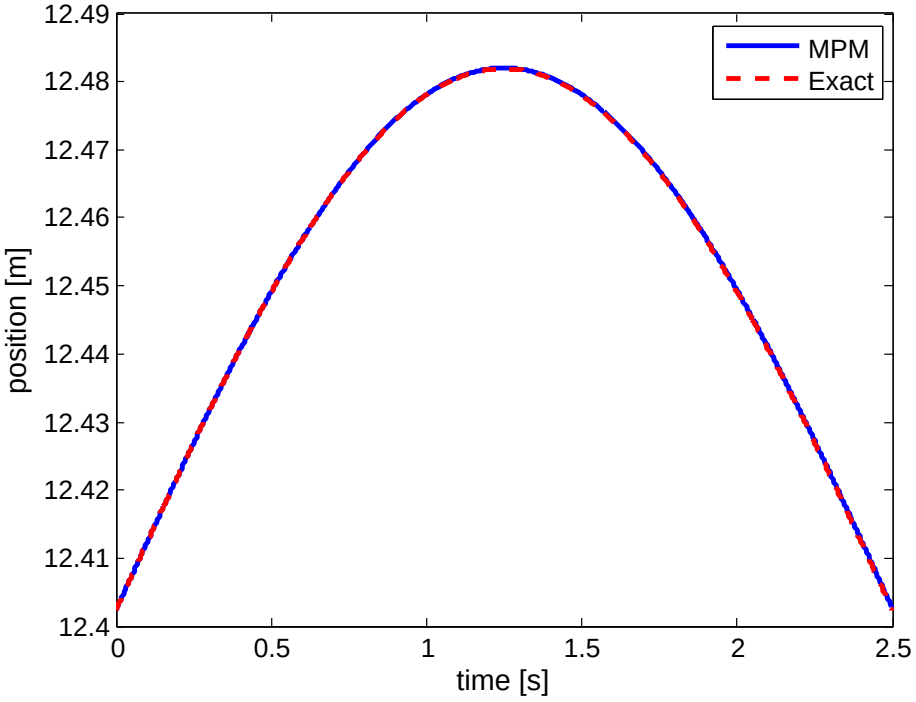

Figure 7.5: Position of the particle situated initially at $x_p = 12.4023$ m, directly left of the middle of the vibrating bar with 4 particles per cell and 34 degrees of freedom. Grid crossing does not occur.

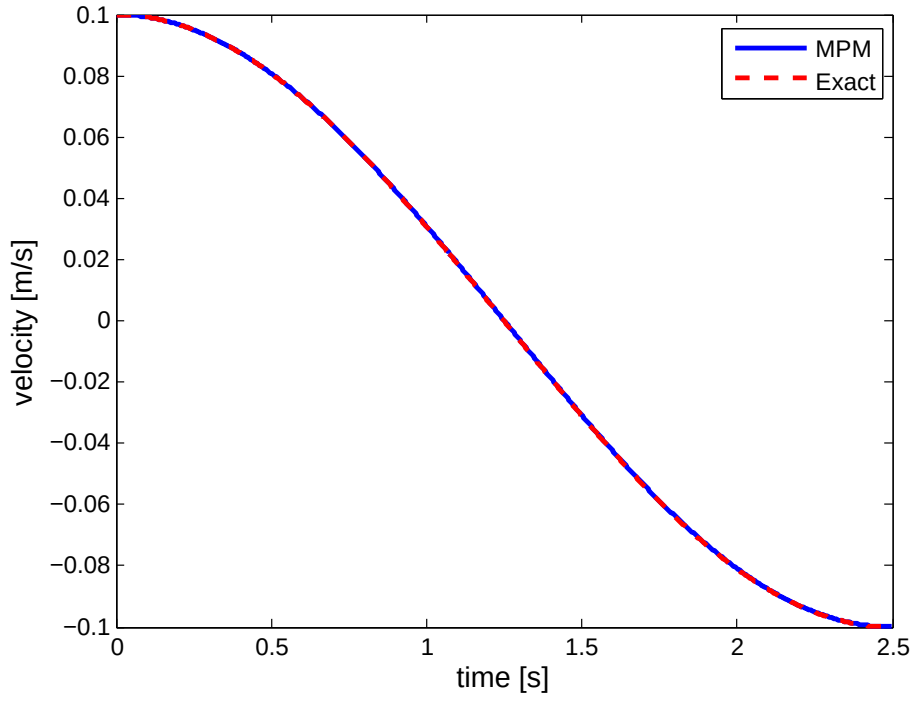

Figure 7.6: Velocity of the particle situated intially at $x_p = 12.4023$ m, directly left of the middle of the vibrating bar with 4 particles per cell and 34 degrees of freedom. Grid crossing does not occur.

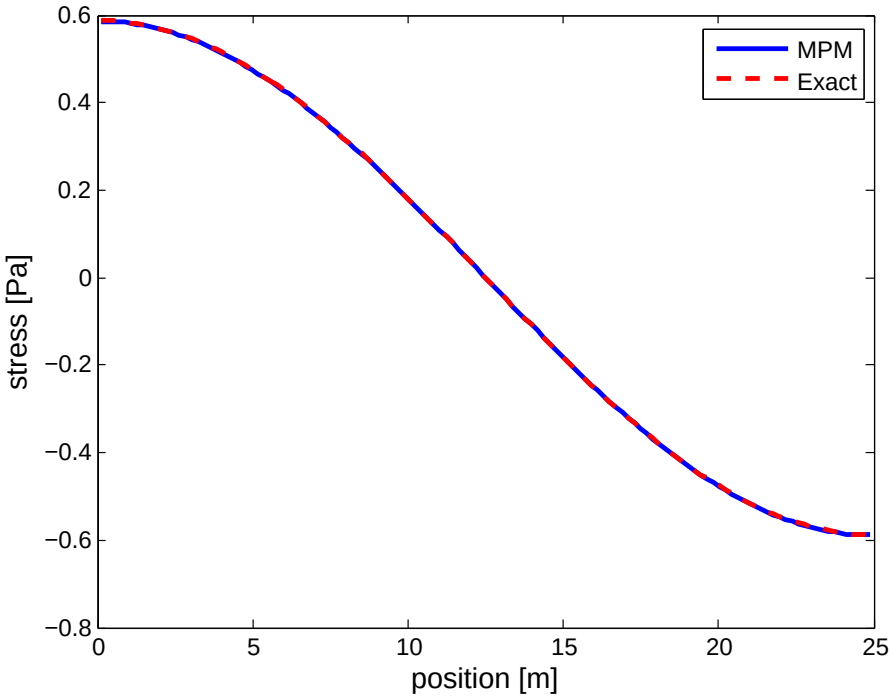

Figure 7.7: Stresses over the bar with spline based MPM at time $t = 0.5$ s with 4 particles per cell and 34 degrees of freedom.

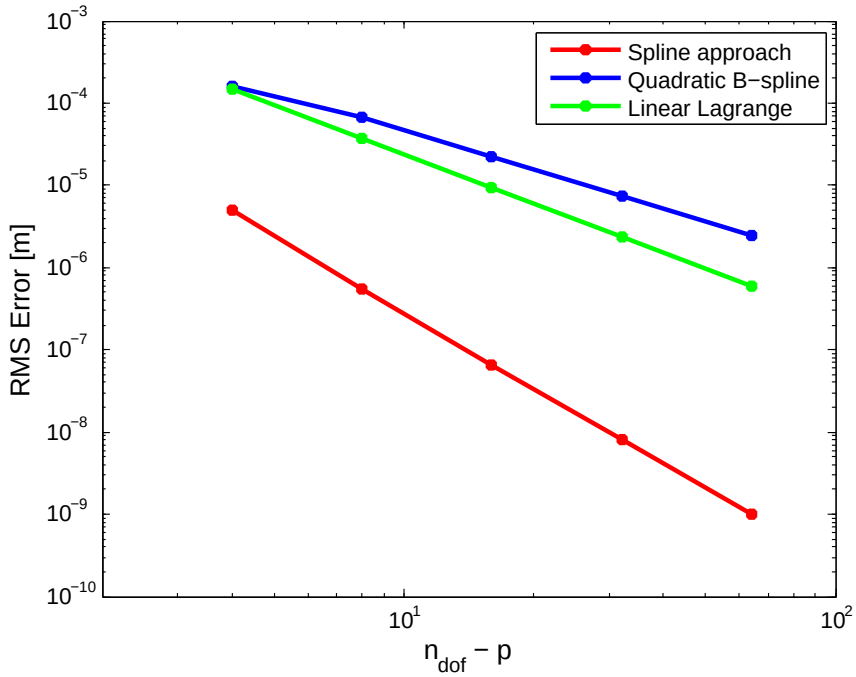

Figure 7.8: Spatial convergence at time $t = 0.02$ s of three versions of MPM with 4 PPC for the vibrating bar problem when considering small deformations. Grid crossing is not observed.

7.2.2. VIBRATING BAR - LARGE DEFORMATIONS

In case of large deformations, the parameter values listed in Table 4.2 are adopted. A time step size of $\Delta t = 1 \cdot 10^{-5}$ s was used for all simulations.

The same version of MPM is used as in the previous section. This implies that an alternative quadrature rule is used to obtain the internal force and velocity at the degrees of freedom. A consistent mass matrix is used to project particle velocities on the degrees of freedom.

Figure 7.9 and 7.10 illustrate respectively the position and velocity of the particle situated directly left of the middle of the vibrating bar with 4 particles per cell and 34 degrees of freedom. Since a time step size of $\Delta t = 1 \cdot 10^{-5}$ s is used, this corresponds to a Courant number of $3.2 \cdot 10^{-3}$. There is no visible difference with the results obtained in Chapter 6, see Figure 6.7 and 6.8. Hence, grid crossing does not affect the numerical solution as in Chapter 5 when using linear Lagrange basis functions.

The stresses over the bar at time $t = 0.5$ s are shown in Figure 7.11. Results can be compared with respectively linear Lagrange and B-spline MPM, see Figure 5.10 and 6.9. The solution obtained with spline based MPM hardly oscillates and is almost identical to the ULFEM solution.

Hence, the use of an alternative quadrature rule within MPM leads to a better representation of the stress field for this benchmark. There are no visible differences in the obtained displacement and velocity when adopting an alternative quadrature rule.

As with small deformations, the use of a consistent mass matrix and an alternative quadrature rule in the particle velocity projection are necessary conditions to obtained a stress field without oscillations at the boundary.

Figure 7.12 shows the internal force at a single degree of freedom over time. As with B-spline MPM grid crossing has no influence on the obtained internal force at the considered degree of freedom.

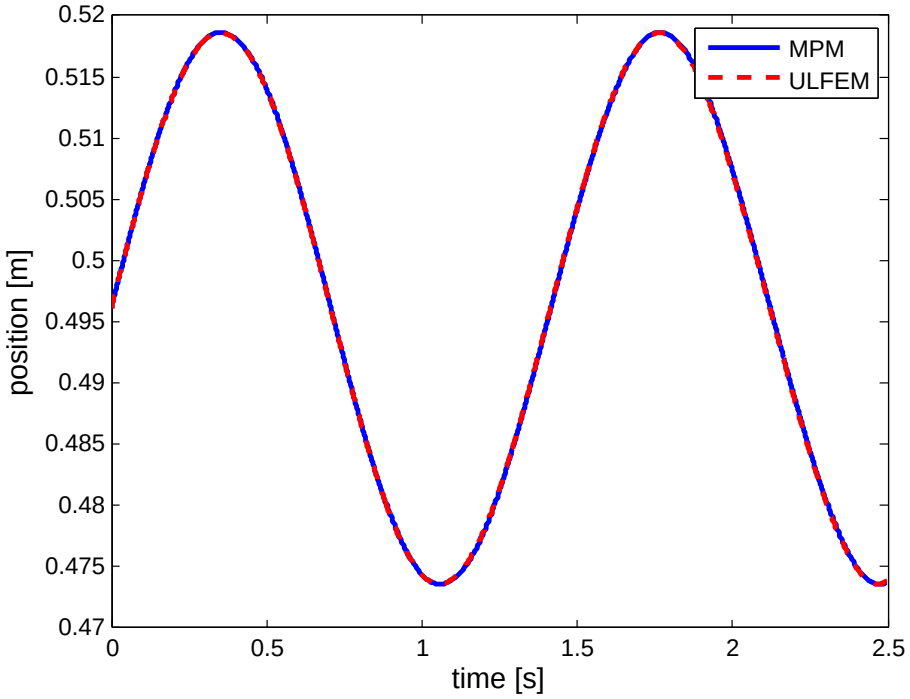

Figure 7.9: Position of the particle initially at $x_p = 0.4961$ m, directly left of the middle of the vibrating bar with 4 particles per cell and 34 degrees of freedom. Grid crossing does occur.

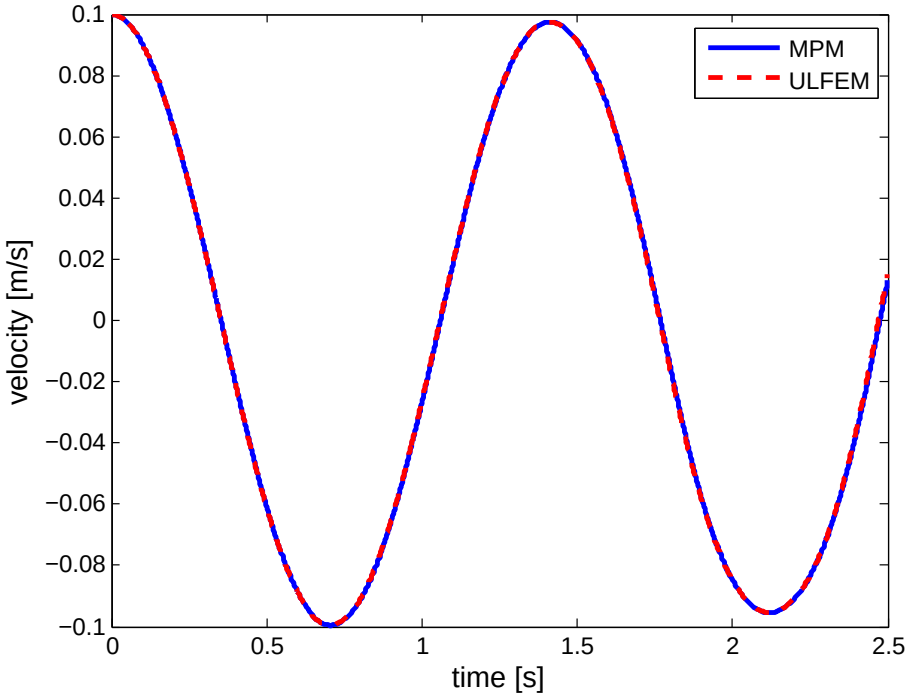

Figure 7.10: Velocity of the particle initially at $x_p = 0.4961$ m, directly left of the middle of the vibrating bar with 4 particles per cell and 34 degrees of freedom. Grid crossing does occur.

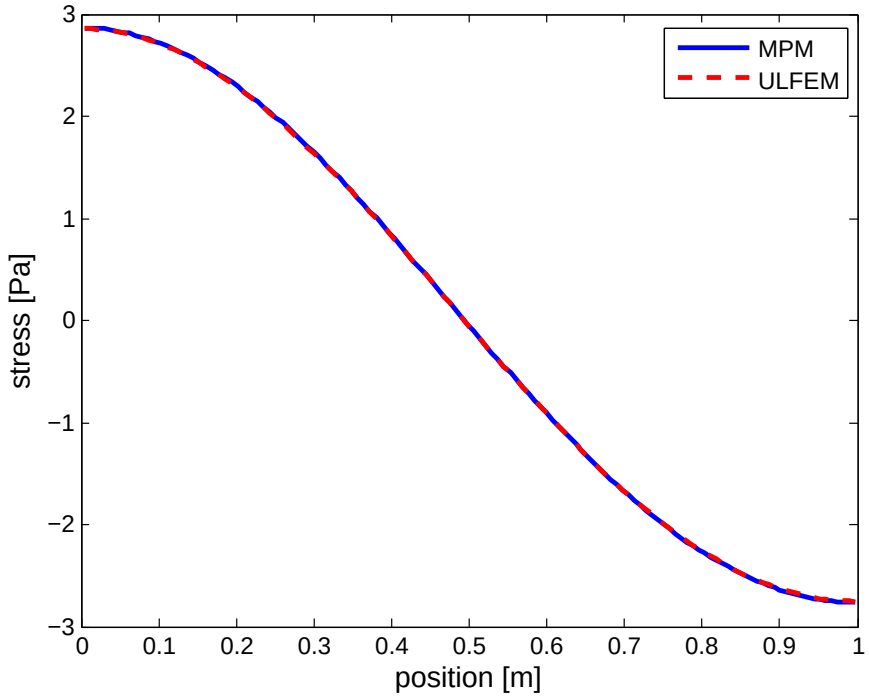

Figure 7.11: Stresses over the bar obtained with spline based MPM at time $t = 0.5$ s.

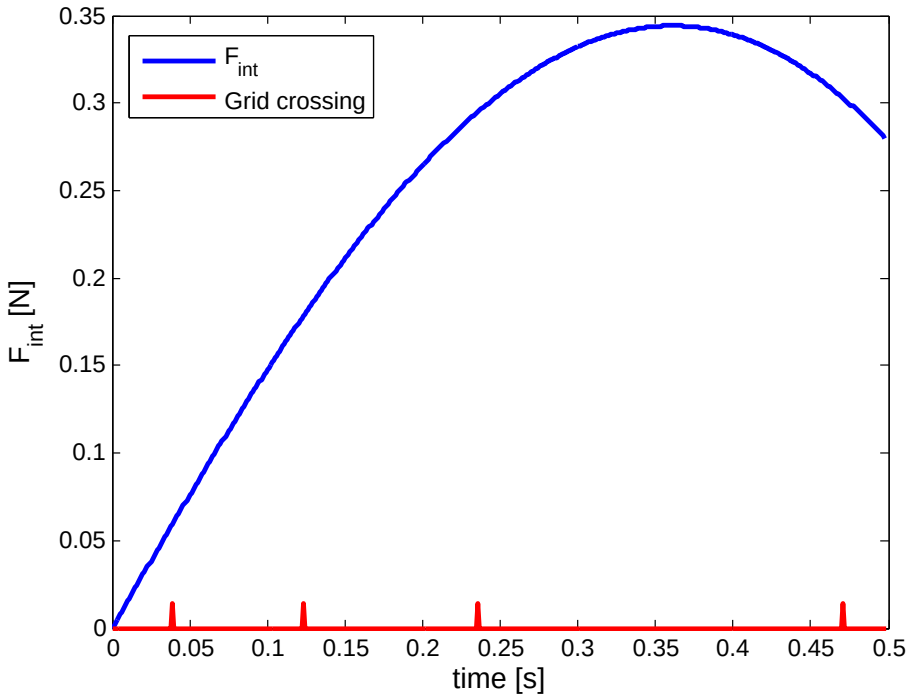

Figure 7.12: Internal force at a single degree of freedom over time. A grid crossing at the discontinuity of the basis functions associated with this degree of freedom is denoted by a red pulse.

7.2.3. COLUMN UNDER SELF-WEIGHT - SMALL DEFORMATIONS

To investigate the performance of the spline based MPM further, the second benchmark is revisited when considering small deformations. The same parameter values are used as in the previous chapters and are listed in Table 4.3. A time step size was used of $\Delta t = 1 \cdot 10^{-4}$ s for all simulations for which results are presented in this section.

In contrast with the previous benchmark, the momentum conserving mapping used in the original MPM is adopted since the alternative mapping lead to oscillations in particle velocity as time increased. Hence, only the internal force at the degrees of freedom is approximated with an alternative quadrature rule.

Figure 7.13 and 7.14 show respectively the computed position and velocity of a material point situated underneath the column center with 2 PPC and 81 degrees of freedom. Since a time step size of $\Delta t = 1 \cdot 10^{-4}$ s is used, this corresponds to a Courant number of $7.07 \cdot 10^{-2}$.

Compared with the results obtained without the adapted numerical quadrature rule, there is visually no difference through enhancement of the integration rule, see Figure 6.11 and 6.12.

Figure 7.15 shows the stresses over the column at time $t = 0.5$ s obtained with spline based MPM. Visually, there is only a small difference with the results obtained in Chapter 6, see Figure 6.13. The stress oscillates less at the upper part of the column with spline based MPM, although the difference is small. Spline based MPM is able to reproduce the wave traveling from the bottom to the top of the column, but the obtained solution still oscillates around the reference solution.

Both B-spline MPM and spline based MPM seem to render equally well for this benchmark when small deformations are considered.

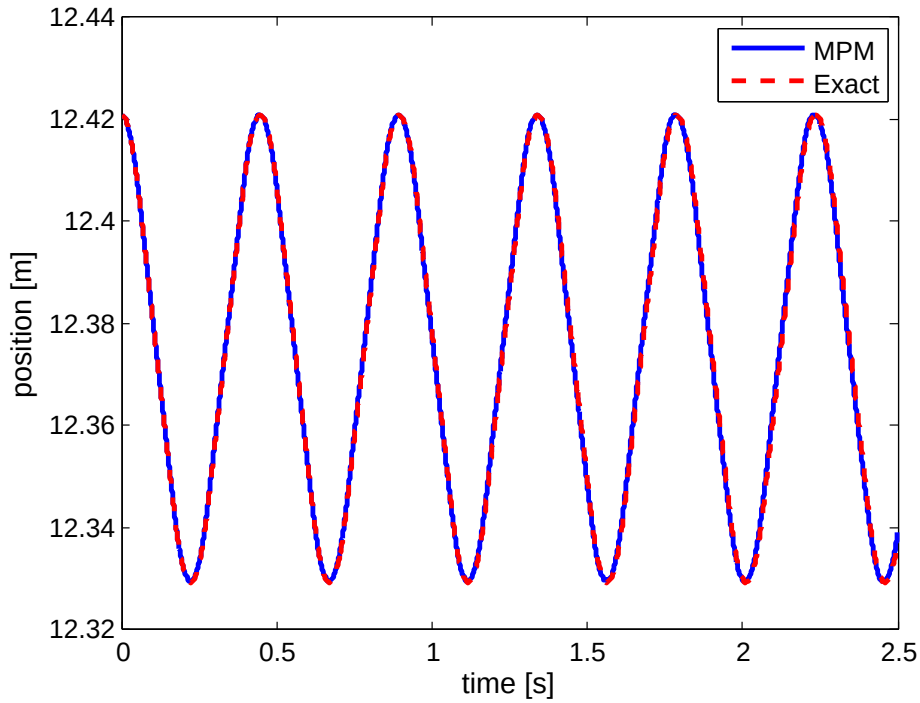

Figure 7.13: Position of the particle situated just underneath the column center with 2 particles per cell and 80 degrees of freedom. Grid crossing does occur.

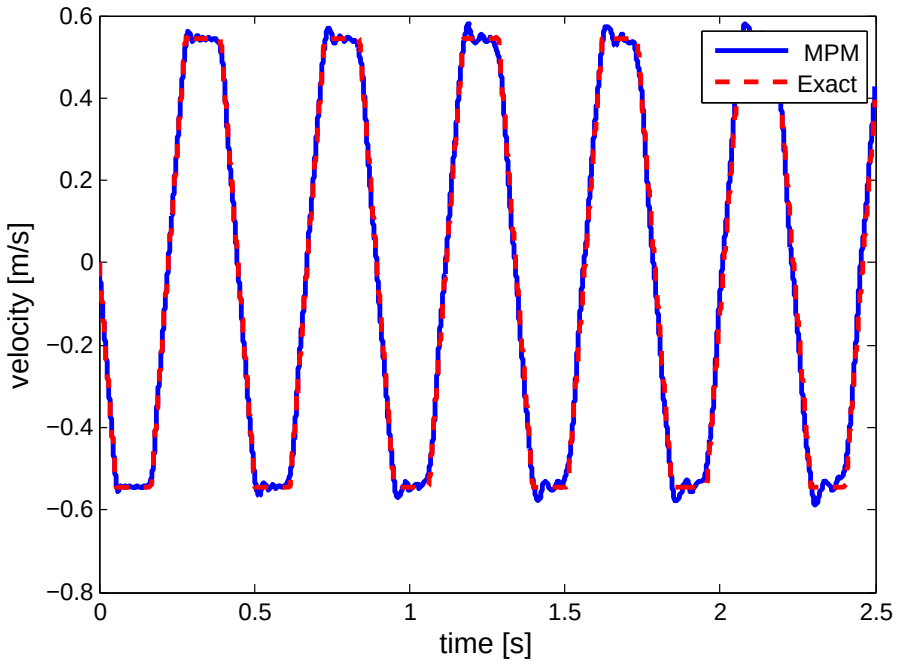

Figure 7.14: Velocity of the particle situated just underneath the column center with 2 particles per cell and 80 degrees of freedom. Grid crossing does occur.

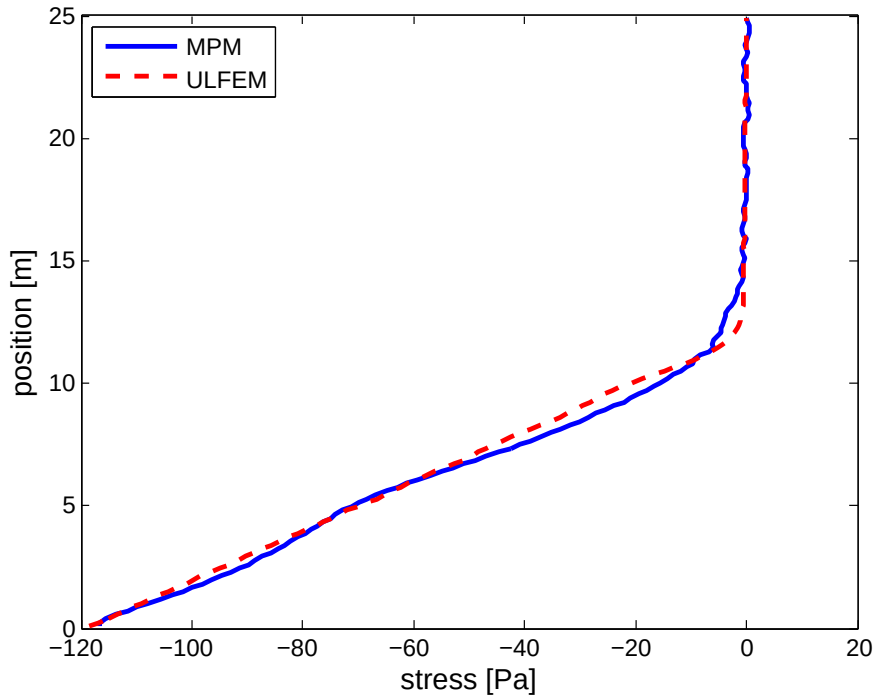

Figure 7.15: Stresses over the column obtained with spline based MPM at time $t = 0.5$ s.

7.2.4. COLUMN UNDER SELF-WEIGHT - LARGE DEFORMATIONS

When considering the second benchmark with deformations beyond 5 percent, the parameters values are listed in Table 4.4. A time step size is used of $\Delta t = 1 \cdot 10^{-4}$ s, which corresponds to a Courant number of $6.5 \cdot 10^{-2}$ in case of 66 degrees of freedom.

As in the previous subsection, the momentum conserving mapping used in the original MPM is adopted and only the internal force at the degrees of freedom is approximated with an alternative quadrature rule. The use of an alternative quadrature rule for the projection of particle velocities led to severe oscillations over time. A consistent mass matrix led to unrealistic high velocities at the degrees of freedom when entries of the mass matrix approached zero.

Figure 7.16 shows the resulting position of a material point initially situated directly underneath the column center. Compared with the results obtained in Chapter 6 (Figure 6.14) the quality of the MPM solution has improved. The obtained solution with spline based MPM is visually almost identical to the ULFEM solution based on 256 degrees of freedom.

The velocity of the material point initially situated direct underneath the column center is shown in Figure 7.17. Again, the obtained solution is visuallly almost identical to the ULFEM solution. The severe oscillations observed with B-spline MPM (Figure 6.15) are no longer present.

Figure 7.18 shows the stresses over the column obtained with spline based MPM at time $t = 0.5$ s. There is only a small difference between the solution obtained with MPM and ULFEM. Compared with the stresses over the column obtained with B-spline MPM (Figure 6.16) the quality of solution significantly has improved.

Results obtained for this benchmark show that the use of an alternative quadrature rule to determine the internal force at the degrees of freedom significantly improves the results in terms of displacement, velocity and stresses.

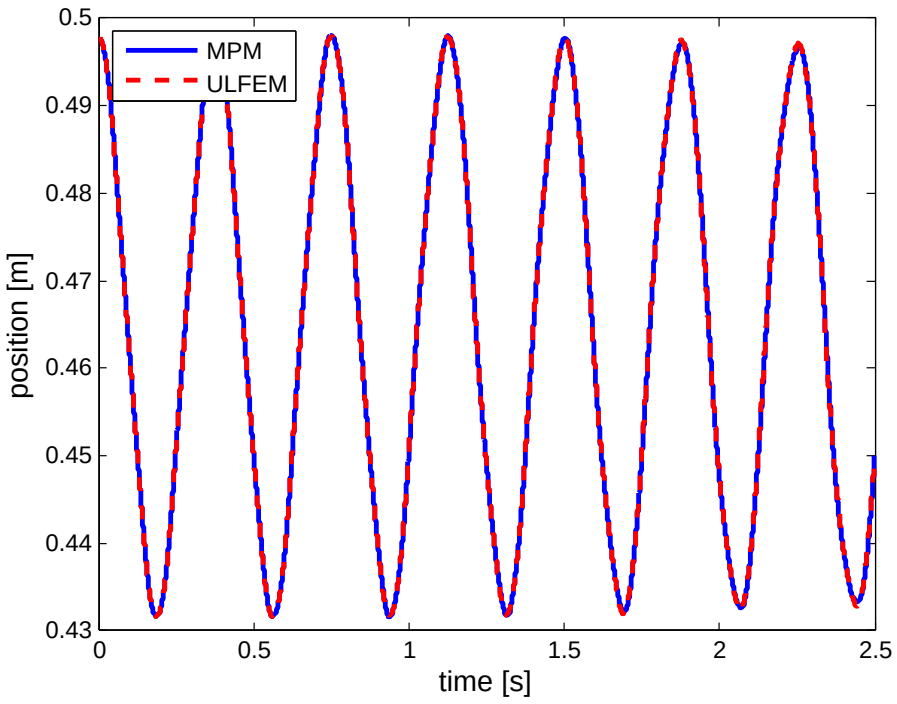

Figure 7.16: Position of the particle situated just underneath the column center with 4 particles per cell and 66 degrees of freedom. Grid crossing does occur.

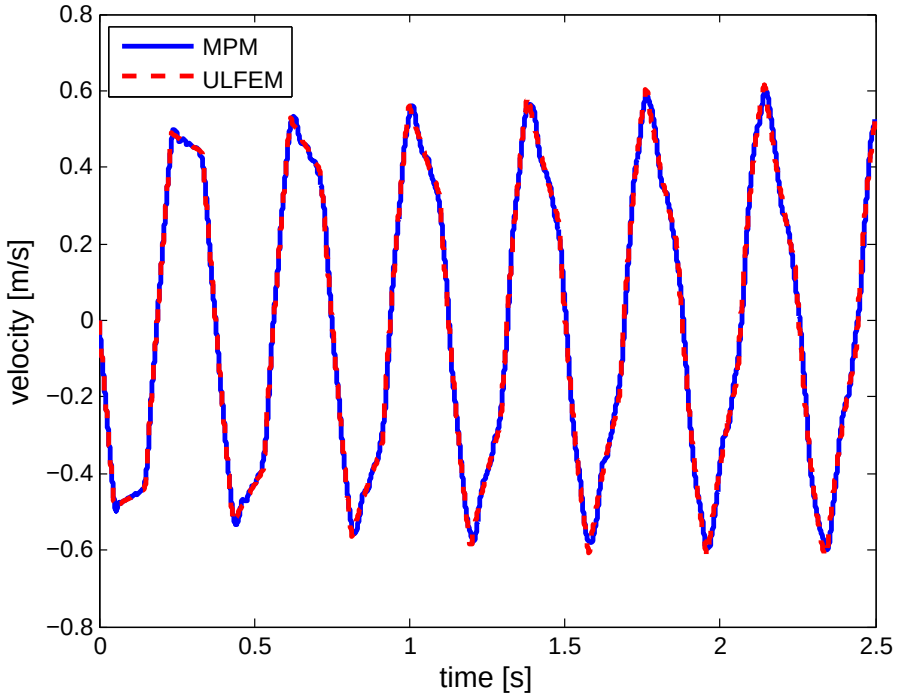

Figure 7.17: Velocity of the particle situated just underneath the column center with 4 particles per cell and 66 degrees of freedom. Grid crossing does occur.

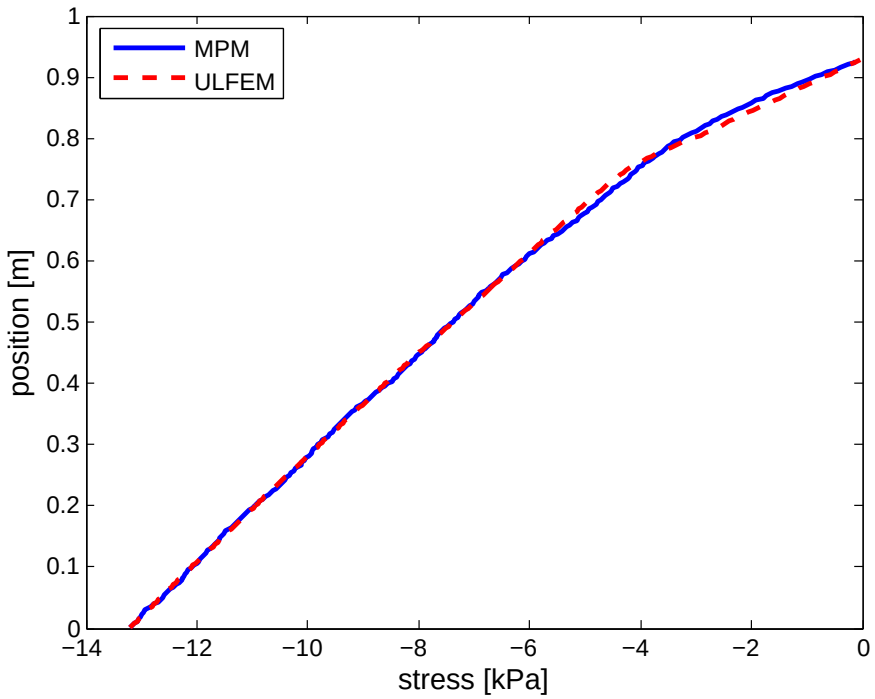

Figure 7.18: Stresses over the column obtained with B-spline MPM and spline based MPM at time $t = 0.5$ s.

7.3. CONCLUSIONS

In this chapter results for the two benchmarks considered in this thesis were presented and compared with those obtained with versions of MPM described in Chapter 5 and 6. The following conclusions can be drawn:

- Third order spatial convergence is observed when an alternative quadrature rule based on (cubic) splines is adopted for the internal forces and velocities. A necessary condition is the use of a consistent mass matrix to project particle velocity onto the degrees of freedom.
- The use of spline based MPM significantly improves the numerical solution for the second benchmark when considering large deformations. In case of small deformations a slight improvement is observed in the representation of the stresses.
- Using a consistent mass matrix or an alternative quadrature rule to project particle velocities onto the degrees of freedom leads to problems when entries of the mass matrix approach zero.

8

CONCLUSIONS

In this thesis the use of different types of basis functions within the MPM was investigated. Furthermore, the numerical quadrature rule used in the MPM was adapted by using spline interpolation. Based on the results for the benchmarks the following conclusions can be drawn:

- The use of Lagrange basis functions leads to numerical problems, which significantly reduce the quality of the numerical solution.
- Quadratic B-spline basis functions solve the problem of grid crossing leading to a more accurate MPM solution compared to the results obtained using Lagrange basis functions.
- An alternative quadrature rule to determine the internal force and velocity at the degrees of freedom improves spatial convergence for the vibrating bar problem when a consistent mass matrix is used in the projection of the velocity.
- Adopting an alternative quadrature rule for the internal forces and a momentum conserving mapping leads to the best results for the second benchmark, when entries of the mass matrix approach zero.

Note that the use of spline based MPM, with or without a momentum conserving mapping, increases the computation time when the same number of degrees of freedom and particles per cell are defined.

DISCUSSION

A decrease of the computational costs can only be achieved when the same accuracy can be obtained while using a coarser mesh and/or less material points. A variant of the second benchmark is considered to investigate whether this decrease can be achieved. The main idea behind these simulations is to compare of the classical MPM solution with that of spline based MPM under the condition that the computational costs are the same. The parameter values used for these simulations are listed in Table 8.1.

Quantity	Symbol	Value	Unit
Density	ρ	$1 \cdot 10^3$	[kg/m^3]
Young's modulus	E	$1 \cdot 10^5$	[Pa]
Gravitational acceleration	g	0	[m/s^2]
Column height	H	1	[m]
Top load	p_0	$-1 \cdot 10^4$	[Pa]

Table 8.1: Parameters used to model large deformations for the column.

Adopting these parameter values corresponds to a sudden load applied on top of a column without considering a gravitational load. This renders a wave front travelling from the top of the column to the bottom, where it is reflected. Since reproducing this shockwave is numerically challenging, it is a valuable benchmark to compare the classical MPM with the spline based MPM.

Figure 8.1 shows respecively the position and velocity of the material point directly underneath the column center obtained with the classical MPM and ULFEM. Results with the MPM are obtained with 321 degrees of freedom and initally 10 particles per cell. A reference solution is obtained with the ULFEM while defining 513 degrees of freedom.

Due to a sudden application of a load on top of the column a wave travels to the bottom. At $t = 0.05$ the wave reaches the center of the column causing the material point to move down. The wave is reflected at the bottom and reaches the material again at approximately time $t = 0.14$ s causing the material point to move up again.

The obtained velocity of the material point shows severe oscillations over almost the entire time interval leading to a solution for the position of the material point which does not correspond to the reference solution. The time needed for the computations was 2300 s.

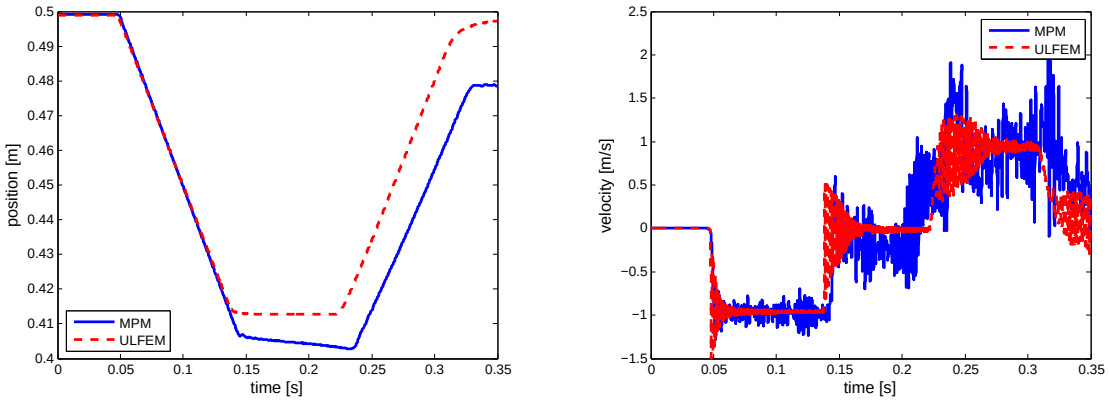

Figure 8.1: Position and velocity of top particle obtained with the classical MPM, 321 degrees of freedom and 10 initially particles per cell.

Figure 8.2 shows the solution for position and velocity of the material point directly underneath the center of the column obtained with spline based MPM. Results improve significantly since oscillations in the numerical solution for the velocity are reduced. The time needed for the computations was 1830 s.

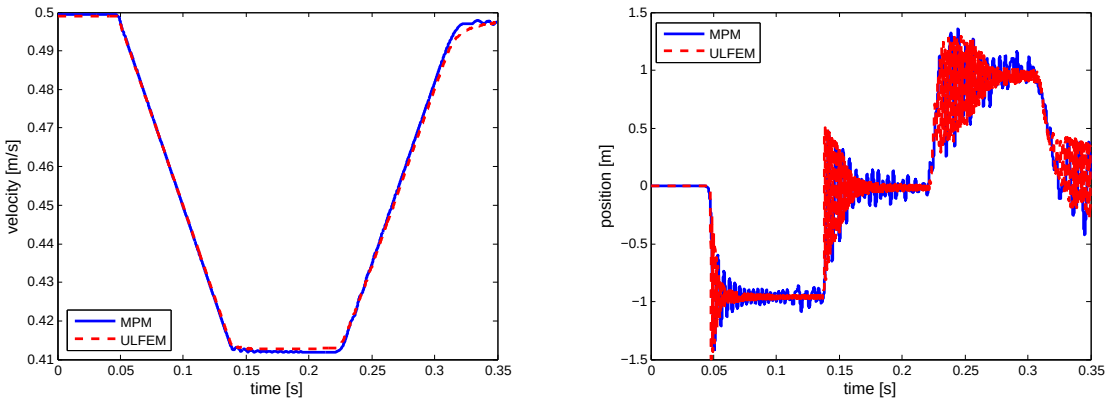

Figure 8.2: Position and velocity of top particle obtained with the spline based MPM, 258 degrees of freedom and 4 initially particles per cell.

Results indicate that the quality of the solution can be improved while decreasing the computational costs with the use of spline based MPM instead of the classical MPM.

EXTENSION TO 2D

When considering the use of B-spline basis functions in 2D, the concept of isogeometric analysis (IgA) plays an important role. Isogeometric analysis combines the techniques used in the FEM with the flexibility of spline functions. In IgA the isoparametric concept is adopted, implying that the solution is represented by the same basis functions as the geometry. However, in contrast with to the FEM, a geometry can be exactly reproduced within IgA leading to a more accurate result. More information about the concept of Iga can be found in [27] and [28].

For the MPM, an exact representation of the geometry is highly relevant, since this simplifies the application of traction boundary conditions and the adaption of the numerical quadrature rule used in MPM. Future research should therefore focus on the application of IgA within the MPM.

As shown in this thesis, continuity of the gradients of the basis functions eliminates the grid crossing error and improves the quality of the MPM solution. Obtaining C^1-continuity on an arbitrary domain in 2D can be achieved by division of the domain in multiple 'patches'. To ensure continuity of the gradient at the boundary of these patches, C^1-continuous multi-patch coupling techniques can be used [33].

To reconstruct a function of two variables based on known functions values, bicubic interpolation can be used. With bicubic interpolation, a function is reconstructed such that the first derivative with respect to each variable and the mixed derivative of this functions are continuous. However, depending on the computational costs, other function reconstruction techniques such as MLS, nearest neightbour or bilinear interpolation might be more preferable.

Future research should focus on these aspects when extending spline based MPM to 2D. However, applying these techniques in the MPM framework is a challenging task.

CONVERGENCE MPM

Although it is tempting to adopt third (or higher) order B-spline basis functions to improve spatial convergence, the overall convergence rate of the MPM is still limited due to different sources of error.

For example, the use of a lumped mass matrix in the density weighted mapping of the particle limits the convergence of the MPM. It was shown in this thesis that the order of convergence can be increased by adopting a consistent mass matrix. However, problems were encoutered when entries of the mass matrix approached zero. The use of a constrained projection might solve these problems, see [32]. Future research should focus on a mapping which does not limit the spatial convergence, is momentum conserving and can be used when the entries of the mass matrix approach zero.

To obtain a numerical method with an overall rate of convergence similar to the FEM, all steps of the MPM should be analyzed to identify those that limit the order of convergence and replace them before increasing the order of the basis functions further.

Simulations which involve more than a million degrees of freedom are expected in future analyses. Even if a high order of convergence can be achieved, high computational costs might limit the application of the MPM in practise. The use of high performance computing (HPC) techniques is therefore crucial to obtain results in a reasonable time.

A

APPENDIX

A.1. ASSEMBLY PROCEDURE

In the material point method the mass matrix and force vectors are determined by assembling the element matrices and element vectors. The assembly procedure for the mass matrix $\mathbf{M}$ and the force vector $\mathbf{F}$ are defined by the following formulas:

$$\begin{aligned} \mathbf{M} &= \sum_{el=1}^{n_e} (\mathbf{T}_e)^T \mathbf{M}_e \mathbf{T}_e, \\ \mathbf{F} &= \sum_{el=1}^{n_e} (\mathbf{T}_e)^T \mathbf{F}_e, \end{aligned}$$

where $\mathbf{T}_e$ denotes a Boolean matrix that scatters the entries of the local element matrix to their global positions in the global matrix.

The assembly procedure is illustrated with a 1D example where linear basis functions are used. Consider a domain consisting of three elements. This implies the existence of three mass matrices, each associated with an element. As an example, consider the following element mass matrices:

$$\mathbf{M}_1 = \begin{bmatrix} 5 & 4 \\ 2 & 7 \end{bmatrix}, \qquad \mathbf{M}_2 = \begin{bmatrix} 1 & 2 \\ 2 & 3 \end{bmatrix}, \qquad \mathbf{M}_3 = \begin{bmatrix} 7 & 3 \\ 5 & 2 \end{bmatrix}.$$

By defining the Boolean matrices

$$\mathbf{T}_1 = \begin{bmatrix} 1 & 0 & 0 & 0 \\ 0 & 1 & 0 & 0 \end{bmatrix}, \qquad \mathbf{T}_2 = \begin{bmatrix} 0 & 1 & 0 & 0 \\ 0 & 0 & 1 & 0 \end{bmatrix}, \qquad \mathbf{T}_3 = \begin{bmatrix} 0 & 0 & 1 & 0 \\ 0 & 0 & 0 & 1 \end{bmatrix},$$

the following global mass matrix is obtained:

$$\mathbf{M} = \begin{bmatrix} 5 & 4 & 0 & 0 \\ 2 & 8 & 2 & 0 \\ 0 & 2 & 10 & 3 \\ 0 & 0 & 5 & 2 \end{bmatrix}.$$

Since the dimension of the element matrices and vectors depend on the number of nodes per element also the Boolean matrices will differ when using higher-order Lagrange basis functions.

A.2. LUMPED MATRIX

The lumped mass matrix $\mathbf{M}^L$ is obtained from the consistent mass matrix $\mathbf{M}$ by putting all the weight of a row on the diagonal. Hence, $\mathbf{M}^L$ is defined by

$$\mathbf{M}^L_{(i,i)} = \sum_{j=1}^{n_{\text{dof}}} \mathbf{M}_{(i,j)},$$

where n_n denotes the number of nodes. Given the mass matrix $\mathbf{M}$ from section A.1, the lumped mass matrix becomes

$$\mathbf{M}^L = \begin{bmatrix} 9 & 0 & 0 & 0 \\ 0 & 12 & 0 & 0 \\ 0 & 0 & 15 & 0 \\ 0 & 0 & 0 & 7 \end{bmatrix}.$$

Every time step, acceleration at the degrees of freedom is obtained by solving equation (3.2), leading to the following expression:

$$\mathbf{a} = \mathbf{M}^{-1}\mathbf{F}.$$

In case a lumped mass matrix is used, the acceleration of degree of freedom i is given by:

$$\mathbf{a}_i = \frac{\mathbf{F}_i}{\mathbf{M}^L_{(i,i)}}.$$

The mass matrix is determined at the beginning of every time step. Therefore, the use of a lumped mass matrix reduces the computational time significantly.

The lumping procedure described above is however not used in our code of the one-dimensional MPM. Instead of lumping the consistent mass matrix, a procedure called *direct lumping* is adopted. This procedure makes use of the partition of unity property of the basis functions:

$$\sum_{j=1}^{n} \phi_j(x) = 1,$$

for all $x \in \Omega$. An arbitrary entry of the lumped mass matrix is then given by

$$\mathbf{M}^L_{(i,i)} = \sum_{j=1}^{n} \mathbf{M}_{(i,j)} = \sum_{j=1}^{n} \int_\Omega \phi_i(x)\rho(x)\phi_j(x)\mathrm{d}x = \int_\Omega \sum_{j=1}^{n} \phi_i(x)\rho(x)\phi_j(x)\mathrm{d}x = \int_\Omega \phi_i(x)\rho(x)\mathrm{d}x.$$

A.3. GAUSSIAN QUADRATURE

A Gaussian quadrature rule is a numerical integration rule where the definite integral of a function f is approximated in the following way:

$$\int_a^b f(x)\mathrm{d}x \approx \sum_{i=1}^{n} \omega_i f(x_i),$$

where ω_i denote the weights associated to the quadrature points x_i. For a n-point Gauss rule, the weights and quadrature points are chosen such that the numerical integration rule integrates polynomials of degree $2n-1$ or less exact.

To illustrate this, the weights and quadrature points will be derived for the interval $[-1,1]$ in case a 2-point Gauss rule is used. Let a polynomial f be given by

$$f(x) = a + bx + cx^2 + dx^3.$$

Since

$$\int_{-1}^{1} f(x)\mathrm{d}x = 2a + \frac{2}{3}c,$$

the weights w_1, w_2 and points x_1, x_2 must be chosen such that

$$\begin{aligned} 2a + \frac{2}{3}c &= \omega_1 f(x_1) + \omega_2 f(x_2) \\ &= \omega_1(a + bx_1 + cx_1^2 + dx_1^3) + \omega_2(a + bx_2 + cx_2^2 + dx_2^3) \\ &= (\omega_1 + \omega_2)a + (\omega_1 x_1 + \omega_2 x_2)b + (\omega_1 x_1^2 + \omega_2 x_2^2)c + (\omega_1 x_1^3 + \omega_2 x_2^3)d. \end{aligned}$$

Hence, the equality above leads to the following system of equations:

$$\begin{aligned} \omega_1 + \omega_2 &= 2 \\ \omega_1 x_1 + \omega_2 x_2 &= 0 \\ \omega_1 x_1^2 + \omega_2 x_2^2 &= \frac{2}{3} \\ \omega_1 x_1^3 + \omega_2 x_2^3 &= 0 \end{aligned}$$

Multiplying the second equation with x_1^2 and substracting it from the fourth equation results in

$$\omega_2 x_2^3 - \omega_2 x_1^2 x_2 = 0.$$

This equation has only one solution which might lead to a valid quadrature rule:

$$x_2 = -x_1.$$

Inserting this expression in equation one, two and three results in:

$$\begin{aligned} \omega_1 + \omega_2 &= 2 \\ \omega_1 x_1 - \omega_2 x_1 &= 0 \\ \omega_1 x_1^2 + \omega_2 x_1^2 &= \frac{2}{3}. \end{aligned}$$

Since $x_1 = 0$ will not lead to a valid quadrature rule, the first and second equation become:

$$\begin{aligned} \omega_1 + \omega_2 &= 2 \\ \omega_1 - \omega_2 &= 0. \end{aligned}$$

The weights ω_i are given by

$$\omega_1 = \omega_2 = 1.$$

After substituting this in the third equation, we obtain:

$$\begin{aligned} 2x_1^2 &= \frac{2}{3} \\ x_1 &= \sqrt{\frac{1}{3}}. \end{aligned}$$

Hence, a 2-point Gauss rule is given by:

$$\int_{-1}^{1} f(x)\mathrm{d}x \approx f\left(-\sqrt{\frac{1}{3}}\right) + f\left(\sqrt{\frac{1}{3}}\right). \tag{A.1}$$

To approximate the integral of a function on the interval $[a,b]$, equation (A.1) can be adapted, which results in [34]

$$\int_{a}^{b} f(x)\mathrm{d}x \approx \frac{b-a}{2} f\left(-\frac{b-a}{2}\sqrt{\frac{1}{3}} + \frac{a+b}{2}\right) + \frac{b-a}{2} f\left(\frac{b-a}{2}\sqrt{\frac{1}{3}} + \frac{a+b}{2}\right). \tag{A.2}$$

BIBLIOGRAPHY

[1] J. Donea, A. Huerta, J. Ponthot, and A. Rodriquez-Ferran, *Encyclopedia of Computational Mechanica* (Prentice Hall, 2004).

[2] M. Gong, *Improving the Material Point Method*, Ph.D. thesis, The University of New Mexico (2015).

[3] D. Sulsky, S. Zhou, and H. Schreyer, *Application of a particle-in-cell method to solid mechanics,* Computer Physics Communications **87**, p. 236 (1995).

[4] I. AL-Kafaji, *Formulation of a dynamic material point method (MPM) for geomechanical problems*, Ph.D. thesis, Institut für Geotechnik der Universität Stuttgart (2013).

[5] F. Harlow, *The particle-in-cell computing method for fluid dynamics,* Methods for Computational Physics **3**, p. 319 (1964).

[6] J. Brackbill and H. Ruppel, *Flip: a method for adaptively zoned, particle-in-cell calculations of fluid flows in two dimensions.* Journal of Computational Physics **65**, p. 314 (1994).

[7] D. Sulsky, J. Brackbill, and D. Burgess, *Mass matrix formulation of the flip particle-in-cell method,* .

[8] D. Sulsky, Z. Chen, and H. Schreyer, *A particle method for history-dependent materials,* Computer methods in applied mechanics and engineering **118**, p. 179 (1994).

[9] D. Sulsky and H. Schreyer, *Axisymmetric form of the material point method with applications to upsetting and taylor impact problems.* Computer Methods in Applied Mechanics an Engineering **139**, p. 409 (1996).

[10] D. Zhang, Q. Zou, B. VanderHeyden, and X. Ma, *Material point method applied to multiphase flows,* Journal of Computational Physics **227**, p. 3159 (2008).

[11] F. Hamad, D. Stolle, and P. Vermeer, *Modelling of membranes in the material point method with applications,* International Journal for Numerical and Analytical Methods in Geomechanics **39**, p. 833 (2015).

[12] A. Stomakhin, C. Schroeder, L. Chai, J. Teran, and A. Selle, *A material point method for snow simulation,* ACM Transactions on Graphics **32** (2013).

[13] D. Sulsky, H. Schreyer, K. Peterson, R. Kwok, and M. Coon, *Using the material-point method to model sea ice dynamics,* Journal of Geophysical Research **112** (2007).

[14] L. Malvern, *Introduction to the Mechanics of a Continious Medium* (Pearson, 1977).

[15] M. Möller, *Flow models and governing equations,* (Lecture slides) .

[16] W. Hu and Z. Chen, *A multi-mesh mpm for simulating the meshing process of spur gears,* Computers and structures **81**, p. 1991 (2003).

[17] M. M. J. Mieremet, *Numerical stability for velocity-based 2-phase formulation for geotechnical dynamic analysis*, Tech. Rep. (Delft Institute of Applied Mathematics, 2015).

[18] S. Bardenhagen and M. Kober, *The generalized material point method.* Computer Modeling in Engineering and Sciences **5**, p. 477 (2004).

[19] I. Fernandes, *Exploring quadratic shape functions in material point method*, Ph.D. thesis, University of Utah, year = 2004.

[20] L. Beuth, *Formulation of a Quasi-Static Material Point Method*, Ph.D. thesis, Universität Stuttgart (2012).

[21] J. Guilkey, J. Hoying, and J. Weiss, *Computational modeling of multicellular constructs with the material point method,* Journal of Biomechanics **39**, p. 2074 (2006).

[22] D. Zhang, X. Ma, and P. Giguere, *Material point method enhanced by modified gradient of shape function,* Journal of Computational Physics **230**, 6379 (2011).

[23] M. Steffen, R. Kirby, and M. Berzins, *Analysis and reduction of quadrature errors in the material point method (mpm).* International journal for numerical methods in engineering **76**, p. 922 (2008).

[24] S. Bardenhagen, *Energy conservation error in the material point method for solid mechanics,* Journal of Computational Physics **180**, p. 383 (2002).

[25] R. Haberman, *Applied Partial Differential Equations with Fourier Series and Boundary Value Problems* (Prentice Hall, 2004).

[26] S. Andersen and L. Andersen, *Analysis of spatial interpolation in the material-point method.* Computers and Structures **88**, p. 506 (2010).

[27] T. Hughes, J. Cottrell, and Y. Bazilevs, *Isogeometric analysis: Cad, finite elements, nurbs, exact geometry and mesh refinement,* Computer Methods in Applied Mechanics and Engineering **194**, p. 4135 (2005).

[28] J. Cottrell, T. Hughes, and Y. Bazilevs, *Isogeometric Analysis: Toward Integration of CAD and FEA* (Wiley, 2009).

[29] C. Vuik, P. v. Beek, F. Vermolen, and J. v. Kan, *Numerieke Methoden voor Differentiaalvergelijkingen* (VSSD, 2006).

[30] T. Belytschko, Y. Krongauz, D. , Organ, M. , Fleming, and P. Krysl, *Meshfree methods: An overview and recent developments.* Computer Methods in Applied Mechanics and Engineering **139**, p. 3 (1996).

[31] J. v. Kan, A. Segal, and F. Vermolen, *Numerical methods in scientific computing* (VSSD, 2008).

[32] D. Kuzmin, M. Möller, N. John, and M. Shashkov, *Failsafe flux limiting and constrained dat projection for equations of gas dynamics,* Journal of Computational Physics **229**, p. 8766 (2010).

[33] F. Buchegger, B. Juttler, and A. Mantzaflaris, *Adaptively refined multi-patch b-splines wth enhanced smoothness,* Applied Mathematics and Computation **272**, 159 (2016).

[34] R. Burden, D. Faires, and A. Burden, *Numerical Analysis* (Cengage Learning, 2005).